Detecting the 21 cm signal from the Epoch of Reionization using Drift Scans

A Thesis

Submitted for the Degree of

Doctor of Philosophy

to Jawaharlal Nehru University, New Delhi

by

Akash Kumar Patwa

Raman Research Institute
Bengaluru – 560 080, India

November 2020

Declaration

I, Akash Kumar Patwa, hereby declare that the work presented in this thesis titled "Detecting the 21 cm signal from the Epoch of Reionization using Drift Scans" is entirely original. This work has been carried out by me under the supervision of Prof. Shiv Sethi and Prof. K. S. Dwarakanath at Raman Research Institute, Bengaluru, India. I further declare that the subject matter presented in this thesis has not previously formed the basis for the award of any degree, diploma, membership, associateship or any other similar title of any university or institution. I have also run the thesis through the *Turnitin* software.

Prof. Shiv Sethi
(Thesis supervisor)
Prof. K. S. Dwarakanath
(Thesis co-supervisor)

Akash Kumar Patwa
Date:

Raman Research Institute
Bengaluru – 560 080
India

Certificate

This is to certify that the thesis titled "Detecting the 21 cm signal from the Epoch of Reionization using Drift Scans", submitted by Akash Kumar Patwa for the award of the degree of Doctor of Philosophy of Jawaharlal Nehru University, is his original work done under our supervision and guidance at the Raman Research Institute. This has not been published or submitted to any other university or institute for any other degree or diploma.

Prof. Shiv Sethi
(Thesis supervisor)

Director
Raman Research Institute
Bengaluru – 560 080
India

Prof. K. S. Dwarakanath
(Thesis co-supervisor)
Date:

To my family...

Acknowledgements

First of all I would like to thank my supervisors Prof. Shiv Sethi and Prof. K. S. Dwarakanath for guiding my research work. I learnt a lot from them about radio astronomy and cosmology. They always gave ample amount of time in discussions and taught me many nuances about the subjects. Without their guidance and support at various stages of my Ph.D., this thesis would not have been possible. I would also like to thank all teachers, especially Biman, in the course work who introduced me to various topics in astrophysics and cosmology. I express my deep gratitude to them.

RRI has excellent facilities and environment for a student. One of the best thing about RRI is its staff in administration, library, and canteen/mess. Among them, I would especially like to mention Vidya, Radha, Manjunath, and Harini, for helping me with administrative matters, for being prompt and flexible with time which made my non-academic work easier and less stressful.

During my Ph.D. course work, I enjoyed my classes and frequent travels with my batchmates – Madhuri, Aditi, Sanhita, Chaitanya, Abhishek, and Tushar. Probably it was the last class of my life as a student. I thank them for making it memorable.

My Ph.D. life was enriched by my wonderful friends with whom I shared many fun events and activities like Freshers' trips, Inhouse meetings, festival celebrations, parties etc. On the Astro floor, I enjoyed my time involving in many serious and not-so-serious discussions and going to Sankey Tank for snacks with my friends and colleagues. My life at RRI was eventful with friends from RMV hostel and other departments. It will be very difficult for me to categorize my friends as I share good memories with all of them on different occasions. So to avoid the trouble I list them in alphabetical order. I am really humbled to have friends like Abir, Aditi, Adwaith, Anand, Anjan, Ashwin, Bhagya, Chandeshwar, Gayathri, Gunjan, Irla, Karamveer, Kartick, Kshitija, Lijo, Manami, Mugundan, Mayuri, Nancy, Narendra, Naveen, Nazma, Nishant, Palak, Priyanka, Raj, Ranita, Raviranjan, Saichand, Sanhita, Shruti, Siddhartha, Sindhu, Sourabh, Sukhjovan, Varun, and Viral. I apologize to anyone who I missed to mention in this list by mistake. A special mention goes to two my wonderful friends Janakee and Saurabh. Both to them were extremely helpful and supporting to me on

multiple occasions in my Ph.D. life and I really enjoy our conversations on multitudes of topics. In future whenever I would think about my Ph.D., RRI, or Bangalore, I will always remember my friends with fond memories.

I dedicate my Ph.D. to my parents, brothers, and other members of my big family. They were patient and supported my decisions throughout my life. I am really lucky to have a family like them and can not imagine my life without them. Without their direct and indirect support, my Ph.D. would have not been possible.

Doing a Ph.D. is hard, challenging, and very demanding. My life in Ph.D. was full of ups and downs, and now I am glad that I finally made it. So, I again express my humble gratitude to everyone who helped me, encouraged me, and were involved in the last 5 years. I wish good luck to my friends and colleagues.

Synopsis

In the early universe there are two major transitions in the state of the baryonic matter: recombination and reionization. From the last scattering surface of the cosmic microwave background (CMB) photons we know that the recombination of primordial hydrogen took place at the redshift of $z \simeq 1100$. On the other hand, the reionization process is expected to have occurred in the redshift range $10 \gtrsim z \gtrsim 6$. However, the physical processes responsible for the reionization are poorly constrained. In the recent years there have been multiple efforts to directly probe the cosmic dawn (CD) and epoch of reionization (EoR) with redshifted 21 cm signal of the neutral hydrogen (HI) using radio telescopes designed to operate at low frequencies (50 MHz $< \nu <$ 200 MHz) (e.g. uGMRT, MWA, HERA, and LOFAR). Measurement of 21 cm signal (also known as HI signal) from EoR is expected to tightly constrain various cosmological and astrophysical phenomena including the formation and growth of large-scale structures, properties of underlying dark matter distribution and first luminous sources (stars and galaxies). According to current theoretical models, the strength of the 21 cm signal (10 mK at $z \simeq 8$) is at least three to four orders of magnitude weaker than the foregrounds (300 K) at 150 MHz. The major component of the foregrounds are extragalactic point-like radio sources and diffuse galactic emission. These foregrounds are spectrally smooth unlike the 21 cm signal. This discriminator is used to isolate the 21 cm signal from bright foregrounds.

In this thesis I have extended the analysis of Paul et al. [2014a] and have developed a theoretical and observational technique to extract the HI signal from low frequency radio data and have applied it on the real datasets from Murchison Widefield Array (MWA). I also provide a comprehensive framework to understand the underlying covariance of HI visibilities against the various observational parameters of the radio telescope (latitude of the telescope, size of the primary beam, baseline components, baseline length, and drift time).

In the drift scan mode of observation the beam of the telescope remains fixed in a chosen direction of the local coordinate system (e.g. at zenith) as sky drifts during observation. This strategy is important because it offers better system stability, stationary

primary beam, and smaller cosmic variance in comparison with the more conventional tracking observation (e.g. Paul et al. [2014a], Trott [2014]). The theoretical formalism, Drift Scan Formalism (DSF), developed in this thesis is based on the cross-correlation of the HI visibilities in time. It avoids noise bias and also gives optimal power spectrum estimate Patwa and Sethi [2019]. This formalism generalizes techniques based on the tracking mode observations, as they are a special case of DSF ($\Delta t = 0$; see Patwa and Sethi [2019]). For this endeavour, I studied the covariance properties of the HI visibility as a function of baseline length, its components (u and v), beam-width, latitude of the instrument, drift time, and input power spectrum. I also applied the formalism on the foregrounds and found that the time scale of the covariance properties of the point-like radio sources are much shorter than that of the 21 cm signal. This can be used to average out and thus mitigate the point-source contamination. This piece of work gains substantial importance since it enables us to understand the underlying phenomenon of covariance in the extraction of 21 cm power spectrum in a general framework. It should also settle some of the data-averaging issues in the community which led to the signal loss in the power spectrum estimate (e.g. Cheng et al. [2018]).

Based on DSF, a pipeline is developed to extract the HI power spectrum from drift scan data. This pipeline is applied on the drift scan data observed with MWA (3 hours in phase I and 55 hours in phase II) Patwa et al. [2021]. The covariance of a visibility pair is computed using DSF and is used as inverse weight to estimate the cylindrically and spherically averaged power spectra. I show that the RMS of mean power spectra in noise dominated Fourier modes fall as $1/t$ as more data are integrated. This behaviour is confirmed with the noise simulations with same configuration of the telescope. I also show that the foreground wedge in the cylindrically averaged power spectra weakens with the integration of data. This weakening of the foreground wedge is also predicted from DSF Patwa and Sethi [2019] as the decorrelation time scale of the point-like radio sources is predicted to be far shorter ($\lesssim 1$ min) than that of the HI signal in drift scan observations.

At the end, I conclude with the salient points of the thesis, summarize them in brief, and discuss some possible future direction to this work. The outline of the thesis is given below.

- Introduction to the Science of the Epoch of Reionization
- Radio Astronomy in the EoR Observations
- Drift Scan Formalism (DSF): A Theoretical and Analytical Study
- Power Spectra of the Drift Scan data from MWA using DSF
- Summary and Conclusions

Publications from the Thesis

- **Patwa, A. K.** & Sethi, S., *Detecting the 21 cm Signal from the Epoch of Reionization using Drift Scans: Correlation of Time-ordered Visibilities,* ApJ 887, 52 (Dec. 2019).
- **Patwa, A. K.**, Sethi, S., & Dwarakanath, K. S., *Extracting the 21cm EoR signal using MWA drift scan data,* MNRAS 504, 2062 (Jun. 2021).

Contents

List of Figures xix

List of Tables xxvii

1 Introduction to the Science of the Epoch of Reionization 1

1.1 Thermal History of The Universe - I . . . 2
1.2 Thermal History of The Universe - II . . . 4
1.3 Various probes of EoR . . . 5
1.3.1 Quasars: Gunn-Peterson Trough and Lyman-α Forest . . . 5
1.3.2 Lyman-α Emitters and Lyman Break Galaxies . . . 7
1.3.3 Cosmic Microwave Background . . . 8
1.3.4 The 21 cm Line of Neutral Hydrogen . . . 10
1.4 The 21 cm Cosmology . . . 10
1.4.1 Origin of the 21 cm Radiation . . . 11
1.4.2 Spin Temperature (T_s): Processes affecting the 21 cm Radiation 13
1.4.3 Radiative transfer of the 21 cm Radiation . . . 16
1.4.4 The Global 21 cm Signal . . . 18
1.4.5 The 21 cm Power Spectrum . . . 21
1.5 Plan of the Thesis . . . 24

2 Radio Astronomy in the EoR Observations 27

2.1 Basics of Radio Astronomy . . . 27
2.1.1 Radio Interferometry . . . 27
2.1.2 Aperture Synthesis . . . 30
2.2 The HI Visibility . . . 31
2.3 The HI Power Spectrum . . . 34
2.4 Sensitivity . . . 36
2.5 Challenges in the 21 cm Power Spectrum detection . . . 38
2.5.1 Foreground . . . 38
2.5.2 Other Challenges . . . 39
2.6 The Murchison Widefield Array (MWA) . . . 41

2.7 Summary . . . 42

3 Drift Scan Formalism (DSF): A Theoretical and Analytical Study 47
3.1 Introduction . . . 47
3.2 HI visibility correlation in Drift scans . . . 48
3.2.1 Visibility Correlation in Delay Space . . . 51
3.2.2 Approximations and input quantities . . . 62
3.3 Foregrounds in drift scans . . . 64
3.3.1 Point Sources . . . 64
3.3.2 Diffuse correlated foregrounds . . . 67
3.4 Analysing drift scan data . . . 71
3.4.1 Impact on foregrounds . . . 73
3.5 Summary . . . 74

4 Power Spectra of the Drift Scan data from MWA using DSF 77
4.1 Introduction . . . 77
4.2 Drift Scan Data . . . 78
4.2.1 Metadata . . . 79
4.2.2 Flagging, calibration, and averaging . . . 79
4.3 Data analysis methodology . . . 81
4.4 Normalization . . . 82
4.5 Data Analysis . . . 83
4.5.1 Gridding of *uv* field and power spectrum estimation . . . 83
4.5.2 Noise characteristics . . . 86
4.5.3 The HI power spectrum . . . 89
4.5.4 The 2-D Power Spectra and the Foreground Wedge . . . 91
4.5.5 Foregrounds in the Drift Scans . . . 92
4.6 Summary . . . 95

5 Summary and Conclusions 99
5.1 Current Upper Limits on The HI Power Spectrum . . . 102
5.2 Concluding Remarks and Future Works . . . 102
A Coordinate Transformation . . . 105
B Further simplification of visibility correlation function . . . 106

Bibliography 111

List of Figures

1.1 A comparison of results from successive CMB experiments - COBE, WMAP and Planck. The color represent the CMB temperature anisotropies ($\sim 10^{-4}$ K). Credit: Roen Kelly, *Astronomy*.* 3

1.2 It displays the time evolution of the Universe from CMB to present. Major cosmic events (e.g. dark ages, first stars etc.) are shown. Credit: Robertson et al. [2010] 3

1.3 This figure displays the spectra of 19 quasars studied using SDSS data. The spectra at redshifts $z > 6$ show absorption due to HI at shorter wavelengths. Credit: Fan et al. [2006]. 6

1.4 It shows the constraints on the neutral hydrogen fraction ($x_{\rm HI}$) against redshift (z) derived using three different observations. Credit: Dijkstra [2016] 8

1.5 It shows the E-mode (zero-curl) polarization power spectra of CMB. The reionization bump at small l (or large scales) arises due to the Thompson scattering of the CMB photons by free electrons in IGM introduced during reionization. Credit: Reichardt [2016] 9

1.6 It shows a cartoon picture of the global 21 cm signal $\langle \Delta T_{21} \rangle$ as a function of redshift and observing frequency ($\nu = \nu_{21}/(1+z)$). The profile of the signal depend on the various astrophysical and cosmological events. Credit: Pritchard and Loeb [2012] 18

1.7 It shows different periods of the cosmic history. These events imprint their respective signatures on the global 21 cm signal. Credit: Pritchard and Loeb [2012] 19

1.8 The 'absorption trough' detected by EDGES team. The depth and shape (flatness) of the signal are unexpected from the known theoretical understanding of the 21 cm cosmology. Credit: Bowman et al. [2018] 21

1.9 Based on simulations, the expected HI power spectrum from the early Universe is shown for many Fourier modes k against redshift (observing frequency) and ionization fraction $(1-x_{\rm HI})$. On large scales (small k-modes), $P_{21}(k)$ has three prominent peaks due to inhomogeneities in (peaks from left to right) ionization, heating of IGM, and Lyman-α radiation respectively. Credit: Santos et al. [2008] 23

2.1 It shows the setup of the two antenna interferometer measuring intensity I_ν in the sky. Variables are given in slightly different form: baseline $\boldsymbol{b} = \boldsymbol{r}_i - \boldsymbol{r}_j$; Credit: Taylor et al. [1999]. 29

2.2 In panel (a), the physical positions of the GMRT antennas are shown. The instantaneous baseline distribution constructed from the antennas is displayed in panel (b). Due to rotation of the earth, the baselines populate the uv plane in an hour long tracking observation (panel (c)). In general better uv coverage is desired for making better images. Credit: Kiehbadroudinezhad et al. [2014]. 32

2.3 Left: The typical foreground dominated modes are shown in gray in 3-D Fourier space. Right: The 3-D space depicted in the left is averaged cylindrically for each $k_\perp = \sqrt{\boldsymbol{k}_\perp \cdot \boldsymbol{k}_\perp}$. The foreground wedge and the EoR window are also marked. Credit: Thyagarajan et al. [2013]. . . . 40

2.4 A tile of the Murchison Widefield Array (MWA) consisting of 16 crossed-dipoles placed on a wired mesh. Credit: MWA Collaboration. 42

2.5 The locations of the 128 tiles in the phase I (top) and II (bottom) configurations of MWA are shown with respect to the center of the array. The phase I configuration has a compact core while other tiles are spread over a radius of ~ 1.5 km. The phase II has two compact hex arrangements for the redundant baselines and rest of the tiles extend upto about 400 m from the center. 43

3.1 The figure displays the amplitude of the visibility correlation function as a function of Δt, normalized to unity for $\Delta t = 0$. The quantity plotted in the figure is $\langle V_\tau(\mathbf{u}_0, w_0, t) V_\tau^*(\mathbf{u}_0, w_0, t')\rangle / \langle V_\tau(\mathbf{u}_0, w_0, t) V_\tau^*(\mathbf{u}_0, w_0, t)\rangle$ as a function of baseline length $|\mathbf{u}_0| = \sqrt{u_0^2 + v_0^2}$ and $\Delta t = t' - t$, for $u_0 = v_0$, $w_0 = 0$, and $\tau = 0$. The amplitude of the correlation function decorrelates mainly due to the rotation of the intensity pattern. However the impact of the traversal of the intensity pattern becomes important for smaller primary beams on small baselines. As seen in the figure, for all baselines for PAPER and large baselines for MWA, HERA, and SKA1-Low, the decorrelation time scales are proportional to $1/|\mathbf{u}_0|$ and $1/\sqrt{\Omega}$. This effect is discussed in subsection 3.2.1 (point (b)). On smaller baselines in MWA, HERA, and SKA1-Low panels, the traversal of the intensity pattern starts dominating the decorrelation. This effect is discussed in subsection 3.2.1 (point (a)). 54

3.2 Left Panel: The amplitude of the visibility correlation function is shown as a function of Δt for a fixed baseline for different primary beams. Right Panel: The isocontours of the decorrelation time are shown in the primary beam–baseline plane; the decorrelation time is defined as Δt such that the amplitude of correlation function falls to half its value as compared to $\Delta t = 0$. The Figure assumes Gaussian beams (Eq. 3.22) with FWHM $= 2\sqrt{\log_e(2)\Omega_{0g}}$. The region on the left bottom is excluded because the shortest baseline $\sqrt{u_0^2 + v_0^2} = d_0$, where d_0 is the primary element of the telescope in units of the central wavelength, λ_0. There could be minor differences between this figure and Figure 3.1 because we use a fixed telescope latitude $\phi = -26.7$ for all primary beams. The primary beams of the four interferometers studied in this work are marked on the figure. The White line demarcates the regions dominated by rotation (above the line) and traversal of intensity pattern (for further discussion see the text). 55

3.3 The figure shows the absolute value of the phase angle of the visibility correlation function (Eq. (3.26)) as a function of $\Delta t = t' - t$. This figure illustrates that the rapidly fluctuating component of the phase of the complex correlation function (Eq. (3.19)) can mostly be removed by multiplying it with $\exp(-i2\pi u_0 \cos\phi \Delta H)$. This allows us to determine the time scales for averaging the time-ordered visibilities in drift scans (section 3.2.1 and 3.4). 61

3.4 The visibility correlation function (Eq. (3.32)) is shown as a function of Δt (normalized to unity for $\Delta t = 0$) for two baselines $\sqrt{u_0^2 + v_0^2} = 20, 100$ for $u_0 = v_0$, for MWA primary beam and latitude. The visibility correlation function is seen to fall to half its value in a few minutes. . 67

3.5 In the left panel, we show two-dimensional power spectrum of DGE ($\Delta H = 0$) in the $k_\parallel$–$k_\perp$ plane in units $(\mathrm{mK})^2(\mathrm{h}^{-1}\mathrm{Mpc})^3$. The figure assumes $\nu_0 = 154\,\mathrm{MHz}$ and bandwidth $B = 10\,\mathrm{MHz}$. The relation applicable to the HI signal is used to transform from the telescope variables (u_0, v_0, τ) to the Fourier modes $(\mathbf{k}_\perp, k_\parallel)$, and to convert the power spectrum to the appropriate units (e.g. Paul et al. [2016]). The Figure highlights the separation of foregrounds from the EoR window; the bandwidth determines the extent of the flat region parallel to the $k_\parallel$ axis. In the right panel, the visibility correlation function (normalized to unity for $\Delta t = 0$) for DGE is shown for three baselines $\sqrt{u_0^2 + v_0^2} = 25, 50, 100$ (Eq. (3.42)). We also show the HI and point source visibility correlation functions for comparison. 70

4.1 This figure displays the Haslem map scaled to 154 MHz assuming the brightness temperature spectral index $\alpha = -2.52$ (Rogers and Bowman [2008]). The big circles correspond to the main lobe of the MWA primary beam at $\nu = 154\,\mathrm{MHz}$. The scan starts roughly at the location of the big circle on the right and lasts until the big circle on the left. The sky covered in the phase I and II are shown using big white and yellow circles, respectively. The smaller white circle shows the angular position of Fornax A. 80

4.2 MWA phase I and II *uv* distribution for a zenith drift scan (in units of $\lambda_0 = 1.945$ m). In phase II, 64 antennas are placed in two compact hex configuration to increase the number of short and redundant baselines. 84

4.3 The baseline distribution of phase I (top) and II (bottom) drift scan data used in this work. MWA phase II configuration has compact hex arrangement which creates a lot of short redundant baselines suited for EoR studies. 85

4.4 **Phase II**: The mean and RMS of power spectra of one *uv* pixel is displayed as a function of drift time. The Left column shows the outcome of Gaussian noise (GN) simulations for the baseline distribution of MWA Phase II. The second and third columns give results for XX and YY polarization, respectively. The first row shows the mean power spectrum while the second row shows the RMS of the power spectra. The horizontal axis in all the plots correspond to drift time. There are 129 curves in every panel, each corresponding to a different value of the delay space parameter τ (including $\tau = 0$). The dark and the light red coloured curves represent the wedge and horizontal bands (including two modes on either side of the band, respectively. The rest of the 'clean' modes in the EoR window are divided in two colours: intermediate values of τ in green and the cleanest modes corresponding to $\tau \geq 22$ (in units of B^{-1}) in light blue. Thick black line in the RMS plots correspond to the function $2a/t$, where t and a are in units of minutes and $(\mathrm{mK})^2(\mathrm{h}^{-1}\mathrm{Mpc})^3$, respectively. 89

4.5 **Phase I**: It displays the counterpart of Figure 4.4 for phase I data-sets. The RMS plots in the lower row panels clearly show the $1/t$ fall (lower black envelope) as per our expectations from simulations (left panels). For phase I, on comparison with the corresponding noise simulations, we find $a = 592 \times 10^{10}$ (XX) and $a = 472 \times 10^{10}$ (YY). 90

4.6 **Phase II:** These plots display the RMS of the power spectrum by re-defining the power spectrum as the average over randomly-chosen 100 grids which yields 54 data sets. The RMS is computed from these sets. The mean power spectrum is left unchanged by this procedure. The colour scheme is the same as in Figure 4.4. These plots enable us to distinguish between modes which are dominated by thermal noise from those that are not: the expected decrement in RMS for thermal noise is approximately a factor of 10, which is seen in clean modes; the wedge and the horizontal bands which are foreground dominated show a more complicated behaviour. 91

4.7 **Phase I:** This figure is the counterpart of Figure 4.6 for phase I data-sets. After the second level of averaging, it again follows the expected $1/t$ profile and we find $a = 50.2 \times 10^{10}$ (XX) and $a = 42.2 \times 10^{10}$ (YY). The ratio of old to new a values are 11.8 and 11.2. 92

4.8 The mean of the HI power spectra for a voxel are shown for the MWA data for both XX and YY polarizations. The mean power spectra are computed using 5254 pixels for a given delay parameter τ. The colour scheme is the same as in Figure 4.4. 92

4.9 The counterpart of Figure 4.8 for MWA phase I data-sets. 93
4.10 These plots are obtained from further averaging the power spectra shown in Figure 4.8 over randomly-chosen 100 grids which yields 54 sets the MWA Phase II data. The mean power spectrum is left unchanged by this procedure. The colour scheme is the same as in Figure 4.4. 94
4.11 The phase I counterpart of Figure 4.10. 95
4.12 2D Power spectra $\left[(\mathrm{mK})^2(\mathrm{h}^{-1}\mathrm{Mpc})^3\right]$ of 2- and 120-minute drift scans of MWA phase II. 96
4.13 The 10-night combined data are displayed for 200 minutes and 326 minutes of drift scan. 96
4.14 2D Power spectra $\left[(\mathrm{mK})^2(\mathrm{h}^{-1}\mathrm{Mpc})^3\right]$ of 2- and 120-minute drift scans of MWA phase I. With the data integration the noise reduces in the EoR window. However, the modes $k_\perp > 0.1h\mathrm{Mpc}^{-1}$ appears to be contaminated. 97

List of Tables

4.1 The table displays the normalization defined in Eq. (4.7) for the 10-night data for both XX and YY polarizations. 87

Chapter 1

Introduction to the Science of the Epoch of Reionization

Cosmology is the study of the Universe including its beginning, evolution, and its future. Since the ancient times, human beings have tried to understand the world around them using tools or methods they have at their disposal. The scientific understanding of cosmology is achieved using physics, astrophysics, and related observations. In this work we shall seek a scientific view of cosmology and will try to probe a key period in the history of the Universe called the 'epoch of reionization' (EoR).

In the last century, our knowledge about the Universe has expanded exponentially. The first building block of the modern physical cosmology was given by Albert Einstein in 1917 when he applied the general theory of relativity on the scale of the Universe which gave a model of a static Universe (with cosmological constant Λ) (original paper is reproduced in Einstein [1952]). Since the 'nebulae' like celestial objects were already proven to be distant star-systems (galaxies) away from Milky Way (Shapley and Curtis [1921]), in 1922 Alexander Friedmann predicted an expanding Universe based on general theory of relativity (Friedmann [1922]). Few years later in 1927, the prediction by Friedmann was independently confirmed by Georges Lemaître (Lemaître [1927]). In 1929, the static model of the Universe was rejected in the favour of an expanding one with the observations of receding galaxies by Edwin Powell Hubble (Hubble [1929]).

The expanding Universe model implied that the Universe would have been much denser and hotter in the past with a beginning or a singularity. This led to the formulation of the 'Big Bang theory' according to which the Universe starts with an 'explosion' (big bang). The background model explains the expansion of the universe while its fluctuations can explain the formation of galaxies due to the gravitational instability. The next milestone in the support of the Big Bang theory and of broader

understanding of the physical cosmology came with the accidental detection of the 'cosmic microwave background radiation' (CMB or CMBR) in 1965. Penzias and Wilson [1965] found an excess of ~ 3.5 K in the measurement of antenna noise temperature of their radiometer. It was established that the unaccounted temperature was of cosmological origin. Hence, the existence of CMB was confirmed and the Big Band model of the Universe was widely accepted in the cosmology community.

Since 1990, there have been rapid developments in the area of observational cosmology, led by landmark cosmology experiments that include COsmic Background Explorer (COBE; Mather et al. [1990], Fixsen et al. [1994]), Wilkinson Microwave Anisotropy Probe (WMAP; Hinshaw et al. [2013]), Planck (Planck Collaboration et al. [2020]), RELIKT-1 or RELICT-1 (Strukov et al. [1992]), Balloon Observations of Millimetric Extragalactic Radiation and Geophysics (BOOMERanG; de Bernardis et al. [2000]), etc (see Figure 1.1). These experiments have determined, with high precision, both the background dynamics and its parameters (e.g. cosmological parameters $\Omega_m, \Omega_b, \Omega_\Lambda, H_0$ etc) and the inhomogeneous universe (e.g. CMB angular power spectrum and galaxy clustering) (Staggs et al. [2018]). With the observation of high-redshift type-1a supernova, it has also been determined that the Universe is not only expanding but also accelerating (Riess et al. [1998], Perlmutter et al. [1999]). The culmination of these findings was that the old Big Bang model of the Universe was modified to include 'dark energy' (sometimes interpreted as Λ introduced by Einstein) and cold 'dark matter' (CDM). The existence of CDM was also predicted from the galaxy rotation curves and the Big Bang nucleosynthesis. This modified model, known as Lambda-CDM model, is now considered the standard model of the Universe in physical cosmology. Some salient aspects of the model are discussed in the next section.

1.1 Thermal History of The Universe - I

A brief timeline of the Universe is given in Figure 1.2. The Universe came in to existence with an 'explosion' approximately 13.8 billion years ago. It underwent an exponential expansion phase termed the 'inflation'. During the inflation, the quantum fluctuations created fluctuations which provided the seeds for the formation of the large scale structure via gravitational instabilities.After the end of the inflationary period, the universe reheats and makes a transition to radiation domination. The radiation-dominated Universe consisted of photons, dark matter, and baryonic matter strongly coupled to photons. The high temperatures and strong photon-baryon coupling kept the baryons ionized and the Universe completely opaque. It also caused baryonic temperature T_K and radiation temperature T_R to be equal, with both decreas-

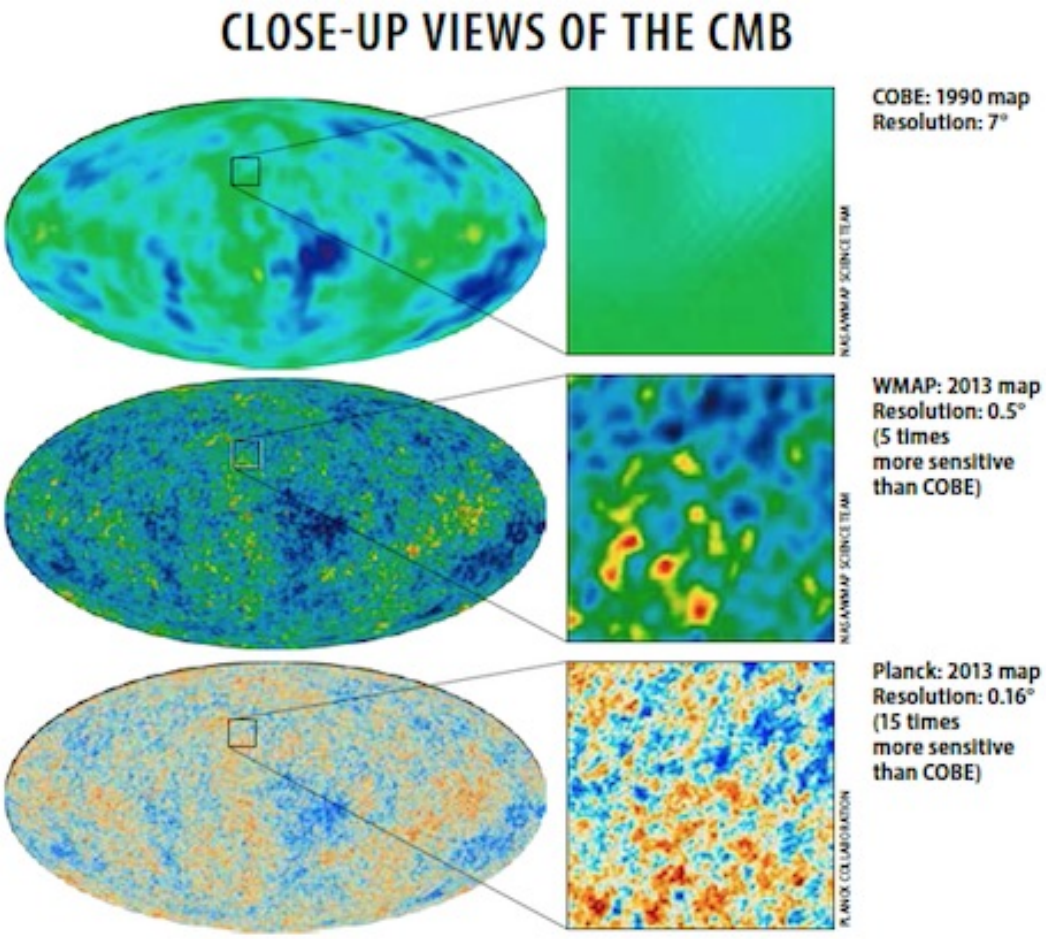

Figure 1.1: A comparison of results from successive CMB experiments - COBE, WMAP and Planck. The color represent the CMB temperature anisotropies ($\sim 10^{-4}$ K). Credit: Roen Kelly, *Astronomy*.*

*https://astronomy.com/magazine/2018/07/decoding-the-cosmic-microwave-background

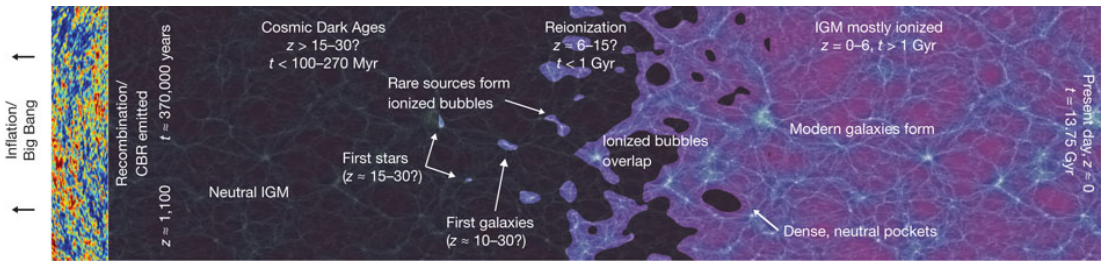

Figure 1.2: It displays the time evolution of the Universe from CMB to present. Major cosmic events (e.g. dark ages, first stars etc.) are shown. Credit: Robertson et al. [2010]

ing as $1/(1+z)$[1]

1.2 Thermal History of The Universe - II

Next major event in the timeline of the Universe is the matter-radiation equality ($\sim$ 47,000 years after the Big Bang or $z \sim 3300$). At this epoch, perturbations created during the inflationary era begin to grow in the cold dark matter component, which interact only via gravitational force. The dark matter perturbations create potential wells which capture baryons in the post-recombination era.

The next important event (epoch of recombination) occurs nearly 370,000 years after the Big Bang ($z \sim 1100$). At this era, the universe makes a transition from ionized to neutral, as the temperature and density of the Universe are such that the rate of hydrogen ionization falls below the rate of electron-proton recombination. At the end of the epoch of recombination, the Universe becomes (almost) completely neutral and enters 'Dark Ages' (because there were no luminous sources). The decoupling of the matter and radiation is almost complete and photons can now travel freely marking the 'last scattering surface' or 'cosmic microwave background' (CMB or CMBR).

In the redshift range $1100 \lesssim z \lesssim 150$, the radiation and matter temperature are the same, as the Compton scattering between residual free electrons and CMB photons help maintain the coupling between CMB photons and kinetic temperature of neutral hydrogen. Around $z \sim 30$, the first luminous sources (stars and galaxies) appear in the universe; this phase transition is called 'Cosmic Dawn' (CD).

Although these sources emit in a wide spectrum like a blackbody, the UV photons, X-rays, and Lyman-α photons are the most relevant: a) the UV photons reionize the neutral hydrogen in the IGM and create HII bubbles (Strömgren sphere) around the luminous source; b) the X-ray photons heat the neutral hydrogen in the IGM; c) the Lyman-α photons couple the hyperfine line of neutral hydrogen with the kinetic temperature in the universe (Wouthuysen-Field effect).

With time the ionized bubbles grow and eventually merge with other ionized bubbles resulting in a ionised Universe. Recent research suggest that the Universe was mostly reionized in $10 \lesssim z \lesssim 6$ except for the residual HI in dense, self-shielded clouds (see for example Barkana and Loeb [2001], Sethi [2005], Fan et al. [2006], Furlanetto et al. [2006b], Morales and Wyithe [2010]). The cosmic period during which the Universe underwent transition from neutral to ionized is known as 'Epoch of Reionization' (EoR).

Our understanding of the Universe has improved significantly in the last few decades.

[1] Here z denotes the redshift.

CMB experiments revealed the details of the epoch of recombination while large scale galaxy surveys (e.g. SDSS[1] and 2dFGRS[2]) explored the Universe at lower redshifts. The time period between these two eras, especially the EoR, is yet to be probed with the same level of precision. The EoR is expected to give us insights into the duration and the topology of the reionization process, details of its evolution, nature of first luminous objects, hierarchy of structure formation, dynamical evolution of large scale structures, etc (Furlanetto et al. [2006b], Pritchard and Loeb [2012], Zaroubi [2013]). In the next section, we review the available evidence from the EoR.

1.3 Various probes of EoR

Above we discussed the evolution of physical cosmology in the last century. We also reviewed the standard model of modern cosmology and mentioned few missing links in the thermal history of the Universe. The epoch of reionization is one such missing link holding a treasure trove of early cosmology. In this section, we provide various probes to EoR and discuss corresponding findings.

1.3.1 Quasars: Gunn-Peterson Trough and Lyman-α Forest

The term "quasar" is the short form of "quasi-stellar radio source" (Chiu [1964]). They were first discovered in early 1960s as star-like objects (quasi-stellar objects/QSOs) of unidentified origins emitting at radio frequencies. One of the brightest sources in the Universe, a quasar is an AGN which consists of a supermassive blackhole (mass of the order $10^6 - 10^9\ M_\odot$) surrounded by an accretion disk.

Interestingly, one feature of quasars is that they have a fairly smooth spectra irrespective of their location in the Universe. Any change in the characteristic spectrum of a quasar can be used to study the IGM between the quasar and the observer. This probe is very sensitive to the amount of neutral hydrogen (HI) in the IGM owing to the large cross-section of Lyman-series lines (e.g. the Lyman-α transition $n = 2 \rightarrow 1$) with rest frame wavelength (1216Å). Thus the photons emitted from QSOs close to frequency of Lyman-α transition get absorbed by HI atoms and are re-emitted in a random direction. Due to the expansion of the Universe and abundance of HI in IGM, this process creates several absorption lines, called Lyman-α forest, in the observed spectra of QSOs at wavelengths larger than the Lyman-α transition. Predicted by Gunn and Peterson [1965], the strong expected absorption of all photons below the Lyman-α wavelength by HI is called Gunn-Peterson (GP) trough. Becker et al. [2001] detected the GP trough for the first time in the spectrum of a quasar at $z = 6.28$ suggesting that

[1] Sloan Digital Sky Survey Gunn et al. [2006]
[2] 2dF Galaxy Redshift Survey Colless et al. [2001]

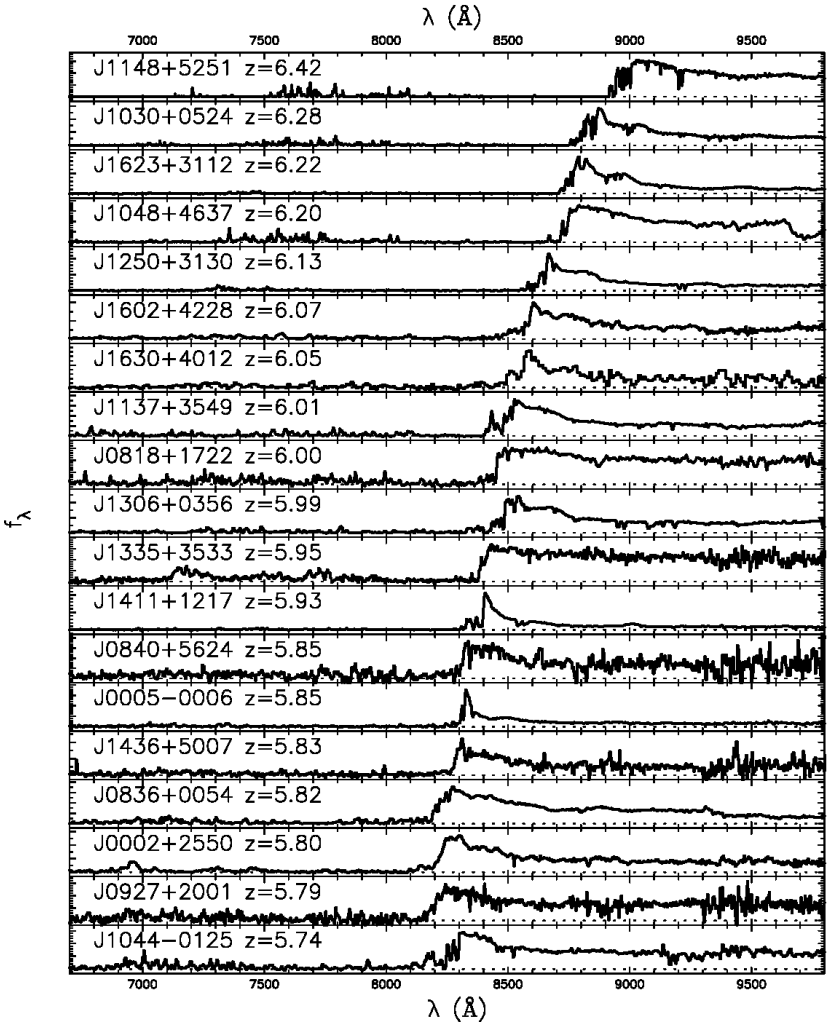

Figure 1.3: This figure displays the spectra of 19 quasars studied using SDSS data. The spectra at redshifts $z > 6$ show absorption due to HI at shorter wavelengths. Credit: Fan et al. [2006].

the Universe was at least partly neutral $z > 6$. Later Fan et al. [2006] studied a sample of 19 quasars in the redshift range $5.74 < z < 6.42$ using high resolution SDSS data and confirmed that reionization ended at $z \sim 6$ (see Figure 1.3). The optical depth of GP, a function of redshift (z), is given by (Eq. (2) of Fan et al. [2006])

$$\tau_{\rm GP}(z) = 1.8 \times 10^5 h^{-1} \Omega_m^{-1/2} \left(\frac{\Omega_b h^2}{0.02}\right) \left(\frac{1+z}{7}\right)^{3/2} \left(\frac{n_{\rm HI}}{\langle n_{\rm HI}\rangle}\right), \qquad (1.1)$$

where angular brackets represent the spatial average, $n_{\rm HI}$ is the number density of HI , and Ω_b, Ω_m, and h have their usual meanings. As suggested from this equation, for a small amount of HI present in the line-of-sight of a QSO the Gunn-Peterson optical depth is large and thus enough to absorb the Lyman-α photons in the rest frame of HI cloud. Thus the spectra from quasars present at high redshifts ($z \sim 6$) can be used as a probe (but not a very good one) to study the reionization history of the Universe.

1.3.2 Lyman-α Emitters and Lyman Break Galaxies

In the subsection 1.3.1 we studied how the characteristic spectra of high redshift quasars provide a tool to understand the reionization history of the Universe. It is possible owing to the large optical depth of the absorption of Lyman-α photons in the IGM. The probe described in this section is based on related processes based on two types of galaxies: Lyman-α emitters and Lyman Break galaxies.

The Lyman-α emitters (LAEs) are galaxies which emit predominantly in narrow band near Lyman-α transition. They are relatively young galaxies having low mass ($10^8 - 10^{10}\ M_\odot$), low metallicity, and high star-formation rate (Malhotra and Rhoads [2002, 2004]). In LAEs, recombination lines from HII regions in the ISM produce these Lyman-α photons. This provides us a way to detect the young galaxies in the Universe (Partridge and Peebles [1967]). The ionized ISM of LAEs allows Lyman-α photons to escape the galaxy easily. However, the flux from LAEs is diminished in the presence of neutral IGM because the escaping Lyman-α photons would be scattered by HI as discussed in the subsection 1.3.1. This probe is sensitive to HI fraction of $\sim 30\% - 50\%$. The observation of LAEs constrains the reionization to be mostly complete at the redshift $z \sim 6.5$ (Malhotra and Rhoads [2004]). In other words, the LAEs probe the mid to late and overlapping phase of the reionization which is complementary to other probes discussed in this section.

The second type of galaxies which probe the reionization are Lyman Break Galaxies (LBGs). The LBGs are star-forming galaxies which are bright at wavelengths greater than Lyman limit (rest frame wavelength 912 Å) but are very dim at wavelengths shorter than Lyman limit. This "break" or "dropout" is due to the presence of HI in the IGM. The observation of spectroscopic spectra from high redshift LBGs show that the number of such galaxies decrease in the redshift range $z \sim 6-7$ and that the fall is smaller for brighter objects in the sample. It suggests two interesting points about the reionization history of the Universe: first, the HI fraction increases in the IGM in the redshift range $z \sim 6-7$ and, second, the hierarchy of the reionization was from high to low density regions (inside-out model of reionization) (Ono et al. [2012]). This drop in the number of LBGs can also be interpreted with the appropriate change in the fraction of ionizing photons which escape the galaxy (Dijkstra et al. [2014]).

The constraints on the reionization history of the Universe, e.g. the redshift at which the HI fraction ~ 0.5, obtained from methods based on Lyman-α galaxies and quasars (subsection 1.3.1) seem to be consistent with each other. These results along with CMB-based probe (discussed in next subsection) are shown in Figure 1.4.

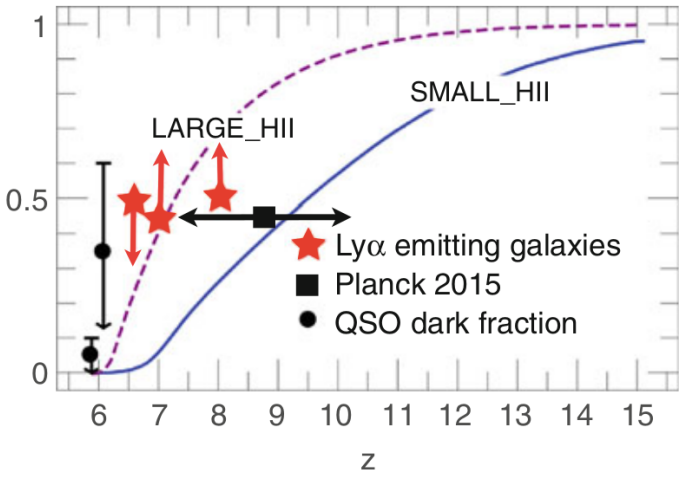

Figure 1.4: It shows the constraints on the neutral hydrogen fraction ($x_{\rm HI}$) against redshift (z) derived using three different observations. Credit: Dijkstra [2016]

1.3.3 Cosmic Microwave Background

One major evidence of the epoch of reionization of the Universe comes from the CMB temperature and polarization anisotropies (e.g. Rees [1968], Hu and White [1997], Bennett et al. [2013], Planck Collaboration et al. [2020]). Most of the CMB photons last scattered at $z \sim 1100$. However, a small fraction (less than 10%) of these photons re-scattered during the epoch of reionization. Therefore, CMB contains crucial signatures of this era.

The free electrons created during the epoch of reionization interact with incoming CMB photons via Thompson scattering. There are two main effects owing to this scattering. First, the anisotropies on scales smaller than the horizon at the epoch of the scattering are diminished. Second the scattering introduces secondary anisotropies on top of (primary) anisotropies of background (CMB) radiation field (Rees [1968], Hu and White [1997]). While these secondary anisotropies have negligible impact of temperature anisotropies, they can substantially alter the polarization angular power spectrum, creating a bump (called 'reionization bump') on large scales (multipoles l corresponding to angular scales larger than roughly the horizon at the epoch of reionization; see Figure 1.5). Given the number density of the free electrons and history of the reionization, it is possible to calculate the optical depth ($\tau_{\rm reion}$) of Thompson scattering:

$$\tau_{\rm reion} = \int n_e(z)\sigma_T ds = \int_0^{z_{\rm LSS}} n_{\rm H,0}(1+z)^3 f_i(z)\sigma_T \frac{cdz}{(1+z)H(z)}, \qquad (1.2)$$

where $ds = \frac{cdz}{(1+z)H(z)}$ is the physical infinitesimal path length traveled by photons, σ_T

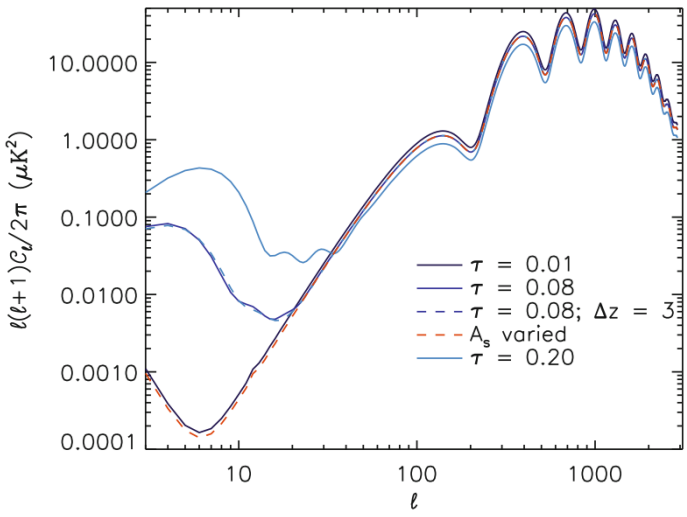

Figure 1.5: It shows the E-mode (zero-curl) polarization power spectra of CMB. The reionization bump at small l (or large scales) arises due to the Thompson scattering of the CMB photons by free electrons in IGM introduced during reionization. Credit: Reichardt [2016]

is the Thomson scattering cross-section, $n_e(z) = n_{\mathrm{H},0}(1+z)^3 f_i(z)$ is the free electron number density, $f_i(z)$ is a function which characterizes the progress of reionization, $n_{\mathrm{H},0}$ is the hydrogen number density at $z = 0$ and z_{LSS} is the approximate redshift of the last scattering surface. The contribution of free electrons from the ionization of Helium (He) atoms is ignored for the simplicity. To solve the integral analytically, reionization history ($f_i(z)$) has to be assumed. In the simplest case an instantaneous reionization is considered (a step function) i.e. $f_i(z \leq z_{\mathrm{re}}) = 1$ and $f_i(z > z_{\mathrm{re}}) = 0$. With this value of $f_i(z)$ and $H(z) = H_0 \left(\Omega_\Lambda + (1+z)^3 \Omega_m\right)^{1/2}$, the optical depth in Eq. (1.2) is found to be

$$\tau_{\mathrm{reion}} = \frac{2c\sigma_T n_{\mathrm{H},0}}{3\Omega_m H_0} \left[\left(\Omega_\Lambda + \Omega_m \left(1+z_{\mathrm{re}}\right)^3\right)^{1/2} - \left(\Omega_\Lambda + \Omega_m\right)^{1/2} \right]. \tag{1.3}$$

Using the above equation it is possible to compute the value of z_{re} from CMB data. The recent Planck Collaboration et al. [2020] results yield $z_{\mathrm{re}} \simeq 8.6$. In other words, if the Universe was to be reionized instantaneously given current observations it would be at the redshift $z_{\mathrm{re}} \simeq 8.6$. It can be noticed that the derived redshift of reionization with a simple toy model of the reionization history (instantaneous; step function) is close to what is found from other experiments ($6 \leq z_{\mathrm{re}} \leq 7$ e.g. Fan et al. [2006], Malhotra and Rhoads [2004]). It can be further refined by taking in to account the following: free electron contribution from the ionization of Helium, a detailed and realistic model of the history of reionization, kinetic Sunyaev-Zeldovich effect (discussed below), lensing effects, BAO etc. With these additional factors Planck Collaboration et al. [2020] derive the redshift of (mid-) reionization to be $z_{\mathrm{re}} = 7.82 \pm 0.71$. It matches better with

other probes as the reionization is expected to be a extended process.

Another probe of reionization utilizing CMB radiation is the kinetic Sunyaev-Zeldovich (kSZ) effect. In the thermal SZ effect the CMB spectrum is distorted via inverse Compton scattering by hot electrons in IGM. Predicted by Sunyaev and Zeldovich [1972], the thermal SZ effect boosts the energy (frequency) of low-energy CMB photons. This effect is second order in v/c and depends on the temperature difference between electrons and CMB. In the kinetic SZ (kSZ) effect, the CMB photons are scattered off electrons with bulk velocity with respect to the comoving frame (Sunyaev and Zeldovich [1980], Ostriker and Vishniac [1986]). This effect is linear in v/c where v corresponds to the bulk velocity of electrons and does not result in spectral distortion of CMB but gives either enhancement or decrement of CMB temperature. The kSZ effect for the patchy distribution of ionizing regions creates small (arcminute) scale temperature anisotropies in the CMB. The measurement of these small scale secondary anisotropies provides another key to understand the reionization process (Carlstrom et al. [2002], McQuinn et al. [2005]). In 2015 the South Pole Telescope (SPT) lead SPT-SZ survey covering 2500 deg^2 of sky studied these secondary anisotropies (tSZ and kSZ both) on small angular scales $1' \lesssim \theta \lesssim 5'$ and put the upper limit on the duration of reionization, $\Delta z < 5.4$, with 95% confidence level (George et al. [2015]).

1.3.4 The 21 cm Line of Neutral Hydrogen

The 21 cm line of HI is one of the most promising probe of the CD/EoR. It is a direct probe using which one can study the HI distribution of the Universe both spatially and temporally, time period and details of the reionization process, hierarchy of the large scale structure formation, nature of the first sources, etc. The 21 cm line (in vacuum, rest frame frequency $\approx$ 1420.4 MHz and wavelength $\approx$ 21.1 cm) corresponds to the transition between the triplet and the singlet hyperfine levels of the ground state of the neutral hydrogen. Due to the expansion of the Universe the 21 cm line emitted during the Cosmic Dawn and epoch of Reionization redshifts to meter wavelengths which can be observed in frequency range 50-200 MHz using modern radio telescopes. Since this thesis is dedicated to study a particular observation method of 21 cm from EoR using radio interferometers, the next subsection seeks to elaborate the physics of 21 cm line, with particular focus on cosmology.

1.4 The 21 cm Cosmology

The 21 cm cosmology is a subset of modern cosmology in which the early Universe is studied using the 21 cm line of the neutral hydrogen. In this section we have taken an inside-out approach: we go from atomic level, to local, and eventually to cosmological

scale. We discuss, in detail, the physical origin of the 21 cm line, its sensitivity to other physical parameters, and how it allows us to study the cosmic dawn and the epoch of reionization.

1.4.1 Origin of the 21 cm Radiation

In this subsection the origin of 21 cm line is discussed, based on the quantum mechanics of the hydrogen atom in the ground state.

Both electrons and protons are fermions with "spin" angular momentum $\hbar/2$ each. The magnetic moments of these particles created by their intrinsic spin angular momenta are:

$$\boldsymbol{\mu}_p = \frac{g_p e}{2m_p}\boldsymbol{S}_p, \qquad \boldsymbol{\mu}_e = -\frac{g_e e}{2m_e}\boldsymbol{S}_e\ , \tag{1.4}$$

where the variables in bold letters are vector quantities, g is the g-factor accounting for quantum effects, m_p and m_e are masses of proton and electron, respectively, e is the electronic charge, $\boldsymbol{S}$ represent the spin operator of the particles. In the electron's rest frame, the electron experiences a magnetic field, $\boldsymbol{B}_p \equiv \boldsymbol{B}_p(\boldsymbol{\mu}_p)$, owing to proton's magnetic moment. The spin magnetic dipole moment of the electron interacts with this magnetic field. Since the magnetic field $\boldsymbol{B}_p$ is a function of $\boldsymbol{\mu}_p$ which in turn is a function of spin of the proton, this spin-spin interaction perturbs the Hamiltonian of the hydrogen atom by a small amount $(-\boldsymbol{\mu}_e \cdot \boldsymbol{B}_p)$. According to perturbation theory of the quantum mechanics, the expectation value of the perturbing Hamiltonian is equal to the correction in the energy levels. For our work, the only non-zero term for the spin-spin interaction is the ground state (orbital angular moment $l = 0$) of the hydrogen atom (Eq. (6.89) of Griffiths [2005]). Thus the energy correction is given by:

$$E_{\rm ss} = \frac{\mu_0 e^2 g_p g_e}{6\pi m_p m_e a^3} < \boldsymbol{S}_p \cdot \boldsymbol{S}_e > \tag{1.5}$$

where μ_0 is the permeability of free space, a is the Bohr radius, and $<>$ represent expectation value of a quantum operator. In the coupling of angular momenta, it is convenient to write: $\boldsymbol{S}_p \cdot \boldsymbol{S}_e = \left(S^2 - S_p^2 - S_e^2\right)/2$ where $\boldsymbol{S} = \boldsymbol{S}_p + \boldsymbol{S}_e$. The eigenvalue s of $\boldsymbol{S}$ are $|s_p - s_e|, |s_p - s_e| + 1, ..., s_p + s_e$ i.e. 0 and 1 since $s_p = s_e = 1/2$ in units of $\hbar$. For a given value of s the eigenvalues of z-component of $\boldsymbol{S}$ range from $-s$ to s for which the number of z-component eigenvalues are $2s+1$. From the number of allowed eigenvalues of $\boldsymbol{S}$ it can be noted that the spin-spin coupling of electron and proton breaks the degeneracy of the ground state of hydrogen atom and splits it into two hyperfine levels: the lower state corresponds to 0 ("anti-parallel" which is singlet since $2 \times 0 + 1 = 1$) and upper state to 1 ("parallel", a triplet since $2 \times 1 + 1 = 3$).

Further, since the electron and the proton both are spin half particles:

$$< S_p^2 >=< S_e^2 >= \frac{1}{2}\left(1+\frac{1}{2}\right)\hbar^2 = \frac{3}{4}\hbar^2. \tag{1.6}$$

With this information, the energy levels in Eq. (1.5) is given by

$$E_{\rm ss} = \frac{\mu_0 e^2 g_p g_e \hbar^2}{6\pi m_p m_e a^3}\,(s(s+1)/2-3/4) \tag{1.7}$$

$$\approx (s(s+1)/2-3/4)\times 5.88\times 10^{-6}\ \text{eV}, \tag{1.8}$$

where we have put the respective values of physical constants in the equation. Hence, the energy difference between the singlet state (s = 0) and the triplet state (s = 1) is

$$\Delta E_{\rm ss} = E_{\rm ss}(s=1) - E_{\rm ss}(s=0) = 5.88\times 10^{-6}\ \text{eV}. \tag{1.9}$$

The frequency and wavelength corresponding to the energy gap $\Delta E_{\rm ss}$ are

$$\nu_{21} \equiv \nu = \Delta E_{\rm ss}/h \approx 1420.4\ \text{MHz}$$
$$\lambda_{21} \equiv \lambda = c/\nu \approx 21.1\ \text{cm}.$$

Hence, if the electron makes a transition from triplet to singlet state in a neutral hydrogen atom, a photon of wavelength 21 cm would be emitted. The Einstein A coefficient which characterizes the rate of probability of spontaneous transition (A_{10}) is 2.85×10^{-15} sec^{-1} for the triplet to singlet state. It implies that the lifetime ($1/A_{10}$) of a hydrogen atom in the triplet state is approximately 11 million years which is very long in human timescales. Hence, in the lab conditions this transition is practically forbidden. However, in the astrophysical and cosmological settings the neutral hydrogen is the most abundant element ($\sim 74\%$) out of all the visible matter. In 1945, H. C. Van De Hulst predicted that the 21 cm radiation from neutral hydrogen atoms might be observable in the ISM (Van de Hulst [1945], Van De Hulst [1982]). The 21 cm emission line was discovered, for the first time in 1951, in the Milky-Way illuminating its spiral arms (Ewen and Purcell [1951]). Since the 21 cm line is very rare and weak in intensity, there are many physical processes in the early Universe which can affect the relative number densities of the triplet and singlet states of HI , thus affecting the 21 cm radiation observable on the earth. In the next subsection these physical processes are discussed.

1.4.2 Spin Temperature (T_s): Processes affecting the 21 cm Radiation

In the previous subsection (1.4.1) we discussed the origin of the 21 cm hyperfine radiation. Here, we study the physical processes which regulate this emission in some details. A 21 cm photon is emitted when a neutral hydrogen makes the transition from triplet to singlet state. The number of emitted photons depends on the relative number densities of HI gas in triplet and singlet states. These number densities are controlled by a characteristic temperature, called "spin temperature", of the HI gas. It is defined as:

$$\frac{n_1}{n_0} = \frac{g_1}{g_0} \exp\left(-\frac{T_*}{T_s}\right), \tag{1.10}$$

where n_1 and n_0 are the number densities of HI in the triplet and singlet states respectively, $T_* = h\nu/k_B = 0.068$ K, g_1 and g_0 are degeneracy of triplet (3) and singlet (1) states, and T_s is the spin (or excitation) temperature.

The spin temperature T_s is the temperature the HI gas would have in the thermodynamic equilibrium if the number densities of triplet and singlet states (n_1 and n_0 respectively) were related according to Eq. (1.10). The spin temperature (T_s) is not the physical temperature of the HI gas but a constructed quantity which helps us understand the HI emission in the early Universe where multiple processes play role in affecting the number densities of triplet and singlet states. There are three processes of relevance in this context, namely - interaction with background radiation (usually CMB), interaction with the Lyman-α photons, and collisions of HI atoms with other particles. We investigate them one by one below. Before we proceed further, it should be mentioned that the 21 cm radiation comes under low energy radio waves in which case the Rayleigh-Jeans limit, $h\nu \ll k_B T$, almost always holds. Under this limit it is convenient to represent a specific intensity (I) of a source with a linearly related temperature (T), called "brightness temperature", as $T = (\lambda^2/2k_B)I$, which is the temperature of a blackbody emitting same specific intensity I.

1. **Background Radiation:** The neutral hydrogen distributed in early Universe has a supply of CMB photons coming from very high redshift (1100). The CMB photons follow the blackbody (Planck's) distribution which is a continuous function at all frequencies. The CMB photons whose redshifted frequencies matches with 1420 MHz can either get absorbed or cause stimulated emission in the HI clouds along their path. It should be emphasized that such interaction with HI cloud is valid not only for CMB but also for any type of background radiation at relevant frequency. Hence, the following equations are written for a general background radiation. The transition probabilities of these transitions (absorp-

tion and spontaneous and stimulated emissions) due to a background radiation are (Field [1958]):

$$P_{01}^R = \frac{g_1}{g_0}\frac{T_R}{T_*}A_{10}, \qquad P_{10}^R = \left(1+\frac{T_R}{T_*}\right)A_{10}$$

where g_1 and g_0 are degeneracy of triplet (3) and singlet (1) states, T_R is the temperature related to the background radiation, and $T_* = h\nu/k_B = 0.068$ K. The expression of P_{01}^R is self explanatory - it represents absorption in terms of Einstein A coefficient. In the equation of P_{10}^R, the first term shows spontaneous emission and the second term stimulated emission. On combining above two equations in first order of T_*/T_R, we get

$$\frac{P_{01}^R}{P_{10}^R} \simeq \frac{g_1}{g_0}\left(1-\frac{T_*}{T_R}\right). \tag{1.11}$$

2. **The Lyman-α Photons:**

   The interaction of the Lyman-α photons emitted from luminous astrophysical objects (e.g. first stars or galaxies) with HI atoms is another way to change the number densities of the neutral hydrogen in the triplet and singlet states. In this interaction, a neutral hydrogen atom can absorb a Lyman-α photon, go to excited state ($n : 1 \Rightarrow 2$), and then may de-excite ($n : 2 \Rightarrow 1$) to a different hyperfine level in the ground state ($n = 1$). Due to the large cross section of the Lyman-α photons, they undergo a large number of scattering in HI regions before being redshifted out of the resonance width. Therefore, the colour temperature of the Lyman-α photons T_α approaches the kinetic temperature of the medium T_K. Due to the same mechanism, The excitation (or spin) temperature (T_s) of HI relaxes to T_α. Hence, the Lyman-α photons couple the spin temperature to the kinetic temperature of the medium ($T_s \to T_K$). This physical process, called "Wouthuysen-Field effect or coupling" was first suggested by Wouthuysen [1952] and was extended by Field [1958, 1959]. For this interaction, the ratio of transition probabilities are computed assuming the thermodynamic equilibrium of two hyperfine states (Field [1958, 1959]). It is given by

$$\frac{P_{01}^\alpha}{P_{10}^\alpha} = \frac{n_1}{n_0} \simeq \frac{g_1}{g_0}\left(1-\frac{T_*}{T_\alpha}\right). \tag{1.12}$$

3. **Collisions:** The third and the last physical process which alters the number densities of the triplet and singlet states is the collision of the neutral hydrogen atoms with other particles (hydrogen atom, protons, or electrons). Since the energy level gap of 21 cm radiation is very small ($\sim 5.88 \times 10^{-1}$ eV), atoms can

receive and give this small energy via kinetic collisional process. It is described by the gas kinetic temperature T_K and the ratio of transition probabilities is given as:

$$\frac{P^c_{01}}{P^c_{10}} = \frac{n_1}{n_0} \simeq \frac{g_1}{g_0}\left(1 - \frac{T_*}{T_K}\right), \tag{1.13}$$

where thermodynamic equilibrium and $T_* \ll T_K$ are assumed (Field [1958]).

Above we discussed the three physical processes which compete with each other given the conditions in the early Universe. Together they redistribute the HI atoms in its triplet and singlet states resulting the variation of spin temperature of HI gas. The concept of "detailed balance" says that these physical process are not only at equilibria individually but also collectively - the net rates of singlet-to-triplet and triplet-to-singlet transitions are equal at equilibrium. That is

$$\left(P^R_{10} + P^\alpha_{10} + P^c_{10}\right) n_1 = \left(P^R_{01} + P^\alpha_{01} + P^c_{01}\right) n_0. \tag{1.14}$$

Using Eqs. (1.10), (1.11), (1.12), (1.13) in (1.14) and assuming $T_* \ll T_s$, the expression for spin temperature T_s is found to be (Field [1958])

$$T_s = \frac{T_R + y_\alpha T_\alpha + y_c T_K}{1 + y_\alpha + y_c} \tag{1.15}$$

$$\text{with} \qquad y_\alpha = \frac{T_*}{T_\alpha}\frac{P^\alpha_{10}}{A_{10}}, \qquad y_c = \frac{T_*}{T_K}\frac{P^c_{10}}{A_{10}}, \tag{1.16}$$

where y_c and y_α are collisional and Lyman-α coupling coefficients respectively. In some literature (e.g. Pritchard and Loeb [2012]), above equation of T_s is written in a slightly different form as:

$$T_s^{-1} = \frac{T_R^{-1} + x_\alpha T_\alpha^{-1} + x_c T_K^{-1}}{1 + x_\alpha + x_c} \tag{1.17}$$

$$\text{with} \qquad x_\alpha = \frac{T_*}{T_R}\frac{P^\alpha_{10}}{A_{10}}, \qquad x_c = \frac{T_*}{T_R}\frac{P^c_{10}}{A_{10}}. \tag{1.18}$$

For our discussion we will use the expression of T_s given in Eq. (1.15). The background radiation whose effect on T_s is given by T_R is usually considered to the CMB radiation ($T_R = T_{\rm CMB}$). However, in the case of some unknown background radiation having brightness temperature T_X, its effect can be easily incorporated using $T_R = T_{\rm CMB} + T_X$ in the expression of T_s in Eq. (1.15).

1.4.3 Radiative transfer of the 21 cm Radiation

Till now we discussed the origin of the 21 cm radiation and what physical processes affect this emission. In this section we will study how the 21 cm radiation is transferred from their place of origin in the early Universe to the observers.

Consider a blob of gas having optical depth τ_ν and brightness temperature $T_{\rm source}$. This blob is illuminated by a constant source in background having brightness temperature $T_{\rm B}$. The photons from the background source traverse through the blob of gas and get absorbed, scattered, or/and re-emitted depending on their frequencies. The brightness temperature of the radiation received by an observer at the other end of the blob would be ([Rybicki and Lightman, 1979])

$$\frac{dT_{\rm B}}{d\tau_\nu} = -T_{\rm B} + T_{\rm source} \tag{1.19}$$

where the specific intensities are written in terms of temperatures assuming the Rayleigh-Jeans limit ($h\nu \ll k_B T$). Above equation is a simple linear differential equation of first order. The solution is given by

$$T_{\rm B}(\tau_\nu) = T_{\rm source}(1 - e^{-\tau_\nu}) + T_{\rm B}(\tau_\nu = 0)e^{-\tau_\nu}. \tag{1.20}$$

This is a solution to radiative transfer applicable to any type of medium and constant background source (under the Rayleigh-Jeans limit). From the solution two extreme cases can be analysed. First, in the case of optically thick medium ($\tau_\nu \gg 1 \Rightarrow e^{-\tau_\nu} \rightarrow 0$), the solution reduces to $T_{\rm B}(\tau_\nu) \approx T_{\rm source}$. It implies that the background source is almost fully suppressed by the optically thick medium (blob) and the observed emission is simply the source function of the medium itself. In the second extreme case, consider the medium is optically thin (i.e. $\tau_\nu \approx 0 \Rightarrow e^{-\tau_\nu} \rightarrow 1$) which suggests the solution would be $T_{\rm B}(\tau_\nu) \approx T_{\rm B}(\tau_\nu = 0)$. In this scenario, the medium would be transparent to the background source and the observer would receive the unaffected background emission.

In the context of the 21 cm cosmology, the background source is usually CMB ($T_{\rm B} = T_{\rm CMB}$) and $T_{\rm source} = T_s$, the spin temperature of the 21 cm line. From the observational point of view, it may not always be possible to measure $T_{\rm CMB}$ on the absolute scale. Often it is the temperature contrast, with respect to background CMB, which is measured with radio telescopes. Thus, a differential brightness temperature is defined as

$$\Delta T \equiv T_{\rm B}(\tau_\nu) - T_{\rm B}(\tau_\nu = 0) = (T_s - T_{\rm CMB})\,(1 - e^{-\tau_\nu}) \tag{1.21}$$

where $T_{\rm B} = T_{\rm CMB}$ is used. Due to expansion of the Universe, the HI emission would be redshifted by a factor of $(1+z)$ for an observer on the earth. The optical depth (τ_ν) is very small in comparison with unity, hence, on substituting $1-e^{-\tau_\nu} \simeq \tau_\nu$ and with proper variable dependence (e.g. 3-D space coordinate $\boldsymbol{r}$), the redshifted 21 cm differential brightness temperature would be

$$\Delta T_{21}(\boldsymbol{r},z) \simeq \frac{T_s(\boldsymbol{r},z) - T_{\rm CMB}(z)}{1+z}\tau_\nu(\boldsymbol{r},z). \tag{1.22}$$

The last unknown variable in the above equation is τ_ν which is a function of the position and redshift of the HI cloud. Its derivation requires formulating the absorption coefficient (as $\tau_\nu(\boldsymbol{r},z) = \int \alpha_\nu(\boldsymbol{r},z)dl$) in terms of Einstein coefficients and cosmological parameters. From Zaroubi [2013], we write the final expression for the redshifted 21 cm differential brightness temperature as

$$\Delta T_{21}(\boldsymbol{r},z) \simeq 28\,{\rm mK}(1+\delta)x_{\rm HI}\left(1-\frac{T_{\rm CMB}}{T_s}\right)\left(\frac{\Omega_b h^2}{0.0223}\right)\sqrt{\left(\frac{1+z}{10}\right)\left(\frac{0.24}{\Omega_m}\right)}\left(\frac{H(z)/(1+z)}{dv_\parallel/dr_\parallel}\right), \tag{1.23}$$

where $x_{\rm HI}$ is the HI neutral fraction, δ is the mass density contrast, h is the Hubble constant in units of 100 kms^{-1} Mpc^{-1}, $dv_\parallel/dr_\parallel$ is the line-of-sight velocity gradient , and other symbols have their usual meanings. The effect induced by line-of-sight velocity gradient is called 'redshift-space distortion'.

From Eq. (1.23) it can be noticed that ΔT_{21} is a complicated function of redshift and position capturing the effects of astrophysics and cosmology. The physical processes like reionization, cosmic expansion, temperature, evolution of matter distribution etc. compete with each other to influence the 21 cm signal (ΔT_{21}). It suggests that ΔT_{21} consists of global (sky-averaged) and fluctuating components both (discussed in next subsection). While the global signal ($\langle \Delta T_{21} \rangle$) can be detected using a monopole radio antenna (e.g. Pritchard and Loeb [2010], Bowman et al. [2018]), a low frequency ($\sim 100-200$ MHz) radio interferometer is employed to measure the fluctuating component in the form of 21 cm power spectra at various spatial scales (Bharadwaj and Sethi [2001], Morales and Wyithe [2010]). The strength of ΔT_{21} is very weak ($\lesssim 250$ mK) in comparison with systematics and other unwanted sources (e.g. foreground sources). Although a challenging endeavour, detection of both of these components are necessary to give us the complete picture of the reionization process. Hence, the 21 cm radiation of HI provides us a rich probe to study the early Universe.

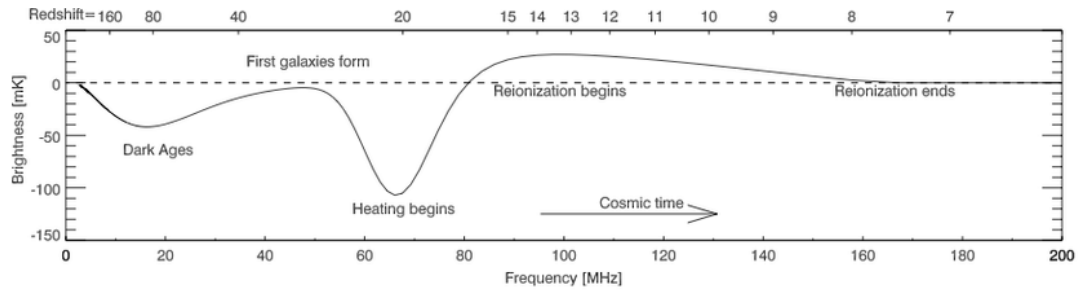

Figure 1.6: It shows a cartoon picture of the global 21 cm signal $\langle \Delta T_{21} \rangle$ as a function of redshift and observing frequency ($\nu = \nu_{21}/(1+z)$). The profile of the signal depend on the various astrophysical and cosmological events. Credit: Pritchard and Loeb [2012]

1.4.4 The Global 21 cm Signal

Here we compute the the global 21 cm signal from the derived differential brightness temperature in Eq. (1.23). It probes the temperature evolution of the IGM in the early Universe. The line-of-sight velocity gradient term is ignored for simplifying the solution. Taking the global spatial volume average (also known as 'sky-averaged' or monopole component) of ΔT_{21} in Eq. (1.23), we find

$$\langle \Delta T_{21}(\boldsymbol{r}, z) \rangle \simeq 28 \text{ mK} \langle x_{\rm HI} \rangle \left\langle \frac{T_s - T_{\rm CMB}}{T_s} \right\rangle \sqrt{\left(\frac{1+z}{10} \right)}, \tag{1.24}$$

where the cosmological parameters from Planck Collaboration et al. [2020] are used and mean of density fluctuation is zero ($\langle \delta \rangle = 0$). On of the possible profiles of the global signal is given in Figure 1.6.

Profile of the Global 21 cm Signal

The cosmic events (e.g. cosmic dawn, heating or reionization of IGM) leave their signatures on the global 21 cm signal. Since these features come from different epochs of the Universe, they affect the signal at different redshifts. A cartoon figure of the different cosmic intervals which we discuss below is shown in Figure 1.7. Before we proceed to discuss the shape of the global signal, it is important to keep in mind the variables in the expression of the 21 cm signal. In Eq. (1.24), the global 21 cm signal depends on the mean HI neutral fraction $\langle x_{\rm HI} \rangle$ and spin temperature. The spin temperature T_s is itself a function of various temperature couplings as discussed in subsection 1.4.2. In case where the spin temperature T_s is totally coupled to the background radiation i.e. $T_s = T_{\rm CMB}$, the global signal $\langle \Delta T_{21} \rangle$ is expected to be zero. For the cases $T_s > T_{\rm CMB}$ and $T_s < T_{\rm CMB}$, the global signal would be seen in emission and absorption respectively.

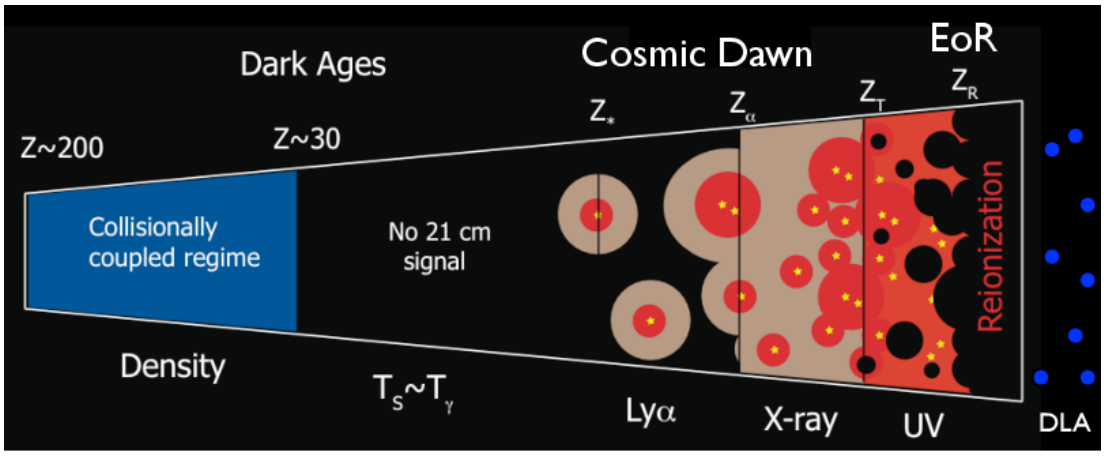

Figure 1.7: It shows different periods of the cosmic history. These events imprint their respective signatures on the global 21 cm signal. Credit: Pritchard and Loeb [2012]

- $\mathbf{1100 \gtrsim z \gtrsim 200}$ **:** This interval of the cosmic history begins at the last scattering surface of CMB which also coincides with the *epoch of recombination*. The residual free electrons from recombination maintain the thermal coupling of hydrogen atoms to background radiation (CMB) ($T_K = T_{\rm CMB}$) via Compton scattering. Since the HI number density has not fallen enough, collisional process further couples the spin temperature to the background radiation (i.e. $T_s = T_{\rm CMB}$). It implies that the mean differential brightness temperature $\langle \Delta T_{21} \rangle = 0$, hence there would not be HI radiation. Thus this regime is also called *dark ages*.

- $\mathbf{200 \gtrsim z \gtrsim 30}$ **:** The residual free electrons are no longer effective and hydrogen decouples from the background radiation (CMB). The HI gas cools adiabatically ($T_K \propto (1+z)^2$) while $T_{\rm CMB} \propto (1+z)$. Collisional process couples T_s to T_K which gives $T_s < T_{\rm CMB}$ and thus $\langle \Delta T_{21} \rangle < 0$. In this case the global 21 cm signal would be seen in absorption.

- $\mathbf{30 \gtrsim z > z_*}$ **:** The HI gas density is now low enough rendering the collisional coupling ineffective. The HI gas again couples to background radiation ($T_s = T_{\rm CMB}$) and hence $\langle \Delta T_{21} \rangle = 0$.

- $\mathbf{z_* \gtrsim z \gtrsim z_h}$ **:** The first luminous sources (e.g. stars and galaxies) form at redshift z_* which also emit X-rays and Lyman-α photons. With production of more Lyman-α photons from newer luminous sources, the neutral hydrogen gets strongly coupled via Lyman-α coupling to the gas temperature ($T_s \to T_K$). Since, $T_s = T_K < T_{\rm CMB}$ an absorption trough is expected in the global signal. Further, X-rays will heat the HI gas eventually causing gas temperature T_K to approach $T_{\rm CMB}$ by the redshift z_h.

- $\mathbf{z_h \gtrsim z > z_{\rm re}}$ **:** Due to X-ray heating, the HI gas gets hotter than background radiation ($T_s = T_K > T_{\rm CMB}$), and hence the global signal is seen in emission

($\langle \Delta T_{21} \rangle > 0$).

- $z_{\rm re} \gtrsim z$ **:** The ultraviolet (UV) photons from luminous sources ionize the HI gas surrounding them in IGM. These ionized bubbles keep growing and eventually get merged with each other. By the redshift $z_{\rm re}$ the Universe gets (almost) completely ionized. Since in this situation the HI neutral fraction becomes zero, $\langle x_{\rm HI} \rangle = 0$, the global 21 cm signal vanishes according to Eq. (1.24). After reionization of the Universe, residual neutral hydrogen HI is mostly trapped in pockets of damped Lyman-α systems.

The spin temperature T_s is the dominant variable in shaping the 21 cm signal in the early Universe ($z \gtrsim z_h$), while HI neutral fraction $x_{\rm HI}$ plays prominent role toward the last phase of the reionization ($z \lesssim z_h$).

Experimental Efforts to detect the Global 21 cm Signal

There are many running and planned single-dish radio telescopes which aim to detect the global 21 cm signal from the early Universe. Some of them include:

- Shaped Antenna measurement of the background Radio Spectrum [40-200 MHz] (SARAS; Patra et al. [2013], Singh et al. [2017, 2018a])
- Experiment to Detect the Global EoR Signature [50-200 MHz] (EDGES; Bowman et al. [2008], Bowman and Rogers [2010], Bowman et al. [2018])
- The Large-Aperture Experiment to Detect the Dark Age [30-85 MHz] (LEDA; Price et al. [2018])
- Probing Radio Intensity at high-Z from Marion [50-130 MHz] (PRI$^{\rm Z}$M; Philip et al. [2019])
- Radio Experiment for the Analysis of Cosmic Hydrogen [50-200 MHz] (REACH[1])
- Mapper of the IGM spin Temperature (MIST[2])

Even though the amplitude of the 21 cm signal is low, the required sensitivity for monopole experiments is not the issue. These endeavours are mostly limited by foreground and ionospheric contaminations and systematics. Some of these experiments put upper limits on astrophysical and cosmological parameters (e.g. Monsalve et al. [2017], Singh et al. [2017, 2018b], Bowman et al. [2018]). Bowman et al. [2018] claimed to have detected an 'absorption trough' from dark ages ($z \sim 17$) at 78 MHz (see Figure 1.8). The amplitude of the observed trough (~ 530 mK) is almost double of maximum expected from the standard models of the global 21 cm signal. While some

[1] https://www.astro.phy.cam.ac.uk/research/research-projects/reach/reach
[2] http://www.physics.mcgill.ca/mist/

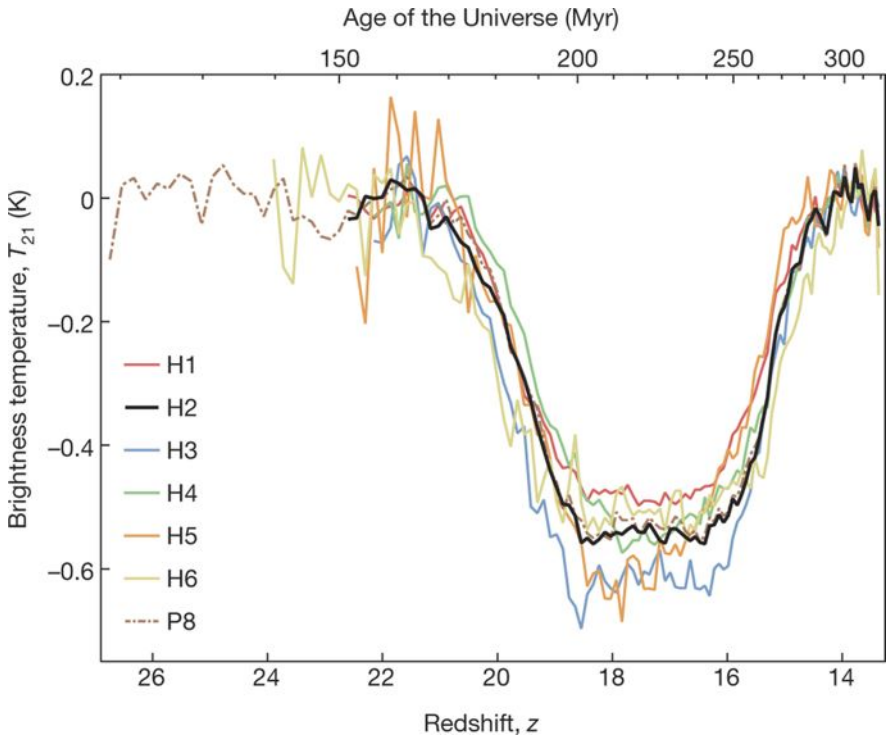

Figure 1.8: The 'absorption trough' detected by EDGES team. The depth and shape (flatness) of the signal are unexpected from the known theoretical understanding of the 21 cm cosmology. Credit: Bowman et al. [2018]

raised concerns at the detected signal (Hills et al. [2018], Sharma [2018], Singh and Subrahmanyan [2019]), others gave alternative theoretical interpretation to the anomalous profile using exotic physics and non-conventional cosmology (Barkana [2018], Fraser et al. [2018], Ewall-Wice et al. [2018]).

1.4.5 The 21 cm Power Spectrum

In the previous subsection we discussed the global (sky-averaged) 21 cm signal from high redshifts. The differential brightness temperature ΔT_{21} varies with spatial coordinates ($\boldsymbol{r}$) and redshift (z) (or observed frequency). The global signal is obtained by averaging over all space coordinates to retain only the redshift dependence of IGM temperature i.e. $\langle \Delta T_{21} \rangle (z)$. In this process the spatial details of the HI signal are averaged out. However, inhomogeneities of HI carry crucial information about structure formation and thermal and ionization history, which makes their study of paramount interest. For doing so we assume ΔT_{21} is a random variable representing a real field, then we can employ the tools of *autocorrelation function* in real space ($\boldsymbol{r}$) and *power spectrum* in Fourier space ($\boldsymbol{k}$). The random variable ΔT_{21} can be seen as a linear sum of all types of inhomogeneities or fields (Furlanetto et al. [2006a]) and hence it can be

decomposed into several sub-components as:

$$\Delta T_{21} = \beta_b \delta_b + \beta_x \delta_x + \beta_\alpha \delta_\alpha + \beta_T \delta_T - \delta_{\partial v}, \tag{1.25}$$

where β's are constants and $\delta_b, \delta_x, \delta_\alpha, \delta_T, \delta_{\partial v}$ denote spatial inhomogeneities in the baryon density, HI neutral fraction, Lyman-α radiation, kinetic temperature, and line-of-sight peculiar velocity gradient respectively. The autocorrelation function of ΔT_{21} is defined as

$$\xi(\boldsymbol{r}_1, \boldsymbol{r}_2) = \langle \Delta T_{21}(\boldsymbol{r}_1) \Delta T_{21}(\boldsymbol{r}_2) \rangle . \tag{1.26}$$

Using that the Universe is statistically homogeneous and isotropic at large scales, the autocorrelation function $\xi(\boldsymbol{r}_1, \boldsymbol{r}_2)$ reduces to $\xi(r)$ where $r = |\boldsymbol{r}_2 - \boldsymbol{r}_1|$. The autocorrelation function $\xi(r)$ of 21 cm emission encodes the information about correlation or 'sameness' of HI radiation at two points separated by a physical distance r. Statistical quantities similar to ξ can be defined in related ways depending upon the case at hand and convenience - e.g. the mean from ΔT_{21} can be subtracted before correlating and/or ξ can be normalized normalized with variance of ΔT_{21}. In this work we will use the definition given in Eq. (1.26).

The power spectrum of a scalar field represents the 'power' contained in each spatial 'frequency' ($\boldsymbol{k}$) - basically it tells us which and how many physical scales are available in the given field. If the scalar field is denoted as $\Delta T_{21}(\boldsymbol{r})$ and its Fourier transform as $\delta_{21}(\boldsymbol{k})$, then the power spectrum $P(\boldsymbol{k})$ of $\Delta T_{21}(\boldsymbol{r})$ is defined as

$$\langle \delta_{21}(\boldsymbol{k_1}) \delta_{21}(\boldsymbol{k_2}) \rangle = (2\pi)^3 \delta^3(\boldsymbol{k_2} - \boldsymbol{k_1}) P_{21}(\boldsymbol{k}) \tag{1.27}$$

where the angular brackets denote ensemble average and δ^3 is the Dirac delta function in 3-D. It can be proven that the power spectrum $P(\boldsymbol{k})$ is the spatial 3-D Fourier transform of the autocorrelation function (Wiener-Khinchin theorem):

$$P_{21}(\boldsymbol{k}) = \int \xi(\boldsymbol{r}) e^{i\boldsymbol{k}\cdot\boldsymbol{r}} d^3\boldsymbol{r}. \tag{1.28}$$

Above two expressions can be further simplified by invoking the cosmological principle (statistical homogeneity and isotropy of the Universe) in which case $P(\boldsymbol{k}) = P(|\boldsymbol{k}|) = P(k)$. However it is not correct for observations if a very large volume of the Universe is selected as the peculiar velocities and temporal evolution of the Universe break this symmetry along the line-of-sight direction.

N-body simulations, analytic and semi-analytic methods are employed to model and predict the HI signal (global and power spectrum both) from the early Universe (e.g. McQuinn et al. [2007], Santos et al. [2008], Raste and Sethi [2018], Kapahtia et al. [2018]). A typical simulated model of the HI power spectrum $P_{21}(k)$ is shown in

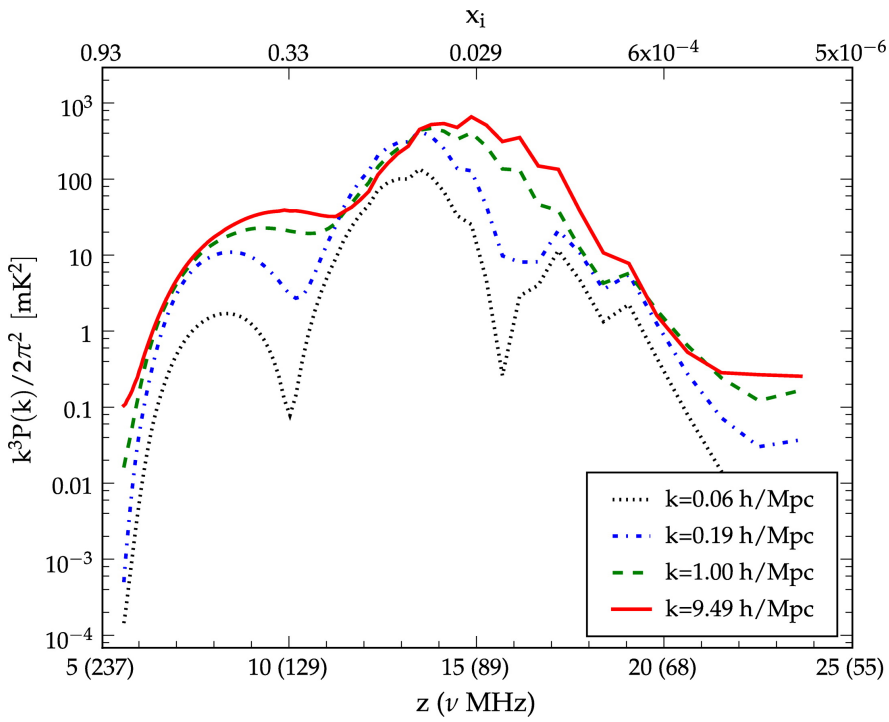

Figure 1.9: Based on simulations, the expected HI power spectrum from the early Universe is shown for many Fourier modes k against redshift (observing frequency) and ionization fraction $(1 - x_{\rm HI})$. On large scales (small k-modes), $P_{21}(k)$ has three prominent peaks due to inhomogeneities in (peaks from left to right) ionization, heating of IGM, and Lyman-α radiation respectively. Credit: Santos et al. [2008]

Figure 1.9 for many Fourier modes (k). One interesting feature of $P_{21}(k)$ is that it is expected to have three peaks on large scales (small k-modes) due to fluctuations in ionization, heating of IGM, and Lyman-α radiation. On small scales (large Fourier modes), however, the power spectrum roughly follows the square of global signal $\langle \Delta T_{21} \rangle^2$ (Santos et al. [2008]).

Many studies say that $P_{21}(k)$ from the early Universe can be observed with low-frequency radio interferometers (e.g. Morales and Hewitt [2004], Sethi [2005]). Below, we list radio telescopes which have been constructed and are planned for the near future to detect the 21 cm power spectrum $P_{21}(k)$ from the EoR.

- Giant Metrewave Radio Telescope [50-1500 MHz] (GMRT; Paciga et al. [2011])
- Hydrogen Epoch of Reionization Array [50-250 MHz] (HERA; DeBoer et al. [2017])
- Low-Frequency Array [30-240 MHz] (LOFAR; van Haarlem et al. [2013])
- Murchison Widefield Array [80-300 MHz] (MWA; Tingay et al. [2013])
- Square Kilometre Array [50-350 MHz] (SKA; Koopmans et al. [2015a])

The output of a radio interferometer is a 3-D data cube known as *visibility* which

has one real axis (observing frequency as line-of-sight direction) and two Fourier axis (baselines; on the plane of sky). Under appropriate assumptions it can be shown that the power spectrum of the redshifted HI emission from EoR is proportional to the square of frequency Fourier transform of visibility (Morales and Hewitt [2004], Parsons et al. [2012b]). The proof, corresponding assumptions etc. are discussed in detail in the next chapter.

1.5 Plan of the Thesis

The primary goal of this thesis is to develop a power spectrum analysis technique for the drift scan observations. In this chapter, we reviewed the 21 cm cosmology and described the physics behind the HI signal and how it gets affected by various effects. In the chapter 2, the observational aspects of the 21 cm cosmology are discussed including the measurements in the radio astronomy, relations between the HI power spectrum and the observation from a radio telescope, primary challenges in the detection etc. In the chapter 3, we develop a formalism to study the HI power spectrum in the drift scan observations. Next, in the chapter 4, we discuss a technique based on the results of this formalism and apply it on the drift scan data from phase I and II of the Murchison Widefield Array (MWA). In the last chapter, we summarise the thesis, make important concluding remarks, and point to the future directions of this work.

Chapter 2

Radio Astronomy in the EoR Observations

In the previous chapter we studied the epoch of reionization, its significance in cosmology, its evidence, and the 21 cm cosmology in detail. In this chapter, we will elaborate on the HI power spectrum from an observational perspective and various challenges in its detection.

2.1 Basics of Radio Astronomy

Radio astronomy is a branch of astronomy in which celestial objects and the Universe are studied at radio wavelengths ($\lambda \gtrsim 1$ cm). Since radio emission is at low energies, the wave nature of light is key to analysing these signals. Radio emission from an astronomical source was first detected by Jansky [1933][1]. Radio telescopes consist of single or multiple antennas (or elements) to collect light from the sky. The latter case utilizes the techniques of *aperture synthesis* and *interferometry*.

2.1.1 Radio Interferometry

The principle of radio interferometry is very similar to that of a Young's double-slit experiment: antennas and radio source in the sky are analogous to slits and coherent source in the double-slit experiment, respectively. Consider a plane wave from a distant source that arrives at two antennas denoted by i and j at times t and $t + \tau_g$. In radio interferometry, the electric fields of the incident wave measured by the antennas are interfered electronically. In practice, the process of digital interference involves the

[1] In radio astronomy, the unit of flux density, jansky or Jy, derives its name from Karl G. Jansky. 1 Jy $= 10^{-26}$ W m^{-2} Hz^{-1}. It is an appropriate unit to quantify radio emission from celestial sources which are usually very weak.

cross-correlation of the electric fields in time. This cross-correlation function, known as *visibility*, is given by:

$$V_\nu^{ij}(\tau_g) \equiv \left\langle E_i(\nu,t) E_j^*(\nu,t+\tau_g) \right\rangle_t , \tag{2.1}$$

where angular brackets represent averaging in time, ν is the observing frequency, τ_g is the geometric delay between arrival times of the wave at two antennas, and V_ν^{ij} is the *visibility* measured by the antenna pair $i-j$. In general, V_ν contains not only the emission from the target field but also various systematics effects, e.g. chromaticity, thermal noise, complex antenna gains, etc. The electric fields E_i and E_j are the electric fields of the same wavefront as the cross-correlation function between two different wavefronts would be zero. It should be clarified that the raw electric fields are recorded at small time intervals (typically inverse of the bandwidth) and the visibility data are output at larger intervals (say at each 0.5 s) after performing cross-correlation and time averaging defined in Eq. (2.1). The output time interval is called *integration time* or *cadence* in radio astronomy. The two processes, cross-correlation and time averaging, reduce the incoherent systematic features and thermal noise in the data.

The visibility defined in Eq. (2.1) can be related to the intensity pattern as: (Taylor et al. [1999]):

$$V_\nu(\boldsymbol{r}_i - \boldsymbol{r}_j) = \int A_\nu(\boldsymbol{\sigma}) I_\nu(\boldsymbol{\sigma}) e^{-2\pi i \nu (\boldsymbol{r}_i - \boldsymbol{r}_j)\cdot\boldsymbol{\sigma}/c} \, d\Omega, \tag{2.2}$$

the integral is all over the sky, c is the speed of light, $d\Omega$ is the infinitesimal solid angle on the sky, $\boldsymbol{r}_i$ and $\boldsymbol{r}_j$ are the position vectors of the antennas, $\boldsymbol{\sigma} = \boldsymbol{s} - \boldsymbol{s}_0$ is the angular separation from *phase tracking center* $\boldsymbol{s}_0$, $I_\nu(\boldsymbol{\sigma})$ is the specific intensity of the sky which is a function of frequency ν and the angular position vector $\boldsymbol{\sigma}$, and $A_\nu(\boldsymbol{\sigma})$ is the power pattern or the response of the antennas called *antenna beam*. $A_\nu(\boldsymbol{\sigma})$ is a dimensionless function (e.g. a Sinc^2 function or a Gaussian) on the sky intensity distribution which is normalized to one at the center ($\boldsymbol{\sigma} = 0$) and goes to zero away from the center. Theoretically, A_ν is the absolute-value-squared of the Fourier transform of the aperture illumination (Christiansen and Hoegbom [1969]). It should be noted that the visibility $V_\nu(\boldsymbol{r}_i - \boldsymbol{r}_j)$ depends on the physical separation of the two antennas, not on their absolute positions. In Figure (2.1) a two-element interferometer is shown along with relevant variables.

Next, it is often convenient to rewrite Eq. (2.2) in terms of direction cosines (l,m,n) as shown in Figure (2.1). It is given by (Taylor et al. [1999]):

$$V_\nu(u,v,w) = \int \frac{dldm}{n} A_\nu(l,m) I_\nu(l,m) e^{-2\pi i(ul+vm+(n-1)w)}, \tag{2.3}$$

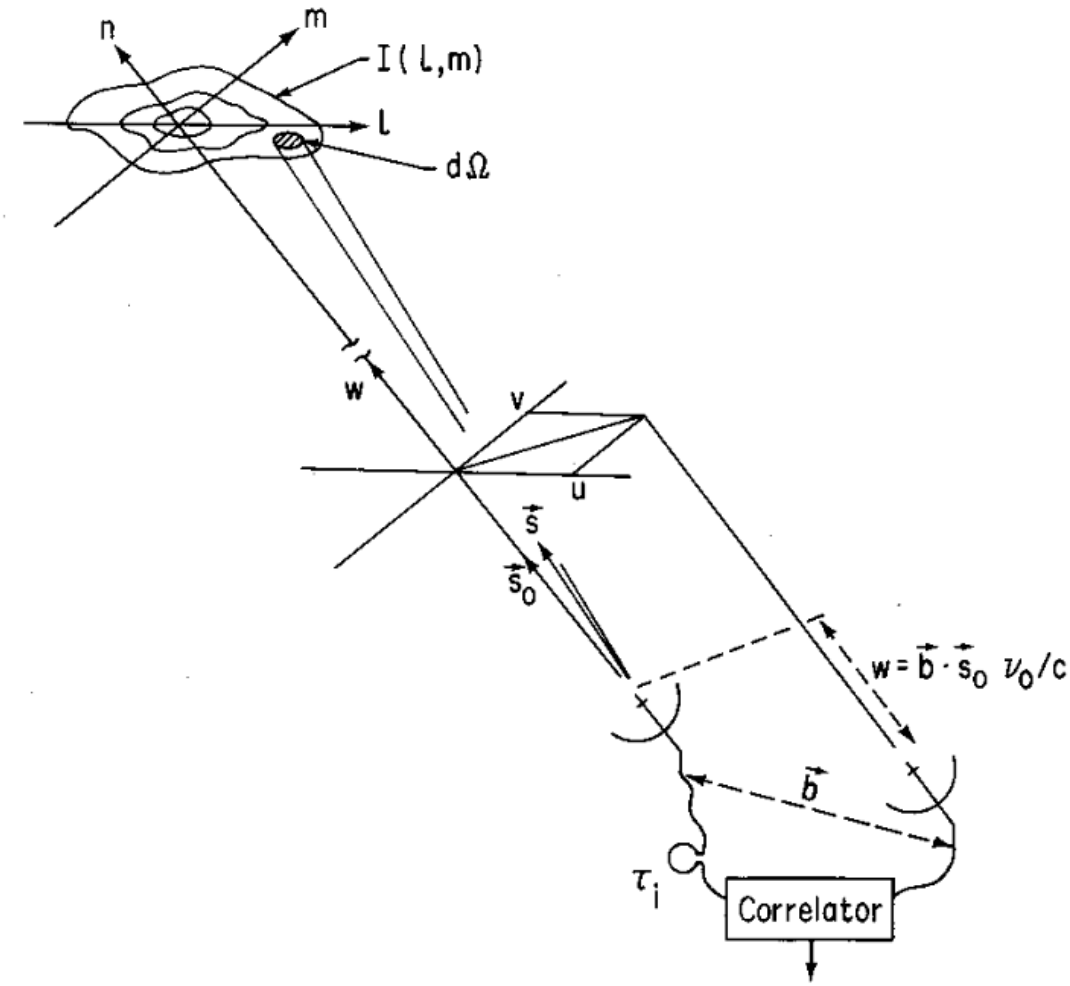

Figure 2.1: It shows the setup of the two antenna interferometer measuring intensity I_ν in the sky. Variables are given in slightly different form: baseline $\boldsymbol{b} = \boldsymbol{r}_i - \boldsymbol{r}_j$; Credit: Taylor et al. [1999].

where $n = \sqrt{1-l^2-m^2}$, $d\Omega = dldm/n$, $w = \boldsymbol{b}\cdot\boldsymbol{s}_0/\lambda$, and $ul+vm+wn = \boldsymbol{b}\cdot\boldsymbol{s}/\lambda$. This equation captures the detail of the sky intensity distribution over the full curved sky. (u,v,w) are the components of the baseline vector $\boldsymbol{b}$ in units of observing wavelength. To avoid the clutter in the equation, here we have suppressed their frequency (or wavelength) dependence - e.g. $u = (u_0/\nu_0)\nu$ - but we will use them when it is needed. The baseline components (u,v) are in the plane perpendicular to $\boldsymbol{s}_0$ and point towards local east and north respectively; w-term is along the line-of-sight (LoS) $\boldsymbol{s}_0$. In a radio interferometric observation, even though (u,v,w) may change due to the earth's rotation (see subsection 2.1.2), $u^2+v^2+w^2$ remains invariant because the physical length of the baseline between antennas ij is fixed in the coordinate transformation.

Eq. (2.3) is the fundamental equation of the radio interferometry. It relates the sky brightness $I_\nu(l,m)$ with the observed visibility $V_\nu(u,v,w)$ in terms of instrumental parameters like baseline and antenna beam. It can be further illustrated assuming the *flat sky approximation* in which $n \simeq 1$ or a small primary beam (main lobe of $A_\nu(l,m)$). In that case Eq. (2.3) becomes:

$$V_\nu(u,v) \simeq \int dldm\, A_\nu(l,m) I_\nu(l,m) e^{-2\pi i(ul+vm)}. \tag{2.4}$$

On looking carefully, we notice that the equation above is a 2-D (spatial) Fourier transform relation in which (u,v) and (l,m) are Fourier conjugate variables or *duals*. It indicates that the observed visibility $V_\nu(l,m)$ is the Fourier transformation of the sky intensity distribution $I_\nu(l,m)$ weighted by the antenna beam $A_\nu(l,m)$. Since the integrand in RHS is a product of I_ν and A_ν, convolution theorem can be applied: V_ν is the Fourier transform of I_ν convolved with the Fourier transform of A_ν.

Another point to notice is that $I_\nu(l,m)$ and $A_\nu(l,m)$ are real space functions as (l,m) are real space (angular) coordinates which means the visibility $V_\nu(u,v)$ exists in the 2-D Fourier space - its third axis frequency ν is still in real space. Thus, there must be a relation between baseline (u,v) and Fourier modes $(k_{\perp 1}, k_{\perp 2})$ on the plane of the sky. We will come back to this point a later stage when we will discuss the 21 cm power spectrum measurements.

2.1.2 Aperture Synthesis

In radio interferometry, one of the principle goals is to image the sky from the observed visibility data. These images are further used to do science of the target field e.g. studying the dynamics of neutral hydrogen gas. In principle, the imaging or map-making can be done by simply inverting the Fourier relation in Eq. (2.3). However, in reality it is not a straightforward process as it may seem and it requires some techniques.

To elucidate the concept of the aperture synthesis, we ignore A_ν in Eq. (2.3) and invert the Fourier relation. We get:

$$I_\nu(l,m) = \Delta u \Delta v \sum_{u,v} V_\nu(u,v) e^{2\pi i(ul+vm)}, \tag{2.5}$$

where we have written the equation in the discrete form and summation is over all available values of u and v. Thus, if the visibilities are measured in the uv plane, we can compute the sky intensity distribution using Eq. (2.5). Sampling of uv plane on regular grids helps in faster computation (e.g. using Fast Fourier Transform) of this equation. However, in practice, visibilities are not sampled (observed) in full uv plane due to the limited number of baselines, and hence there are gaps and irregularity in the uv space. In other words, the sampling function of the visibility is irregular and its Fourier transform[1] is convolved with the *true* image[2]. Along with the inverse Fourier transform (from (u,v) to (l,m) coordinates), the imaging process also involves deconvolution of the synthesized beam. The most famous algorithm for the deconvolution is CLEAN (Högbom [1974]). Hence, a good knowledge of the sampling function is required to construct a 'faithful' image from the observations.

To mitigate this problem of undersampling of uv space, the rotation of the earth is utilized to increase the number of unique baselines in the uv space. In tracking radio observations, the target field is tracked as the earth rotates about its axis. Since the baseline components (u,v) are projections of antenna separation vector $\boldsymbol{b}$ on to the plane perpendicular to $\boldsymbol{s}_0$ (LoS), baseline components (u,v) also change during the course of the (tracking) observation (see Figure (2.2)). Thus, the technique of aperture synthesis allows sampling of visibilities at larger number of baselines in the uv space which helps make superior images of the target field.

2.2 The HI Visibility

At this point we are equipped with the basics of radio astronomy. Now, we can apply it to the problem of the detection of the HI power spectrum from EoR. We first construct the visibility of the redshifted HI emission from EoR.

The HI emission $I(\boldsymbol{r})$ received from high redshifts depends on the position $(\boldsymbol{r})$ of the HI cloud in the Universe. Essentially, the emission is a 3-D real field (or a function): two spatial coordinates on the plane on the sky and third along the line-of-sight (LoS). The HI emission $I(\boldsymbol{r})$ is modelled as a statistically homogeneous and isotropic process

[1] In the language of radio astronomy, the Fourier transform of the sampling function or baseline distribution is called the synthesized beam.

[2] A true image convolved with the Fourier transform of the sampling function is called a *dirty image*.

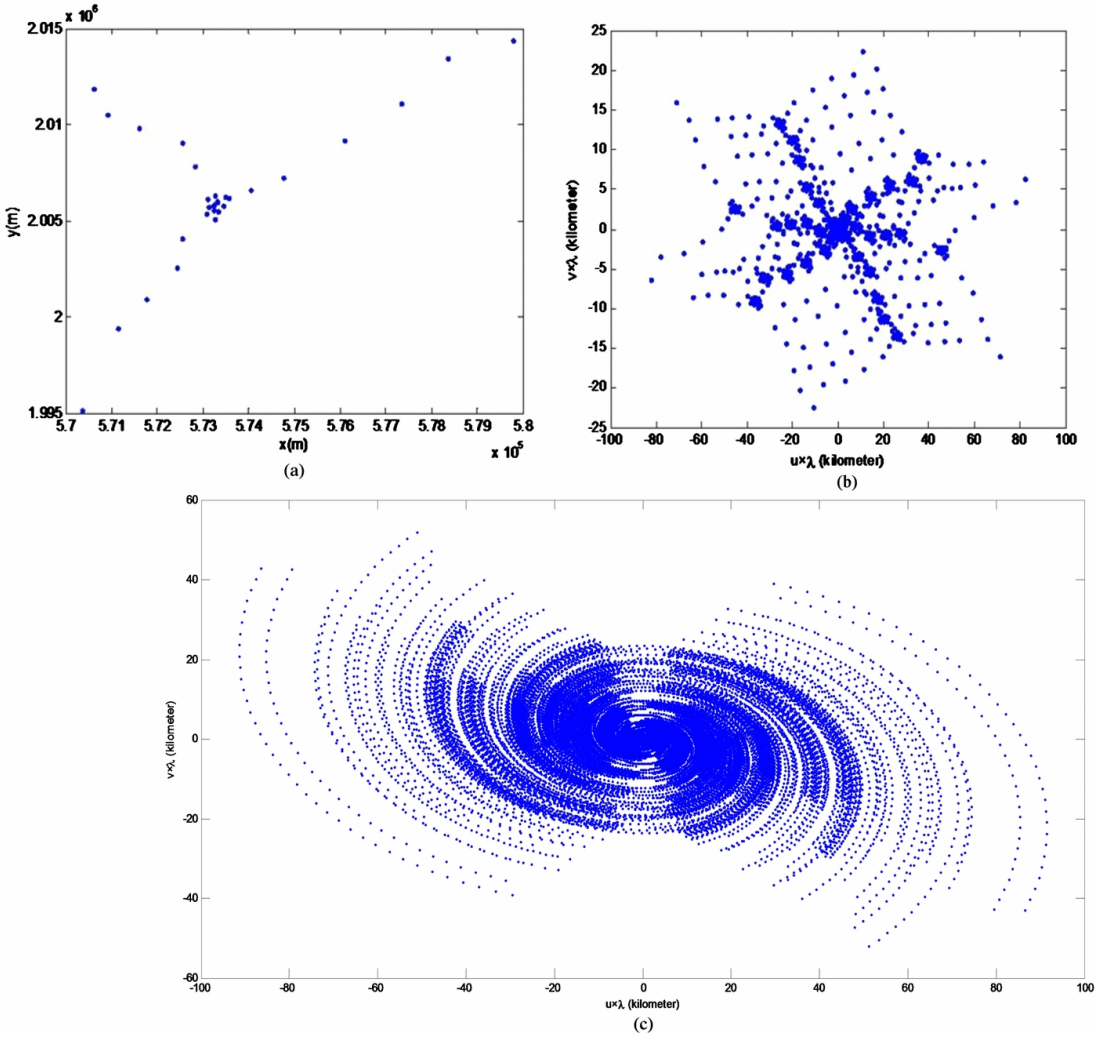

Figure 2.2: In panel (a), the physical positions of the GMRT antennas are shown. The instantaneous baseline distribution constructed from the antennas is displayed in panel (b). Due to rotation of the earth, the baselines populate the *uv* plane in an hour long tracking observation (panel (c)). In general better *uv* coverage is desired for making better images. Credit: Kiehbadroudinezhad et al. [2014].

[1]. We decompose the function characterizing the field into the mean and fluctuating components as (Bharadwaj and Sethi [2001]):

$$I(\boldsymbol{r}) = \bar{I}_\nu + \Delta I_\nu(\boldsymbol{\theta}) \tag{2.6}$$

$$\text{and} \qquad \bar{I}_\nu = \frac{A_{21} h_p c \langle n_{\rm HI} \rangle}{4\pi H(z)}, \tag{2.7}$$

where $\bar{I}_\nu$ is the mean and isotropic HI emission at frequency ν, ΔI_ν is the fluctuation on top of the mean $\bar{I}_\nu$, A_{21} is Einstein's coefficient for HI transition, $H(z)$ is the Hubble's parameter in the matter dominated Universe, h_p and c are Planck's constant and the speed of light respectively. In our analysis we ignore the peculiar motion of the sources. The observing frequency ν is the proxy for the LoS position or redshift as $\nu = \nu_0/(1+z)$. The angular vector $\boldsymbol{\theta} \equiv (l,m)$ is position on the plane perpendicular to LoS measured with respect to the phase tracking center or the center of the antenna beam.

A radio interferometer measures only the fluctuating components of the sky, the mean HI intensity $\bar{I}_\nu$ does not appear in the expression of the visibility. Thus, using Eq. (2.4) we write the visibility for HI emission as:

$$V_\nu(\boldsymbol{u}_\nu) \simeq \int d^2\boldsymbol{\theta}\, A_\nu(\boldsymbol{\theta}) \Delta I_\nu(\boldsymbol{\theta}) e^{-2\pi i\, \boldsymbol{\theta}\cdot\boldsymbol{u}_\nu}, \tag{2.8}$$

where $\boldsymbol{u}_\nu \equiv (u,v)$ is the baseline vector (frequency dependence is made explicit here). Further, the fractional intensity fluctuation $\Delta I_\nu/\bar{I}_\nu$ can be expanded in terms of its Fourier components as (Bharadwaj and Sethi [2001], Morales and Hewitt [2004]):

$$\frac{\Delta I_\nu(\boldsymbol{\theta})}{\bar{I}_\nu} = \int \frac{d^3\boldsymbol{k}}{(2\pi)^3}\, \delta_{21}(\boldsymbol{k}) e^{i\boldsymbol{k}\cdot\boldsymbol{r}} = \int \frac{d^3\boldsymbol{k}}{(2\pi)^3}\, \delta_{21}(\boldsymbol{k}) e^{ir_\nu(k_\parallel + \boldsymbol{k}_\perp\cdot\boldsymbol{\theta})} \tag{2.9}$$

where $\delta_{21}(\boldsymbol{k})$ is the same Fourier variable defined in Eq. (1.27) in section 1.4.5 which encompasses every kind of fluctuations responsible for the HI emission. The variable $\boldsymbol{r}$ is the vector position of the HI cloud in the Universe which is split into two mutually perpendicular components – along the line of sight ($\boldsymbol{k}_\parallel$) and on the plane of the sky ($\boldsymbol{k}_\perp$). On using the expression of $\Delta I_\nu(\boldsymbol{\theta})$ in Eq. (2.8), we find:

$$V_\nu(\boldsymbol{u}_\nu) = \bar{I}_\nu \int \frac{d^3\boldsymbol{k}}{(2\pi)^3}\, \delta_{21}(\boldsymbol{k}) e^{ir_\nu k_\parallel} \int d^2\boldsymbol{\theta}\, A_\nu(\boldsymbol{\theta}) e^{-2\pi i\, \boldsymbol{\theta}\cdot(\boldsymbol{u}_\nu - r_\nu \boldsymbol{k}_\perp/2\pi)}$$

$$V_\nu(\boldsymbol{u}_\nu) = \bar{I}_\nu \int \frac{d^3\boldsymbol{k}}{(2\pi)^3}\, \delta_{21}(\boldsymbol{k}) e^{ir_\nu k_\parallel} Q_\nu\left(\boldsymbol{u}_\nu - r_\nu \boldsymbol{k}_\perp/2\pi\right) \tag{2.10}$$

$$\text{with} \qquad Q_\nu(\boldsymbol{x}) \equiv \int d^2\boldsymbol{\theta}\, A_\nu(\boldsymbol{\theta}) e^{-2\pi i\, \boldsymbol{\theta}\cdot\boldsymbol{x}} \tag{2.11}$$

[1]The Gaussianity of the signal is not assumed and we expect the HI signal to be non-Gaussian (e.g. Wyithe and Morales [2007]).

where Q_ν, called *Fourier beam*, is the response of the antenna beam in the Fourier space. Notice that the Fourier beam is a function of baseline and is maximum when the exponent is zero: $\boldsymbol{k}_\perp = (2\pi/r_\nu)\boldsymbol{u}_\nu$. This relation indicates that a baseline $\boldsymbol{u}_\nu$ of a radio interferometer can probe a Fourier mode near $\boldsymbol{k}_\perp = (2\pi/r_\nu)\boldsymbol{u}_\nu$. In other words, a visibility $V_\nu(\boldsymbol{u}_\nu)$ measured with a given baseline $\boldsymbol{u}_\nu$ contains the information of the sky in 2D Fourier space near the Fourier mode $\boldsymbol{k}_\perp = (2\pi/r_\nu)\boldsymbol{u}_\nu$. Thus, the visibility, a data product of the radio interferometer, may be used to estimate the spatial power spectrum of the sky which we discuss in the next subsection.

2.3 The HI Power Spectrum

In the previous subsection, we derived the expression of the visibility for the HI emission. Here we will show how it can be used to construct the HI power spectrum of the same scalar field under some simplifying assumptions. First we recall that the expression of the spatial power spectrum which was defined in Eq. (1.27) as:

$$\langle \delta_{21}(\boldsymbol{k_1})\delta_{21}(\boldsymbol{k_2})\rangle = (2\pi)^3\delta^3(\boldsymbol{k_2}-\boldsymbol{k_1})P_{21}(\boldsymbol{k}), \tag{2.12}$$

where $P_{21}(\boldsymbol{k})$ is the quantity that we want to estimate from the radio interferometric data. Since the power spectrum exists in the 3D Fourier space, we need to transform the observed visibility into full 3D Fourier space. The only axis of the visibility $V_\nu(\boldsymbol{u}_\nu)$ data-cube which is in the real space is the frequency ν (in cosmology, the observing frequency is the proxy for the LoS distance or the redshift). We take the Fourier transform of the visibility $V_\nu(\boldsymbol{u}_\nu)$ given in Eq. (2.10) along the frequency axis[1]. We find:

$$\begin{aligned} V_\tau(\boldsymbol{u}_0) &= \int_{\nu_0-B/2}^{\nu_0+B/2} d\nu\, V_\nu(\boldsymbol{u}_\nu)e^{-2\pi i\tau\nu} \\ &= \int \frac{d^3\boldsymbol{k}}{(2\pi)^3}\,\delta_{21}(\boldsymbol{k}) \int_{\nu_0-B/2}^{\nu_0+B/2} d\nu\, \bar{I}_\nu e^{ir_\nu k_\parallel - 2\pi i\tau\nu} Q_\nu\left(\boldsymbol{u}_\nu - r_\nu\boldsymbol{k}_\perp/2\pi\right) \end{aligned}$$

where ν_0 and B denote the central frequency and the bandwidth of the observation respectively, τ is the geometric delay (in Figure (2.1) it is denoted as τ_i) and is the Fourier conjugate variable of frequency ν. $V_\tau(\boldsymbol{u}_0)$ is in 3D Fourier space and $\boldsymbol{u}_0$ represent the baseline at the central frequency ν_0, The Universe evolves with respect to the observing frequency. However, in a small bandwidth ($B \lesssim 10$ MHz), we may assume that it remains approximately constant. It allows us to Taylor expand the frequency dependent terms about the central frequency ν_0 in the first non-zero order. Furthermore, since the aim of this section is to demonstrate that the 21 cm power is related with visibilities, we also assume that the Fourier beam Q is constant in the given bandwidth

[1]This frequency Fourier transform is also called *delay transform* (Parsons et al. [2012b], Paul et al. [2014a]).

B. We get:

$$V_\tau(\boldsymbol{u}_0) \simeq \bar{I}_{\nu_0} \int \frac{d^3\boldsymbol{k}}{(2\pi)^3}\, \delta_{21}(\boldsymbol{k}) Q_{\nu_0}\left(\boldsymbol{u}_0 - \frac{r_0 \boldsymbol{k}_\perp}{2\pi}\right) e^{i(r_0 - \dot{r}_0 \nu_0)k_\parallel} \int_{\nu_0 - B/2}^{\nu_0 + B/2} d\nu\; e^{i\nu\left(\dot{r}_0 k_\parallel - 2\pi\tau\right)} \tag{2.13}$$

$$= B\bar{I}_{\nu_0} \int \frac{d^3\boldsymbol{k}}{(2\pi)^3}\, \delta_{21}(\boldsymbol{k}) Q_{\nu_0}\left(\boldsymbol{u}_0 - \frac{r_0 \boldsymbol{k}_\perp}{2\pi}\right) e^{i\left(r_0 k_\parallel - 2\pi\tau\nu_0\right)} \mathrm{sinc}\left[\left(\dot{r}_0 k_\parallel - 2\pi\tau\right) B/2\right] \tag{2.14}$$

where subscript '0' under a variable denote the value of that variable at the central frequency, $\dot{r}_\nu = \frac{dr_\nu}{d\nu} = \frac{c(1+z)^2}{\nu_{21} H(z)}$, and $\mathrm{sinc} A = \frac{\sin A}{A}$ is the *sinc* function.

Now, we have a data product $V_\tau(\boldsymbol{u}_0)$ which is in the 3D Fourier space. Next, we compute the amplitude square of this quantity and use the definition of the power spectrum given in Eq. (2.12) to get:

$$|V_\tau(\boldsymbol{u}_0)|^2 \simeq (B\bar{I}_{\nu_0})^2 \int \frac{d^3\boldsymbol{k}}{(2\pi)^3}\, P_{21}(\boldsymbol{k}) \left| Q_{\nu_0}\left(\boldsymbol{u}_0 - \frac{r_0 \boldsymbol{k}_\perp}{2\pi}\right) \mathrm{sinc}\left[\left(\dot{r}_0 k_\parallel - 2\pi\tau\right) B/2\right] \right|^2 .$$

In the above equation we note that the power spectrum is convolved with the Fourier responses of the beam and frequency band[1]. Usually these response functions are sharply peaked in the Fourier domain for the wide antenna beams. The power spectrum does not vary much over such sharp response functions. So, we can take it out of the integral[2]:

$$|V_\tau(\boldsymbol{u}_0)|^2 \simeq (B\bar{I}_{\nu_0})^2 P_{21}(\boldsymbol{k}_0) \int \frac{d^3\boldsymbol{k}}{(2\pi)^3} \left| Q_{\nu_0}\left(\boldsymbol{u}_0 - \frac{r_0 \boldsymbol{k}_\perp}{2\pi}\right) \mathrm{sinc}\left[\left(\dot{r}_0 k_\parallel - 2\pi\tau\right) B/2\right] \right|^2 ,$$

where the vector $\boldsymbol{k}_0 = (2\pi u_0/r_0, 2\pi v_0/r_0, 2\pi\tau/\dot{r}_0)$ is the measured Fourier mode (Bharadwaj and Sethi [2001], Morales and Hewitt [2004], Parsons et al. [2012b], Paul et al. [2014a]). Hence, if the antenna beam and frequency window function are known with accuracy, in principle, we can estimate the power spectrum on the Fourier mode $\boldsymbol{k}_0$ using the equation above.

The antenna beam $A_\nu(\boldsymbol{\theta})$ and the frequency window function (above, a rectangular function is used) both taper the HI intensity field along the three mutually perpendicu-

[1] In practice, often a frequency window/tapering function is used before the frequency Fourier transform to avoid the discontinuity at the end points of the visibility which otherwise causes the power leakage (Press et al. [1992]). In that case, the used frequency window function should be Fourier transformed in Eq. (2.13). An example of this is given in Eq. (3.41) where we derived a correlation function of visibilities of diffuse foreground with a Gaussian window function.

[2] Convolution with a sharply peaked function:

$$f * \delta\,(x) = \int f(y)\delta(x-y)dy = f(x)\int \delta(x-y)dy = f(x)$$

lar axes - the frequency window function along the LoS axis and the antenna beam on the plane perpendicular to the LoS. In other words, they introduce 'scales' in the problem. The consequence of this is that the triplet (u, v, τ) is not uniquely sensitive to the triplet $(2\pi u_0/r_0, 2\pi v_0/r_0, 2\pi\tau/\dot{r}_0)$ in Fourier domain but also in small vicinity around them. This correlation can be estimated analytically or numerically given the tapering functions mentioned above. It can be shown that the two baselines are correlated if $|\boldsymbol{u}_2 - \boldsymbol{u}_1| \lesssim \theta_0^{-1}$ (Bharadwaj and Sethi [2001], Paul et al. [2014a]) and two delay bins are correlated if $\tau_2 - \tau_1 \lesssim B^{-1}$ - where θ_0 is the size of the primary beam. It is worth noting that the scales of the correlations in Fourier space are inverse of the respective scales in the real space.

To clarify the point about the correlation scales, we use a simple case. The Fourier response of a constant function ($f(x) = 1$) is a Dirac δ function $\delta_D(k)$. The scale of the constant function is infinite (extends from $-\infty$ to $+\infty$), so in Fourier domain its scale is infinitesimally small. Now, we introduce a scale d in the real space by imposing a rectangular function: $f(x) = 1$ for $x \in [-d/2, d/2]$ and 0 elsewhere. It can be easily checked that the new Fourier response would be a sinc function with the width/scale proportional to d^{-1}.

In this section we made some simplifying assumptions to demonstrate that one can estimate the 21 cm power spectrum from EoR using a radio interferometer. However, it might not possible to show this analytically where the relevant assumptions break down - e.g. large bandwidth of data or very chromatic (frequency dependent) antenna beam. The chromaticity of the antenna beam and baselines also cause *mode mixing* in the power spectrum (see e.g. Vedantham et al. [2012], Parsons et al. [2012b], Thyagarajan et al. [2013], Hazelton et al. [2013], Liu et al. [2014a]). In such cases one needs to study the correlation properties of the HI visibilities against various parameters and then use them to extract the 21 cm power spectrum from the EoR data accurately.

2.4 Sensitivity

In this section, we will discuss the sensitivity of a given radio interferometer to detect the 21 cm power spectrum. The power spectrum sensitivity of an interferometer is the quantification of the minimum power the instrument can measure. Since the 21 cm power spectrum is derived from the HI visibility, the sensitivity depends on the thermal noise in the visibility and the array configuration.

The thermal noise in the visibility measured by two identical antennas is independent of the baseline but depends on the amount of radio signal collected by the antennas. It is a random variable which follows a Gaussian distribution. The standard deviation of this Gaussian distribution is given by (Wrobel and Walker [1999], Taylor et al. [1999]):

$$\sigma_{\rm th} = \frac{2k_B T_{\rm sys}}{A_{\rm eff}\sqrt{2\Delta\nu\, t_{\rm int}}}, \tag{2.15}$$

where $\Delta\nu$ is the frequency channel width, $t_{\rm int}$ is the integration time, k_B is the Boltzmann constant, $A_{\rm eff}$ is the effective collecting area of the antenna, and $T_{\rm sys}$ is the *system temperature*.

The system temperature is the sum of the total sky temperature ($T_{\rm sky}$) and the antenna receiver temperature ($T_{\rm rec}$): $T_{\rm sys} = T_{\rm sky} + T_{\rm rec}$. $T_{\rm rec}$ and $T_{\rm sky}$ both increase with decreasing frequencies. However, $T_{\rm sky}$ sharply varies with frequency as $\nu^{-(2+\alpha)}$ where α is the spectral index of the total sky emission[1] (typically $\alpha \simeq -0.8$). $T_{\rm sky}$ encompasses contribution from all types of emission other than from the instrument - e.g. atmospheric emission, galactic background, cosmic background etc. (Wrobel and Walker [1999]). It dominates over $T_{\rm rec}$ at lower frequencies ($\lesssim 200$ MHz) and thus is a major source of noise in EoR observations: for example $T_{\rm rec} \simeq 50$ K and $T_{\rm sky} \simeq 350$ K at 150 MHz for MWA (Tingay et al. [2013]).

The HI power spectrum sensitivity $\Delta^2_{\rm N}$ is a function of multiple parameters which can be tuned while designing the telescope and during the observation to achieve the better results. It is given by (Parsons et al. [2012a]):

$$\Delta^2_{\rm N}(k) \simeq 60 \left[\frac{k}{0.1h\ {\rm Mpc}^{-1}}\right]^{2.5} \left[\frac{6\ {\rm MHz}}{B}\right]^{0.5} [\Delta \ln k]^{-0.5}$$
$$\times \left[\frac{\Omega}{0.76\ {\rm str}}\right] \left[\frac{T_{\rm sys}}{500\ {\rm K}}\right]^2 \left[\frac{6\ {\rm hrs}}{t_{\rm per-day}}\right]^{0.5} \left[\frac{120\ {\rm days}}{t_{\rm days}}\right] \left[\frac{32}{N}\right] \left[\frac{10^4 f_0}{f}\right]^{0.5} {\rm mK}^2, \tag{2.16}$$

where k is the observing mode, $\Delta \ln k$ is the bin-size in k-space for averaging, Ω denote the antenna beam size, $t_{\rm per-day}$ and $t_{\rm days}$ are the duration of observation per day and total number of such days respectively, N represent the number of non-overlapping antennas in the array, and f/f_0 account for the redundancy of a baseline (see Parsons et al. [2012a] for more detailed discussion). As it can be noticed from Eq. (2.16), the EoR sensitivity of a radio interferometer can be improved by a larger collecting area, larger bandwidth, larger integration time, redundant baselines, smaller system temperature, etc.

Using Eq. (2.16) one can estimate the order of observation time required to detect the HI power spectrum from EoR. With ~ 6 hours per day and 120 days of observations, under ideal conditions for PAPER, we get $\Delta^2_{\rm N}(k) \simeq 33$ mK^2 (Parsons et al. [2012a]) for

[1] In Rayleigh-Jeans limit, the total sky specific intensity is:

$$I_\nu \propto T_\nu/\lambda^2 \Rightarrow T_\nu \propto \nu^{-(2+\alpha)},$$

if $I_\nu \propto \nu^{-\alpha}$ from the observation.

$\sim$ 720 hours of data. For other telescopes also, similar numbers have been computed: nearly $\sim$ 1000 hours of data is needed to detect the HI signal.

However, the detection is made even harder owing to strong foreground emission from galactic and extragalactic sources, radio frequency interference (RFI), ionosphere, and systematics.

2.5 Challenges in the 21 cm Power Spectrum detection

As discussed in the previous chapter, the magnitude of the HI signal is around 10 mK ($z \sim 8$) and to this level nearly $\sim$ 1000 hours of integration would be needed even in the ideal case with currently operational telescopes. In this section, we briefly highlight other sources of contamination which make the detection even harder.

2.5.1 Foreground

The foregrounds are 4 to 5 orders of magnitude brighter than the HI signal. They can be broadly divided into the following categories:

- **Extragalactic Sources:** The sources of extragalactic foreground are distant radio galaxies which emit in the frequency band of our interest. The majority of the extragalactic foreground consist of unresolved point-like sources and a few resolved extended sources. Their spatial distribution on the sky-plane follow a nearly Poissonian distribution. In radio interferometers, the long baselines are needed for the better angular resolution which help image the point sources and calibrate the data [1].

- **Diffuse Galactic Emission:** All diffuse galactic emission, such as synchrotron, free-free emission etc., are grouped together. The observations show that this combined radiation field can be described by a Gaussian random field with a smooth 2-D power spectrum in the Fourier space.

Both of the foregrounds mentioned above share a few common properties on the scales of our interest. The specific intensity from both vary smoothly along the frequency axis (e.g. Ghosh et al. [2012], Rogers and Bowman [2008], and references therein). It suggests that even though the sky-plane spatial distribution of the foregrounds are randomly distributed, they are highly correlated along the LoS direction.

On the other hand, the HI signal from EoR fluctuate in all three dimensions and thus are not strongly correlated along any axis. The distinct behaviour along the LoS is

[1] The shorter baselines are used for HI power spectrum estimation as usually they are higher in number and the HI power spectrum is expected to be stronger at those baselines.

exploited to distinguish between the HI signal and foreground emission: a Fourier transform along the frequency axis would limit the Foreground contamination at small $k_{\parallel}$ modes.

The Foreground Wedge: The foreground emission are primarily concentrated at small $k_{\parallel}$ values after the delay transform. However, since the baselines (u_ν, v_ν) are chromatic and increase with frequency, the response of the foregrounds also widens contaminating the higher $k_{\parallel}$ modes at larger baselines. In the corresponding power spectrum plot, this effect creates a bright wedge like structure of the foreground emissions (see Figure (2.3) and Liu et al. [2014b]). This phenomenon can be understood with a sinc function (an approximate response of a single point source) whose central lobe becomes wider at larger baselines. It can be shown analytically for the extragalactic point sources and the diffuse foregrounds both (see chapter 3 for detailed and general calculations). For a given baseline, the power response of a point source located at position $\boldsymbol{\theta}$ will be maximum when:

$$k_{\parallel} \simeq \frac{r_0}{\dot{r}_0 \nu_0} \boldsymbol{k}_{\perp} \cdot \boldsymbol{\theta}, \tag{2.17}$$

where the symbols have their usual meanings defined earlier. It is a equation of a plane in 3-D which reduces to a line ($k_{\parallel} \propto k_{\perp}$) in 2-D Fourier space (see Figure (2.3). Since the foreground populate all sky, the maximum slope of the line, which is the boundary of the wedge, is created by the foreground sources located at the horizon or at the end of the beam in a realistic case.

The EoR Window: Once the foreground contaminations are concentrated in the foreground wedge, the rest of the Fourier space (called EoR window) remains relatively free of the foregrounds (Figure (2.3)). In the foreground avoidance technique, only the clean modes in the EoR window are used to estimate the HI power spectrum (e.g. Chapman et al. [2014], Liu et al. [2014b]).

2.5.2 Other Challenges

Ionosphere: The ionosphere of the earth contains a layer of charged particles which interact with the incident radio waves and distort them. The opacity of the ionosphere increases at the lower frequency. The properties of the ionosphere varies across the sky and on the timescales of a few minutes to hours. This variation is higher during the day due to ionization of the particles by the radiation from the sun - this is the reason why the observations during the night time are preferred. It further implies that the telescopes with wide antenna beams require careful observation strategy. Some recent studies of the ionosphere in the context of the 21 cm cosmology can be found in Datta et al. [2014], Sokolowski et al. [2015], Arora et al. [2015], Loi et al. [2015, 2016],

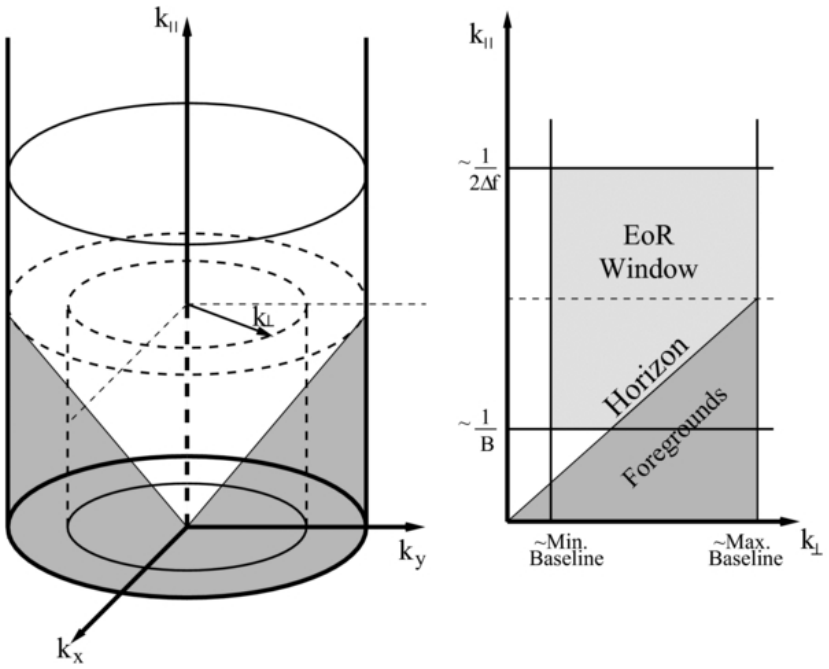

Figure 2.3: Left: The typical foreground dominated modes are shown in gray in 3-D Fourier space. Right: The 3-D space depicted in the left is averaged cylindrically for each $k_\perp = \sqrt{\boldsymbol{k}_\perp \cdot \boldsymbol{k}_\perp}$. The foreground wedge and the EoR window are also marked. Credit: Thyagarajan et al. [2013].

Jordan et al. [2017], Gehlot et al. [2018].

Radio Frequency Interference (RFI): In the frequency band of our interest (70-300 MHz), there are many sub-bands which are used for communication purposes (FM radio, mobile networks, satellites, military and aircraft related communications). Their strengths are many orders of magnitude stronger than the HI signal and foregrounds both. RFIs are dealt with by building the telescope at a radio quiet site where human activity is very low. Even in radio quiet zones, RFIs are never absent. The RFI affected frequency channels in the data are flagged before performing any kind of analysis (e.g. using AOFlagger - Offringa [2010]). The residual or ultra faint RFI in data should be mitigated for the EoR data analysis (Wilensky et al. [2019]).

Systematics: Systematics are the responses of the telescope itself. For the detection of the HI power spectrum, these systematics should be be minimal and stable. The stability of the instrument help us in dealing with the systematics in a relatively easier way. They can be largely divided into following:

- **Complex Gain Calibration:** Each antenna in a radio interferometer has a complex gain which gets multiplied to the true visibilities before they are recorded. The solutions to these antenna based complex gains are found using a sky-based, redundant-baseline, or hybrid of both calibration approaches. The sky-based calibration requires long baselines to accurately locate the point sources in the sky

so that the *closure phase* property using three antennas can be exploited (Wilkinson [1989]). On the other hand, the redundant-baseline calibration method uses identical baselines as they would measure the same signal with different complex gains (Liu et al. [2010]). For the HI power spectrum detection, the calibration solutions are needed to be accurate to the levels lower than the expected signal. Some conventional and novel calibration algorithms are discussed in Cornwell and Fomalont [1999], Fomalont and Perley [1999], Liu et al. [2010], Grobler et al. [2018], Li et al. [2018] and references therein.

- **Bandpass Calibration:** Another source of the frequency dependent system response is the frequency bandpass. Generally, the frequency channels of the bandpass are not equally sensitive to the input signal which results in the modified flux/spectrum of the target field. This issue is remedied by performing the bandpass calibration on the data using a calibrator. For this purpose, a well studied, strong, and unresolved radio source (called calibrator) is observed at start/during/at end of the target observation. Since the properties of the calibrator is already known, the change in its observed spectrum is used to do the bandpass calibration in the data.

2.6 The Murchison Widefield Array (MWA)

To avoid RFI, radio telescopes are built in the remote places which have minuscule human activities. It is particularly necessary for the telescopes dedicated for the EoR science. Some of those instruments are listed in the section 1.4.5. One of the science goals of the Square Kilometer Array (SKA), the largest radio interferometer planned for the next decade, is the EoR science (Koopmans et al. [2015b]). The MWA and the MeerKAT are the precursors of the SKA1-Low (Australia) and the SKA1-Mid (South Africa) respectively. Already operational and built at the respective sites of SKA1-Low and SKA1-Mid, the precursors are providing us invaluable lessons for the SKA. In this work, we will test our power spectrum estimation technique on the MWA data.

The Murchison Widefield Array (MWA) is a radio interferometer located in a desert of the Western Australia (26.7°S,116.7°E). It has 128 antennas (called tiles) and each tile consists of 16 crossed dipoles placed on a square mesh of side ~ 4 m in a 4x4 arrangement (see Figure 2.4). Due to the relatively small size of the tiles, the power response or the primary beam of a tile (after combining each dipole on a tile) is approximately 27°.

The MWA operates in the frequency range of 80-300 MHz with the observation bandwidth of 30 MHz and raw frequency resolution (channel width) of 40 kHz. It records visibility data files at an interval of 2 minutes with the temporal resolution of 0.5 s. In

Figure 2.4: A tile of the Murchison Widefield Array (MWA) consisting of 16 crossed-dipoles placed on a wired mesh. Credit: MWA Collaboration.

each 2-minute snapshot, the actual observation is taken for 112 s.

In the initial phase of the array (2013), the tiles were distributed in the $1/r^2$ configuration optimized for the multiple science goals. It had a compact core of the diameter $\sim$ 100 m dedicated for the EoR science and the rest of the tiles were spread over the radius of $\sim$ 1.5 km for other science goals and data calibration. The top panel of Figure 2.5 shows the antenna positions in the phase I. The phase I design and the science objectives are discussed in Tingay et al. [2013] and Bowman et al. [2013] respectively.

The phase II of the MWA became operational in 2016, in which 64 tiles were placed into two compact Hex configuration primarily to increase the sensitivity to the EoR power spectra measurements (see the bottom panel of Figure 2.5). This configuration resulted in a larger number of short baselines at the expense of the angular resolution. Wayth et al. [2018] and Beardsley et al. [2019] give details of the phase II modifications and its science goals respectively.

2.7 Summary

We conclude the ongoing chapter by summarising some of the important ideas in the observational 21 cm cosmology. In this chapter, we started with the basics of radio astronomy and discussed how a radio signal originating in the space is measured using a pair of radio antennas. We then applied the tools of radio astronomy on the redshifted HI emission from EoR and showed that a baseline is sensitive to a Fourier mode of the HI fluctuations $\delta_{21}(\boldsymbol{k})$. In principle, it is possible to measure the HI power spectrum by performing a Fourier transform (along the frequency axis) of the HI visibilities and taking the amplitude square: $|V_\tau(\boldsymbol{u}_0)|^2 \propto P_{21}(\boldsymbol{k})$. But there are multiple challenges before the detection. First, the thermal noise of the telescope (in a few observation hours) is orders of magnitude stronger than the HI signal. This problem can be overcome by integrating $>$ 1000 hours of EoR data. Second, the foreground emission from

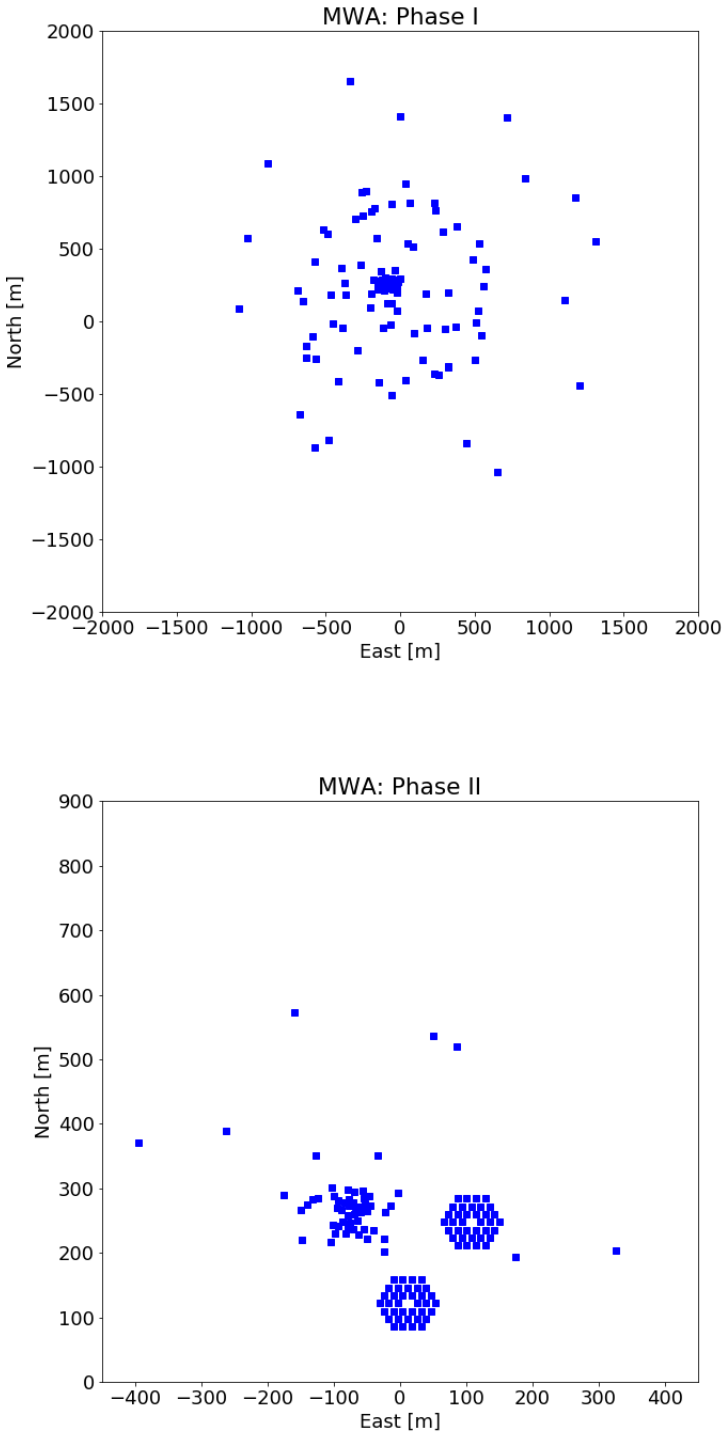

Figure 2.5: The locations of the 128 tiles in the phase I (top) and II (bottom) configurations of MWA are shown with respect to the center of the array. The phase I configuration has a compact core while other tiles are spread over a radius of $\sim$ 1.5 km. The phase II has two compact hex arrangements for the redundant baselines and rest of the tiles extend upto about 400 m from the center.

the galactic and the extragalactic radio sources are extremely bright. Fortunately, the smooth frequency-spectra of the foregrounds allow us to separate them from the HI signal. Moreover, any imperfection in the telescope contaminates the EoR window by mode-mixing. Thus the precise treatment of the contamination—either by subtraction or avoidance— is very important. Third and the last, various systematics (chromatic complex gains of the antennas, uneven bandpass, lack of system stability etc.) should also be dealt with for the accurate treatment of foregrounds and, consequently, for the detection of the HI signal.

There are multiple theoretical models of the EoR, most of which are loosely constrained. A positive detection of the HI power spectrum is necessary to break the degeneracy of the models and constrain the EoR. However, its detection is a challenging task as the expected signal is extremely faint ($\sim$ 10 mK) in comparison with the foreground contaminations ($>$ 100 K), the chromatic and unstable systematics, and the thermal noise of the telescope. A detection would require multiple efforts and different techniques to build the credibility in the results. In the next chapter, we develop a novel analytical formalism technique for the drift scan observation. This formalism is then applied on the drift scan data (154 MHz) from phase I and II of MWA to estimate the HI power spectra.

Chapter 3

Drift Scan Formalism (DSF): A Theoretical and Analytical Study [1]

3.1 Introduction

Given the weakness of the HI signal, strong foregrounds, and the requirement of hundreds of hours of integration for detection, one needs extreme stability of the system, precise calibration, and reliable isolation of foregrounds. Drift scans constitute a powerful technique to achieve instrumental stability during an observational run. During such a scan the primary beam and other instrumental parameters remain unchanged while the sky intensity pattern changes. Interferometers including MWA, HERA, CHIME, and Tianlai work in this mode while the others can also acquire data in this mode. Different variants of drift scans have been proposed in the literature: *m*-mode analysis (Shaw et al. [2014, 2015], applied to OVRO-LWA data in Eastwood et al. [2018]), cross- correlation of the HI signal in time (Paul et al. [2014a]), drift and shift method (Trott [2014]) and fringe-rate method (Parsons et al. [2016], applied to PAPER data). Trott [2014] provided a framework to estimate the uncertainty in measurement of HI power spectrum based on visibility covariance. Using simulations of visibility covariance, Lanman and Pober [2019] have shown that the sample variance can increase up to 20% and 30% on the shortest redundant baselines of HERA and MWA respectively. Owing to changing intensity pattern, it is conceptually harder to extract the HI signal from drift scans. As the HI signal is buried beneath instrumental noise, it is imperative that correct algorithm be applied to retain this sub-dominant component and prevent its loss (e.g. Cheng et al. [2018]).

In this chapter, we extend the work of Paul et al. [2014a] to delay space and, additionally, identify the effects of phase covariance and primary beam size. We also apply

[1] Based on *Patwa, A. K., Sethi, S. 2019, The Astrophysical Journal, 887, 52*

our formalism to foregrounds by considering a set of isotropically-distributed point sources and statistically homogeneous correlated diffuse emission. We work in both frequency and delay space, the preferred coordinate for separating foregrounds from the HI signal (e.g. Datta et al. [2010], Parsons et al. [2012b]). Our primary aim is to determine the correlation time scales of time-ordered visibilities of HI signal in drift scan observations. This information can be used to establish how the HI signal can be extracted from drift scans using correlation of visibilities measured at different times.

In the next section, we motivate the issue, develop our general formalism, and apply it to the HI signal in frequency and delay space. We use primary beams of PAPER, MWA, HERA, and SKA1-Low for our work. We discuss in detail analytic approximation of numerical results in the section and Appendix B. In section 3.3 we discuss the nature of foregrounds and compute the visibility correlation functions for a set of point sources and diffuse foregrounds. In section 3.4, we elaborate on how our formulation can be applied to drift scan data. We discuss many different approaches to the analysis of data including comparison with earlier attempts. In the final section, we summarize our main results.

Throughout this work, we use spatially-flat ΛCDM model with $H_0 = 100h$ Km/sec/Mpc, $h = 0.67$, $\Omega_\Lambda = 0.6911$ (Planck Collaboration et al. [2016]).

3.2 HI visibility correlation in Drift scans

The measured visibilities are a function of frequency, baseline, and time. The aim of this section is to determine the correlation structure of visibilities in these domains. In particular, our focus is on the correlation structure of visibilities as a function of time as the intensity pattern changes, for a fixed primary beam, during a drift scan.

This information allows us to average the data in the uv space with optimal signal-to-noise and prevent possible HI signal loss. The signal loss could occur if the data is averaged over scales larger than the scales of correlation (see e.g. Cheng et al. [2018]). For instance, the visibilities owing to HI signal are correlated for baselines separated by roughly the inverse of primary beam, so averaging data over pixels larger than the inverse of primary beam would result in the loss of HI signal. However, if the data is averaged using pixels much smaller than the correlation scale then it would result in sub-optimal signal-to-noise.

In this chapter, we determine the time scales over which measured visibilities (for a given baseline, etc.) are coherent in time and therefore could be averaged in a drift scan to yield optimal signal-to-noise without any loss in HI signal. For this purpose, we derive the correlation function of visibilities, arising from the EoR HI signal, measured

at two different times in a drift scan.

A pair of antennas of a radio interferometer measures the visibility V_ν, which is related to the sky intensity pattern as (Eq. 2.21 of Taylor et al. [1999]):

$$V_\nu(u_\nu, v_\nu, w_\nu) = \int \frac{dldm}{n} A_\nu(l,m) I_\nu(l,m) \exp\left[-2\pi i \left(u_\nu l + v_\nu m + w_\nu (n-1)\right)\right] \quad (3.1)$$

Here ν is the observing frequency. (u_ν, v_ν, w_ν) are the components of the baseline vector between two antennas measured in units of wavelength. (l,m,n) define the direction cosine triplet in the sky with $n = \sqrt{1-l^2-m^2}$. $A_\nu(l,m)$ is the primary beam power pattern of an antenna element and $I_\nu(l,m)$ is the specific intensity pattern in the sky. We further define vectors $\mathbf{u}_\nu = (u_\nu, v_\nu)$ and $\boldsymbol{\theta} = (l,m)$. The intensity pattern owing to the EoR HI gas distribution $I_\nu(\boldsymbol{\theta})$ can be decomposed in mean and fluctuating components as:

$$I_\nu(\boldsymbol{\theta}) = \bar{I}_\nu + \Delta I_\nu(\boldsymbol{\theta}) \quad (3.2)$$

As an interferometer measures only fluctuating components of the signal, we can write:

$$V_\nu(\mathbf{u}_\nu, w_\nu) = \int \frac{d^2\theta}{n} A_\nu(\boldsymbol{\theta}) \Delta I_\nu(\boldsymbol{\theta}) \exp\left[-2\pi i \left(\mathbf{u}_\nu \cdot \boldsymbol{\theta} + w_\nu (n-1)\right)\right] \quad (3.3)$$

The HI inhomogeneities $\delta_{\rm HI}(\mathbf{k})$ arise from various factors such as HI density fluctuations, ionization inhomogeneities, etc. The fluctuation in the specific intensity $\Delta I_\nu(\boldsymbol{\theta})$ can be related to the HI density fluctuations in the Fourier space, $\delta_{\rm HI}(\mathbf{k})$:

$$\Delta I_\nu(\boldsymbol{\theta}) = \bar{I}_\nu \int \frac{d^3k}{(2\pi)^3} \delta_{HI}(\mathbf{k}) \exp\left[i\mathbf{k}\cdot\mathbf{r}\right] \quad (3.4)$$

Here $\mathbf{r}$ is the three-dimensional (comoving) position vector and its Fourier conjugate variable is $\mathbf{k}$; k, the magnitude of the $\mathbf{k}$ vector, is $k = |\mathbf{k}| = \sqrt{k_\perp^2 + k_\parallel^2} = \sqrt{k_{\perp 1}^2 + k_{\perp 2}^2 + k_\parallel^2}$, where $\mathbf{k}_\perp$ and $k_\parallel$ are the (comoving) components on the plane of the sky and along the line of sight, respectively. The position vector $\mathbf{r}$ can be written in terms of the line of sight (parallel) and perpendicular components as $\mathbf{r} = r_\nu \hat{n} + r_\nu \boldsymbol{\theta}$; r_ν is the comoving distance. Eq. (3.4) reduces to:

$$\Delta I_\nu(\boldsymbol{\theta}) = \bar{I}_\nu \int \frac{d^3k}{(2\pi)^3} \delta_{\rm HI}(\mathbf{k}) \exp\left[i r_\nu \left(k_\parallel + \mathbf{k}_\perp \cdot \boldsymbol{\theta}\right)\right] \quad (3.5)$$

As the HI fluctuations are statistically homogeneous, we can define the HI power spec-

trum $P_{\rm HI}(k)$ as [1]:

$$\left\langle \delta_{\rm HI}(\mathbf{k})\delta^{*}_{\rm HI}(\mathbf{k}')\right\rangle = (2\pi)^3\delta^3(\mathbf{k}-\mathbf{k}')P_{\rm HI}(k) \tag{3.6}$$

In tracking observations, the primary beam of the telescope follows a particular patch of the sky. In a drift scan, the sky pattern moves with respect to the fixed primary beam. This change of the sky intensity with respect to the fixed phase center introduces a time dependent phase $\vartheta(t)$ in the expression of $\Delta I_\nu(\boldsymbol{\theta})$ in Eq. (3.5), which gives us the fluctuating component of the specific intensity as a function of time:

$$\Delta I_\nu\left(\boldsymbol{\theta},t\right) = \bar{I}_\nu \int \frac{d^3k}{(2\pi)^3}\delta_{\rm HI}(\mathbf{k})\exp\left[ir_\nu\left(k_\parallel + \mathbf{k}_\perp\cdot\left(\boldsymbol{\theta}-\boldsymbol{\vartheta}(t)\right)\right)\right] \tag{3.7}$$

In Eq. (3.3) we use the expression of $\Delta I_\nu\left(\boldsymbol{\theta},t\right)$ and expand terms containing n up to first non-zero order [2] as $d^2\theta/n \simeq d^2\theta$ and $w_\nu(n-1) \simeq -\left(l^2+m^2\right)w_\nu/2 = -\theta^2 w_\nu/2$. This gives us:

$$\begin{aligned} V_\nu(\mathbf{u}_\nu,w_\nu,t) \simeq \bar{I}_\nu \int \frac{d^3k}{(2\pi)^3}\delta_{HI}(\mathbf{k})\exp\left[ir_\nu k_\parallel\right]\int d^2\theta A_\nu(\boldsymbol{\theta}) \\ \times\exp\left[-2\pi i\left(\left(\mathbf{u}_\nu - \frac{r_\nu}{2\pi}\mathbf{k}_\perp\right)\cdot\boldsymbol{\theta} + \frac{r_\nu}{2\pi}\mathbf{k}_\perp\cdot\boldsymbol{\vartheta}(t) - \frac{1}{2}w_\nu\theta^2\right)\right] \end{aligned} \tag{3.8}$$

Next we compute the two-point visibility correlation function between two different frequencies, baselines, and times:

$$\begin{aligned} \left\langle V_\nu(\mathbf{u}_\nu,w_\nu,t)V^{*}_{\nu'}(\mathbf{u}'_{\nu'},w'_{\nu'},t')\right\rangle \simeq \bar{I}_\nu\bar{I}_{\nu'}\iint\frac{d^3k}{(2\pi)^3}\frac{d^3k'}{(2\pi)^3}\left\langle\delta_{\rm HI}(\mathbf{k})\delta^{*}_{\rm HI}(\mathbf{k}')\right\rangle \\ \times\exp\left[i\left(r_\nu k_\parallel - r_{\nu'}k'_\parallel\right)\right]\int d^2\theta A_\nu(\boldsymbol{\theta})\int d^2\theta' A_{\nu'}(\boldsymbol{\theta}') \\ \times\exp\left[-2\pi i\left[\left(\mathbf{u}_\nu - \frac{r_\nu}{2\pi}\mathbf{k}_\perp\right)\cdot\boldsymbol{\theta} - \left(\mathbf{u}'_{\nu'} - \frac{r_{\nu'}}{2\pi}\mathbf{k}'_\perp\right)\cdot\boldsymbol{\theta}' + \frac{r_\nu}{2\pi}\mathbf{k}_\perp\cdot\boldsymbol{\vartheta}(t) - \frac{r_{\nu'}}{2\pi}\mathbf{k}'_\perp\cdot\boldsymbol{\vartheta}'(t') - \frac{1}{2}w_\nu\theta^2 + \frac{1}{2}w'_{\nu'}\theta'^2\right]\right] \end{aligned} \tag{3.9}$$

Using Eq. (3.6) in Eq. (3.9) gives the two-point correlation function in terms of the HI power spectrum $P_{\rm HI}(k)$. We first note that the time dependence of Eq. (3.9) occurs as the time difference, Δt in just one term $\boldsymbol{\vartheta}'(t') - \boldsymbol{\vartheta}(t) = \Delta\boldsymbol{\vartheta}(\Delta t)$ which is obtained by dropping the frequency dependence of r_ν. This approximation is discussed in detail in the next subsection. Eq. (A.4) is used to express the time-dependent part of the

[1] We also assume here that the HI signal is statistically isotropic which allows us to write the power spectrum as a function of $|\mathbf{k}|$. Statistical isotropy is broken owing to line of sight effects such as redshift space distortion and line-cone anisotropies, which would make the power spectrum depend on the angle between $\mathbf{k}$ and the line of sight.

[2] As discussed below, we use primary beams corresponding to many ongoing and future radio telescopes for our analysis. For all the cases, this approximation holds for the main lobe of the primary beam, which means, as we show later, that our main results are unaffected.

correlation function explicitly in terms of change in the hour angle ΔH (for details see Appendix A). This gives us:

$$\left\langle V_\nu(\mathbf{u}_\nu, w_\nu, t) V^*_{\nu'}(\mathbf{u}'_{\nu'}, w'_{\nu'}, t') \right\rangle = \bar{I}_\nu \bar{I}_{\nu'} \int \frac{d^3k}{(2\pi)^3} P_{HI}(k) \exp\left[ik_\parallel (r_\nu - r_{\nu'})\right] \exp\left[ir_\nu k_{\perp 1} \cos\phi \Delta H\right] \times Q_\nu(\mathbf{k}_\perp, \mathbf{u}_\nu, w_\nu, \Delta H = 0) Q^*_{\nu'}(\mathbf{k}_\perp, \mathbf{u}'_{\nu'}, w'_{\nu'}, \Delta H) \quad (3.10)$$

Here ϕ is the latitude of the telescope and the Fourier beam (or 2D Q-integral) is defined as:

$$Q_\nu(\mathbf{k}_\perp, \mathbf{u}_\nu, w_\nu, \Delta H) = \int d^2\theta A_\nu(\boldsymbol{\theta}) \exp\left[-2\pi i \left(\boldsymbol{x}_u \cdot \boldsymbol{\theta} - \frac{1}{2} y \theta^2\right)\right] \quad (3.11)$$

with

$$x_u = u_\nu - \frac{r_\nu}{2\pi}\left(k_{\perp 1} + k_{\perp 2} \sin\phi \Delta H\right) \quad (3.12)$$

$$x_v = v_\nu - \frac{r_\nu}{2\pi}\left(k_{\perp 2} - k_{\perp 1} \sin\phi \Delta H\right) \quad (3.13)$$

$$y = w_\nu + \frac{r_\nu}{2\pi} k_{\perp 1} \cos\phi \Delta H \quad (3.14)$$

Here we consider only the zenith drift scan. Non-zenith drift scans can be treated by replacing ϕ with $\phi + \chi$, where χ is the angle between the latitude of the zenith and the phase center of the observed field (for details see Appendix A in Paul et al. [2014a]). This doesn't impact our main results. Eq. (3.10) can be numerically solved for a given primary beam pattern $A_\nu(\boldsymbol{\theta})$. We next discuss the visibility correlation in delay space, the preferred coordinate for analysing the data.

3.2.1 Visibility Correlation in Delay Space

To compute the HI visibility correlation function in delay space (τ) we define:

$$V_\tau(\mathbf{u}_0, w_0, t) = \int_{\nu_0 - B/2}^{\nu_0 + B/2} d\nu V_\nu(\mathbf{u}_\nu, w_\nu, t) \exp\left[2\pi i \tau \nu\right] \quad (3.15)$$

Throughout this thesis the subscript '0' under any variable denotes the value of that variable at the central frequency. Here we use: $\nu_0 \simeq 154$ MHz and bandpass $B \simeq 10$ MHz. Its cross-correlation in delay space can be expressed as:

$$\left\langle V_\tau(\mathbf{u}_0, w_0, t) V^*_\tau(\mathbf{u}'_0, w'_0, t') \right\rangle = \iint_{\nu_0 - B/2}^{\nu_0 + B/2} d\nu d\nu' \left\langle V_\nu(\mathbf{u}_\nu, w_\nu, t) V^*_{\nu'}(\mathbf{u}'_{\nu'}, w'_{\nu'}, t') \right\rangle e^{-2\pi i \tau \Delta\nu} \quad (3.16)$$

Eq. (3.16) can be reduced to a more tractable form by making appropriate approximations. We expand frequency-dependent variables in exponents around ν_0 up to the first order. Thus $(r_\nu - r_{\nu'}) \simeq -\dot{r}_0 \Delta\nu$, denoting $(dr_\nu/d\nu)_{\nu_0} = \dot{r}_0$, $\nu' - \nu = \Delta\nu$. To the same

order, the approximation made following Eq. (3.10) is also valid. We further approximate $\mathbf{u}_\nu \simeq \mathbf{u}_0$ and drop the weak frequency dependence of the mean specific intensity and primary beam within the observing band-width B. We discuss the impact of these approximations in section 3.2.2. This gives us:

$$\left\langle V_\tau(\mathbf{u}_0,w_0,t)V_\tau^*(\mathbf{u}_0',w_0',t')\right\rangle = \bar{I}_0^2\int\frac{d^3k}{(2\pi)^3}P_{\rm HI}(k)\exp\left[ir_0k_{\perp 1}\cos\phi\Delta H\right]\times$$
$$\left(\iint_{\nu_0-B/2}^{\nu_0+B/2}d\nu d\nu'\exp\left[-i\Delta\nu\left(k_\parallel\dot{r}_0+2\pi\tau\right)\right]\right)Q_{\nu_0}(\mathbf{k}_\perp,\mathbf{u}_0,w_0,\Delta H=0)Q_{\nu_0}^*(\mathbf{k}_\perp,\mathbf{u}_0',w_0',\Delta H) \tag{3.17}$$

The integrals over ν and ν' can be solved in two ways. They can be solved by changing the variables from (ν,ν') to (x,y). $x=\nu'-\nu=\Delta\nu$ and $y=(\nu'+\nu)/2$. They can also be solved by separating $\Delta\nu=\nu'-\nu$ and integrating over ν and ν' individually. The resulting function peaks sharply at $\tau=-\dot{r}_0k_\parallel/(2\pi)$. The major contribution to the integral in Eq. (3.17) occurs when $k_\parallel=-2\pi\tau/\dot{r}_0$, which gives us the well-known correlation scale along the line-of-sight direction (e.g. Paul et al. [2016]). We use the δ-function approximation for frequency integrals:

$$\iint_{\nu_0-B/2}^{\nu_0+B/2}d\nu d\nu'\exp\left[-i\Delta\nu\left(k_\parallel\dot{r}_0+2\pi\tau\right)\right]=B^2\,\mathrm{sinc}^2\left[\pi B\left(\tau+\frac{\dot{r}_0}{2\pi}k_\parallel\right)\right]\simeq\frac{2\pi B}{|\dot{r}_0|}\delta\left(k_\parallel-\frac{2\pi\tau}{|\dot{r}_0|}\right) \tag{3.18}$$

This approximation preserves the area under the curve. We note that the delta function approximation used in Eq. (3.18) could break down if B is small. For $B=10\,$MHz, we use in the work, it is an excellent assumption. For a much smaller B, the sinc function in the equation can be directly integrated without making any difference to our main results. We denote $\dot{r}_0=-|\dot{r}_0|$ because the comoving distance decreases with increasing frequency. Using this in Eq. (3.17) we find, with $k_\parallel=2\pi\tau/|\dot{r}_0|$:

$$\left\langle V_\tau(\mathbf{u}_0,w_0,t)V_\tau^*(\mathbf{u}_0',w_0',t')\right\rangle \simeq\bar{I}_0^2\frac{B}{|\dot{r}_0|}\int\frac{d^2k_\perp}{(2\pi)^2}P_{\rm HI}(k)\exp\left[ir_0k_{\perp 1}\cos\phi\Delta H\right]$$
$$\times Q_{\nu_0}(\mathbf{k}_\perp,\mathbf{u}_0,w_0,\Delta H=0)Q_{\nu_0}^*(\mathbf{k}_\perp,\mathbf{u}_0',w_0',\Delta H) \tag{3.19}$$

Here $k=\sqrt{k_{\perp 1}^2+k_{\perp 2}^2+(2\pi\tau/|\dot{r}_0|)^2}$. Eq. (3.19) generalizes the results of Paul et al. [2014a] to delay space and also accounts for the impact of the w-term. To further simplify Eq. (3.19) we need an expression for the primary beam pattern. We consider four radio interferometers in our analysis.

MWA: MWA has square-shaped antennas called tiles. Each tile consists of 16 dipoles placed on a mesh and arranged in a 4x4 grid at spacing of roughly 1.1 meters. Effective area of a tile $A_{\rm eff}=21.5\ \mathrm{m}^2$ at 150 MHz (Tingay et al. [2013]). The square of the

absolute value of the 2D Fourier transform of the antenna shape gives the antenna power response. For MWA $A_\nu(l,m) = \mathrm{sinc}^2(\pi L_\nu l)\,\mathrm{sinc}^2(\pi L_\nu m)$. Here $L_\nu = L(\nu/\nu_0)$; $L\left(\equiv\sqrt{A_{\rm eff}}/\lambda_0 \simeq 2.4\right)$ is the length of the square tile in units of central wavelength ($\lambda_0 \simeq 1.95$m). Therefore, the 2D primary beam response $A_\nu(l,m)$ can be represented as a product of two independent 1D patterns; $A_\nu(l,m) = A_\nu(l)A_\nu(m)$.

PAPER, HERA and SKA1-Low: Individual element in PAPER, HERA, and SKA1-Low correspond to dishes of diameter 2 meters, 14 meters, and 35 meters, respectively. The beam pattern at a frequency ν can be expressed as:

$$A_\nu = 4\left|\frac{j_1(\pi d_\nu\sqrt{l^2+m^2})}{(\pi d_\nu\sqrt{l^2+m^2})}\right|^2, \tag{3.20}$$

where $j_1(x)$ is the spherical Bessel function and d_ν is the diameter of the dish in the units of wavelength. Unlike MWA, this primary beam pattern is not separable in l and m. Or the double integral over angles in Eq. (3.11) cannot be expressed as a product of two separate integrals over l and m. We do not consider LOFAR in our analysis as its core primary beam, suitable for EoR studies, is close to SKA1-Low [1]. For MWA and SKA1-Low: $\phi = -26.7^\circ$ and for HERA and PAPER: $\phi = -30.7^\circ$.

In Figure 3.1 we show the amplitude of the correlation function (Eq. (3.19)), normalized to unity for $\Delta t = 0$, as a function of the time difference, $\Delta t \equiv t' - t$ in a drift scan. In the Figure, we use the HI power spectrum $P_{\rm HI}(k)$ given by the simulation of Furlanetto et al. [2006b]; we discuss the dependence of our results on the input power spectrum below in subsection 3.2.2. The figure displays numerical results for different primary beams as a function of baselines length $|\mathbf{u}_0| = \sqrt{u_0^2+v_0^2}$, for $w_0 = 0$ and $\tau = 0$. Our numerical results further show that the visibility correlation function in time domain is nearly independent of τ. This is discussed and justified in Appendix B using analytic approximations. Figure 3.2 complements Figure 3.1 and allows us to study the change in decorrelation time when the primary beam is changed for a fixed baseline; it will be discussed in detail in the next sub-section.

To get analytic insights into the nature of numerical results displayed in Figures 3.1 and 3.2, we consider a separable and symmetric Gaussian beam.

Fourier Beam and HI Correlation with Gaussian Beam

The Fourier Beam introduced in Eq. (3.11) is the response of the primary beam in the Fourier domain. It has two useful properties which makes the computation of the Fourier beam easier. If the primary beam is separable, $A_\nu(l,m) = A_\nu(l)A_\nu(m)$, then

[1] http://old.astron.nl/radio-observatory/astronomers/lofar-imaging-capabilities-sensitivity/lofar-imaging-capabilities/lofa

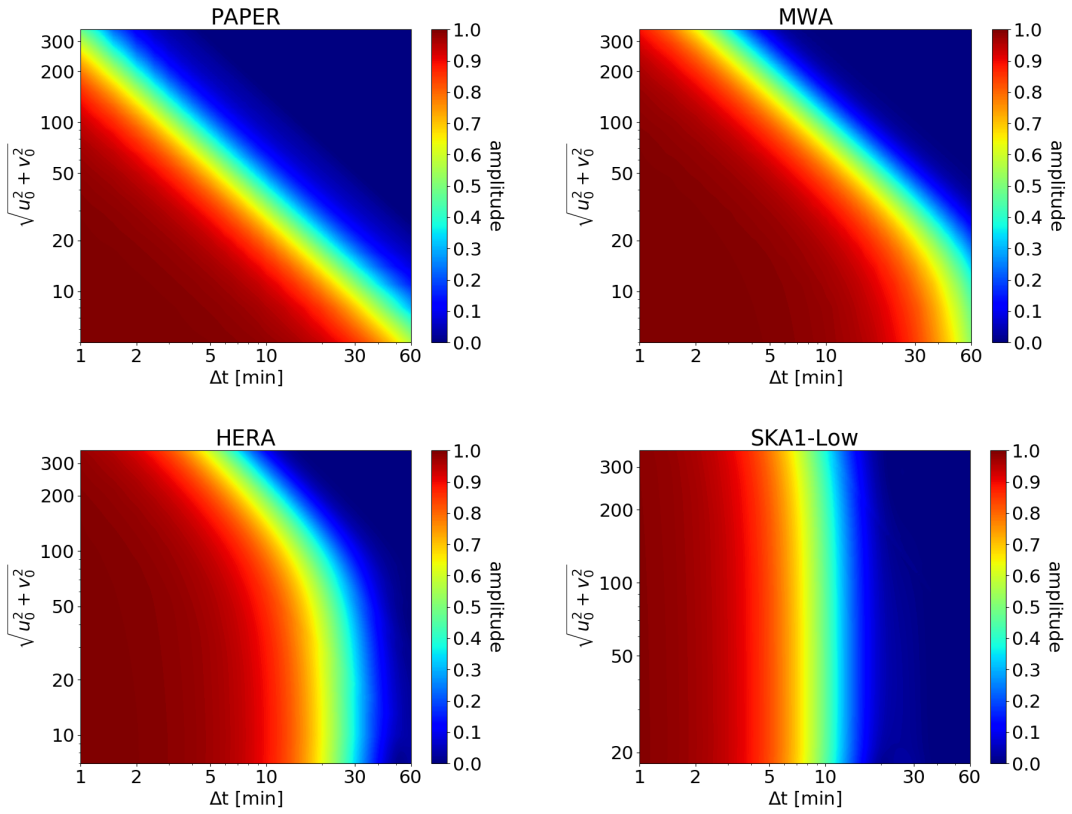

Figure 3.1: The figure displays the amplitude of the visibility correlation function as a function of Δt, normalized to unity for $\Delta t = 0$. The quantity plotted in the figure is $\langle V_\tau(\mathbf{u}_0, w_0, t) V_\tau^*(\mathbf{u}_0, w_0, t')\rangle / \langle V_\tau(\mathbf{u}_0, w_0, t) V_\tau^*(\mathbf{u}_0, w_0, t)\rangle$ as a function of baseline length $|\mathbf{u}_0| = \sqrt{u_0^2 + v_0^2}$ and $\Delta t = t' - t$, for $u_0 = v_0$, $w_0 = 0$, and $\tau = 0$. The amplitude of the correlation function decorrelates mainly due to the rotation of the intensity pattern. However the impact of the traversal of the intensity pattern becomes important for smaller primary beams on small baselines. As seen in the figure, for all baselines for PAPER and large baselines for MWA, HERA, and SKA1-Low, the decorrelation time scales are proportional to $1/|\mathbf{u}_0|$ and $1/\sqrt{\Omega}$. This effect is discussed in subsection 3.2.1 (point (b)). On smaller baselines in MWA, HERA, and SKA1-Low panels, the traversal of the intensity pattern starts dominating the decorrelation. This effect is discussed in subsection 3.2.1 (point (a)).

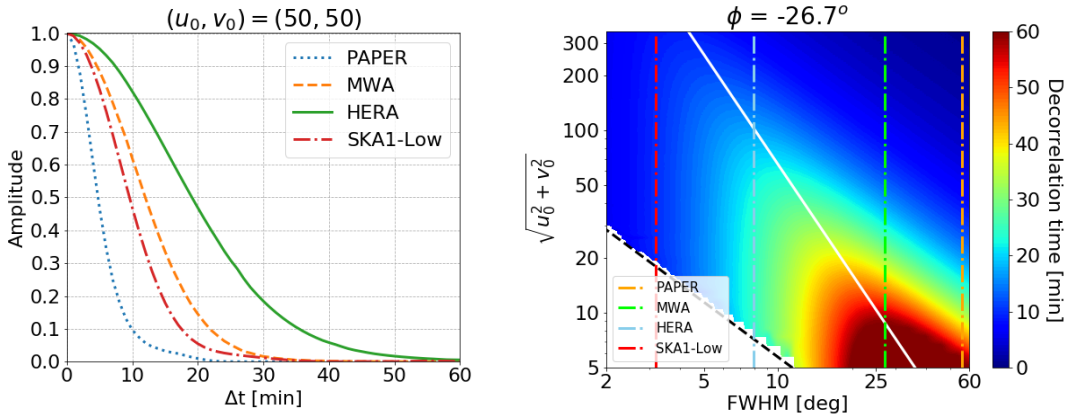

Figure 3.2: Left Panel: The amplitude of the visibility correlation function is shown as a function of Δt for a fixed baseline for different primary beams. Right Panel: The isocontours of the decorrelation time are shown in the primary beam–baseline plane; the decorrelation time is defined as Δt such that the amplitude of correlation function falls to half its value as compared to $\Delta t = 0$. The Figure assumes Gaussian beams (Eq. 3.22) with FWHM $= 2\sqrt{\log_e(2)\Omega_{0g}}$. The region on the left bottom is excluded because the shortest baseline $\sqrt{u_0^2 + v_0^2} = d_0$, where d_0 is the primary element of the telescope in units of the central wavelength, λ_0. There could be minor differences between this figure and Figure 3.1 because we use a fixed telescope latitude $\phi = -26.7$ for all primary beams. The primary beams of the four interferometers studied in this work are marked on the figure. The White line demarcates the regions dominated by rotation (above the line) and traversal of intensity pattern (for further discussion see the text).

the Fourier beam is also separable, $Q_\nu(\mathbf{u}_\nu) = Q^1_\nu(u_\nu)Q^2_\nu(v_\nu)$. And if the 1D primary beam response, $A_\nu(l)$, is an even function then the 1D Fourier beam, $Q^1_\nu(u_\nu)$, satisfies the following relations.

$$\begin{aligned} Q^1_\nu(-x_u, y) &= Q^1_\nu(x_u, y) \\ Q^1_\nu(x_u, -y) &= Q^{1*}_\nu(x_u, y) \end{aligned} \tag{3.21}$$

The expressions above are also valid for $Q^2_\nu(v_\nu)$. This shows that it is sufficient to calculate Fourier beam for only $x_u, y \geq 0$. The variables x_u, x_v, and y are defined in Eqs. (3.12)–(3.14). x_u and x_v determine the correlation scales in the neighbourhood of the Fourier mode, $2\pi\mathbf{u}_0/r_0$, at which the Q-integral receives maximum contribution. The variable y can be viewed as an effective w-term. We note that when y is small $Q^1_\nu(x_u, y)$ is large but falls very rapidly along x_u. For larger values of y, $Q^1_\nu(x_u, y)$ is smaller and goes to zero slowly along x_u. This behaviour can be understood as follows: the effective beam size shrinks for larger value of w-term, resulting in a decrease in signal strength but an increase in the correlation scale (e.g. Paul et al. [2016], Cornwell et al. [2008]).

The discussion also applies to 2D Fourier beams. The 2D Fourier beam is a function of Fourier coordinates x_u, x_v and parameter y. The point $(x_u, x_v) = (0, 0)$ receives the maximum contribution and picks out Fourier modes, $k_{\perp 1}, k_{\perp 2}$. Large beams have smaller Fourier beams e.g. for PAPER the Fourier beam is the smallest of all the cases we consider. The width of the Fourier beam decides the range of correlation scales of the HI signal. This range is roughly on the order of $2/\sqrt{\Omega} \simeq 2d$ where Ω is the primary beam solid angle and d is the antenna size in the units of wavelength. The amplitude of the Fourier beam is more sensitive to y if the beam is larger (PAPER, MWA).

To gain further analytic insights into the HI correlation function, we use a Gaussian primary beam in our formalism to compute the Fourier beam. For illustration, we choose Gaussian primary beam of solid angle Ω_{0g} at $\nu_0 = 154.24\,\mathrm{MHz}$ ($\Omega_{0g} = 0.25/L^2$ roughly matches the MWA primary beam). This gives us:

$$A_{\nu_0}(l, m) = e^{-(l^2+m^2)/\Omega_{0g}} \tag{3.22}$$

To compute the Fourier response of a Gaussian beam analytically, we extend the limits of the integral from $[-1, 1]$ to $[-\infty, \infty]$, which is a valid procedure as the integrand falls rapidly outside the support of the primary beam. Using Eq. (3.11), we obtain:

$$Q_{\nu_0}(\mathbf{k}_\perp, \mathbf{u}_0, w_0, \Delta H) = \frac{\pi\Omega_{0g}}{1 - i\pi y\Omega_{0g}} \exp\left[-\frac{\pi^2\Omega_{0g}(x_u^2 + x_v^2)}{1 - i\pi y\Omega_{0g}}\right] \tag{3.23}$$

We assume $\mathbf{u_0} = \mathbf{u_0'}$ and $\mathbf{k}_\perp = (2\pi/r_0)\mathbf{u_0}$ to study the time behaviour of the correlation function relevant in a drift scan. The time-dependent part of the visibility correlation function is determined by the product of two Fourier beams separated by drift time ΔH in Eq. (3.19). For Gaussian beam this product is:

$$Q_{\nu_0}(\Delta H = 0)Q^*_{\nu_0}(\Delta H) = \frac{(\pi\Omega_{0g})^2}{(1 - i\pi\Omega_{0g}w_0)(1 + i\pi\Omega_{0g}y)} \exp\left[-\frac{\pi^2\Omega_{0g}|\mathbf{u_0}|^2\sin^2\phi\Delta H^2}{1 - i\pi y\Omega_{0g}}\right] \tag{3.24}$$

where only the dependence on the time variable is retained in the LHS for brevity. As discussed above, $y = (w_0' + u_0\cos\phi\Delta H)$ acts as an effective w-term. For a zenith drift scan we study in this work, the w-term is small, so we put $w_0 = w_0' = 0$. We find the amplitude of the product of the Fourier beams to be:

$$|Q_{\nu_0}(\Delta H = 0)Q^*_{\nu_0}(\Delta H)| = \frac{(\pi\Omega_{0g})^2}{\sqrt{(1 + \pi^2\Omega_{0g}^2u_0^2\cos^2\phi\Delta H^2)}} \exp\left[-\frac{\pi^2\Omega_{0g}|\mathbf{u_0}|^2\sin^2\phi\Delta H^2}{1 + \pi^2\Omega_{0g}^2u_0^2\cos^2\phi\Delta H^2}\right] \tag{3.25}$$

Eq. (3.25), along with Eqs. (3.19) and (3.24), allows us to read off several salient features of the visibility correlation function in a drift scan.

Due to the rotation of the earth on its axis, the sources in the sky move with respect to the fixed phase center ($l = 0$, $m = 0$) of a telescope located at latitude ϕ. The changing intensity pattern is a combination of two motions: rotation around a fixed phase center and the east-west translation of the pattern with respect to the fixed phase center (Eq. (A.2)). In Fourier space, the rotation causes a time-dependent mixing of Fourier modes in the plane of the sky, while the translation introduces a new time-dependent phase which is proportional to $k_{\perp 1}$, the component of the Fourier mode in the east-west direction (Eq. A.4)). In addition to these two effects, which are linear in the angle, we also retain a second order term which becomes important for large beams (Eqs. (A.2) and A.4)). The impact of each of these effects on the visibility correlation function is discussed next:

(a) *Traversal time of coherence scale*: The phase term proportional to $\exp(ir_0k_{\perp 1}\cos\phi\Delta H)$ in Eq. (3.19) represents this effect. $\Delta H \simeq 1/(r_0k_{\perp 1}\cos\phi)$ is the time over which a coherent feature of linear size $1/k_{\perp 1}$ is traversed in the east-west direction. As $r_0k_{\perp 1} \simeq 2\pi u_0$, $\Delta H \simeq 1/(2\pi u_0\cos\phi)$ appears to give a rough estimate of the time over which the decorrelation occurs for a given u_0, the east-west component of the baseline. However, it doesn't give a reasonable estimate for the decorrelation time scale of the amplitude of the correlation function as Eq. (3.19) can be multiplied and divided by $\exp(i2\pi u_0\cos\phi\Delta H)$ which allows us to absorb the

fastest changing term as the phase term of the correlation function. The correlation time scale of the amplitude of the correlation function depends on the slow phase $\exp(i(r_0 k_{\perp 1} - 2\pi u_0)\cos\phi\Delta H)$ whose contribution to the visibility correlation is determined by the primary beam as we discuss below.

(b) *Rotation of intensity pattern*: This effect is captured by the numerator in the Gaussian in Eq. (3.25), which shows that the decorrelation owing to the rotation of the intensity pattern is proportional to $1/(\Omega_{0g}^{1/2}|\mathbf{u_0}||\sin\phi|)$. This effect, unlike (a), depends the magnitude of the baseline and not its east-west component. Eqs. (3.11)–(3.13), along with Eq. (A.2) and Eq. (A.4), allow us to understand this effect. When visibilities at two times are correlated for a given baseline, they respond to different Fourier modes of the HI power spectrum owing to the rotation of intensity pattern in a drift scan (Eqs. (3.11)–(3.13)). The extent of correlation of visibilities which get contribution from different Fourier modes depends on the primary beam: the smaller the primary beam the larger is the range of Fourier modes that contribute to the correlation. Therefore, the decorrelation time is proportional to $\Omega_{0g}^{-1/2}$.

(c) *Large field of view*: The terms proportional to Ω_{0g}^2 in Eq. (3.25) (or more generally the terms proportional to y in Eq. (3.23)) are responsible for this effect. These terms correspond to an effective w-term, a part of which arises from w_0 and the remaining is the higher-order time-dependent phase in a drift scan. This effect is important when the primary beam or w_0 is large. [1]

We next discuss the relative importance of (a), (b), and (c) in understanding Figures 3.1 and 3.2. We first note that (c) doesn't play an important role in explaining qualitative features seen in the Figures. Its impact is only mildly important for PAPER at the smallest baselines we consider.

For PAPER, the decorrelation time in the Figure scales linearly as the inverse of the length of the baseline $1/|\mathbf{u_0}|$. Figure 3.1 shows only the case $u_0 = v_0$. We have checked that the behaviour seen in the figure is nearly independent of the individual components of the baseline. Also a comparison of decorrelation times between PAPER and MWA shows that the decorrelation times scale as $\Omega_{0g}^{-1/2}$ for baseline $|\mathbf{u_0}| \gtrsim 25$. A comparison of these two cases with large baselines $|\mathbf{u_0}| \gtrsim 150$ for HERA and SKA1-Low also shows the same scaling with the primary beam. This means that (b) is the dominant

[1] Here we assume $w_0 = 0$ and we only consider the impact of the time-dependent term. Our assumption would be valid for a zenith drift scan, which we assume, for a near-coplanar interferometric array. Coplanarity is generally a good assumption as our focus for the detection of the HI signal is short baselines, e.g. for MWA $w_0 \ll |\mathbf{u}|$ for a zenith scan. We can gauge the quantitative impact of non-zero w_0 using Eq. (3.24). The main effect of non-zero w_0 is to yield a smaller effective primary beam (Paul et al. [2016, 2014a], Cornwell et al. [2008]) and to introduce additional phase in the visibility correlation function (Eq. (B.4)).

decorrelation mechanism in all these cases.

For short baselines for MWA, HERA, and SKA1-Low the behaviour is markedly different. If (b) alone determined the decorrelation in these cases, the decorrelation time would be longer as the primary beam is smaller in these two cases, but this behaviour is seen only for longer baselines. Therefore, (a) plays an important role in these cases. For large primary beams, (a) is unimportant because the slow phase discussed above is closer to zero, as it gets contribution from a small range of Fourier modes. However, for narrower primary beams, this term gets contribution from a larger range of Fourier modes which results in cancellation when integration over $k_{\perp 1}$ is carried out. This results in a reduction of correlation time scale. This effect is more dominant for smaller baselines for the following reason: for a given u_0, the range of Fourier modes that contribute to the visibility correlation function is $\Delta k_{\perp 1} \simeq 1/(r_0 \Omega_{0g}^{1/2})$ (i.e. size of the Fourier beam) centered around $k_{\perp 1} = 2\pi u_0 / r_0$ (e.g. Eqs. (3.11)–(3.13)). It should be noted that $\Delta k_{\perp 1}$ is only determined by the size of the primary beam while $k_{\perp 1}$ scales with the east-west component of the baseline. This implies that for long baselines, $k_{\perp 1} \gg \Delta k_{\perp 1}$. In this case, the visibility correlation function is dominated by the contribution of a single Fourier mode, which suppresses the impact of possible cancellation that occurs owing to the mixing of Fourier modes, diminishing the impact of (a) for long baselines. However, when $\Delta k_{\perp 1} \simeq k_{\perp 1}$, the effect becomes important and it determines the decorrelation time scale for shorter baselines.

For small baselines and narrower primary beams, both (a) and (b) play an important role so it is worthwhile to investigate the dependence of the decorrelation time on the components of baselines (Figure 3.1 assumes $u_0 = v_0$). We have checked many different combinations of u_0 and v_0 and find that the qualitative features of Figure 3.1 are largely determined by the the length of the baseline. But, as discussed below, the phase of the correlation function is dominated by the east-west component of the baseline.

The correlation structure in the primary-beam–Δt–baseline space is further explored in Figure 3.2. In the left panel, we show the amplitude of the correlation function as a function of Δt for a fixed baseline for different primary beams. The right panel shows the isocontours of the decorrelation time in the primary beam–baseline plane; the decorrelation time is defined as the time difference Δt at which the amplitude of the correlation function falls to half its value at $\Delta t = 0$. For each baseline, the decorrelation time reaches a maximum value as a function of the primary beam. Our formalism allows us to understand this general behaviour: for smaller primary beam, the Fourier beam is large which causes decorrelation owing to mode-mixing in the transverse motion of the intensity pattern (point (a)). For larger primary beam, the rotation of intensity pattern is responsible for the decorrelation (point (b)). The decorrelation

time scales inversely with the baseline length and could reach an hour for the shortest baselines and large primary beams, in agreement with Figure 3.1. A notable feature of Figure 3.2 is the alignment of the isocontours of decorrelation time. Its shape is determined by the interplay of decorrelation owing to the rotation and the traversal of the intensity pattern and can be derived analytically.

For large primary beams, the decorrelation time is $\simeq 1/(|\mathbf{u_0}|\Omega_{0g}^{1/2}|\sin\phi|)$ (point (b), (Eq. (3.25)); the decorrelation profile for large primary beams is seen to follow this function. For small primary beams, the decorrelation time is $\simeq \Omega_{0g}^{1/2}/\cos\phi$, nearly independent of the length of the baseline (point (a)). Equating these two expressions gives us: $\Omega_{0g}|\tan\phi|\ |\mathbf{u_0}| \simeq 1$. This relation is shown in Figure 3.2 (White line) and it separates the regions dominated by decorrelation owing to the rotation (above the White line) from the regions in which the translation plays the dominant role. Figure 3.2 shows the White line adequately captures the essential physics of the separation of the two regions. We note that the large field of view (point (c) above) does not play an important role in our study because of the range of telescope latitudes we consider, which is motivated by the location of radio interferometers studied here. For $\phi \simeq 90^\circ$, both translation and large field of view effects are negligible while, for $\phi \simeq 0$, the impact of rotation is negligible while translation and wide field of view effects dominate (Eq. (3.25)).

The phase of visibility correlation function

In the foregoing we studied the amplitude of the correlation function. As the correlation function (in either frequency or delay space Eq. (3.10) or Eq. (3.16)) is a complex function we need to know the correlation properties of its phase in addition to complete the analysis.

In Appendix B, we discuss how suitable approximations allow us to discern major contributors to the phase of the correlation function. Eqs. (B.3) and (B.4) show that the phase angle is $2\pi u_0 \cos\phi\Delta H + \psi_1 + \psi_2$. The term $2\pi u_0 \cos\phi\Delta H$ has already been discussed above (point (a) on traversal time of coherence scale). It follows from Eq. (B.4) that both ψ_1 and ψ_2 are small as compared to $2\pi u_0 \cos\phi\Delta H$ as $\psi_1 \propto \Omega_g$ and $\psi_2 \propto \Omega_g^2$ for $\pi^2\Omega_g^2 y^2 < 1$. ψ_2 can only be significant when effects arising from large field-of-view become important (Eq. (B.4) and discussion on point (c) above), which is not the case for $w_0 = 0$ and the primary beams we consider in our analysis. The dominant phase angle $2\pi u_0 \cos\phi\Delta H$ can be explicitly identified in Eq. (B.3) in this case.

Motivated by our analytic results, we define the phase angle as:

$$\psi(\mathbf{u}, t'-t) = \mathrm{Arg}\left(\exp(-i2\pi u_0 \cos\phi\Delta H)\left\langle V_\tau(\mathbf{u}_0, w_0, t)V_\tau^*(\mathbf{u}_0, w_0, t')\right\rangle\right) \qquad (3.26)$$

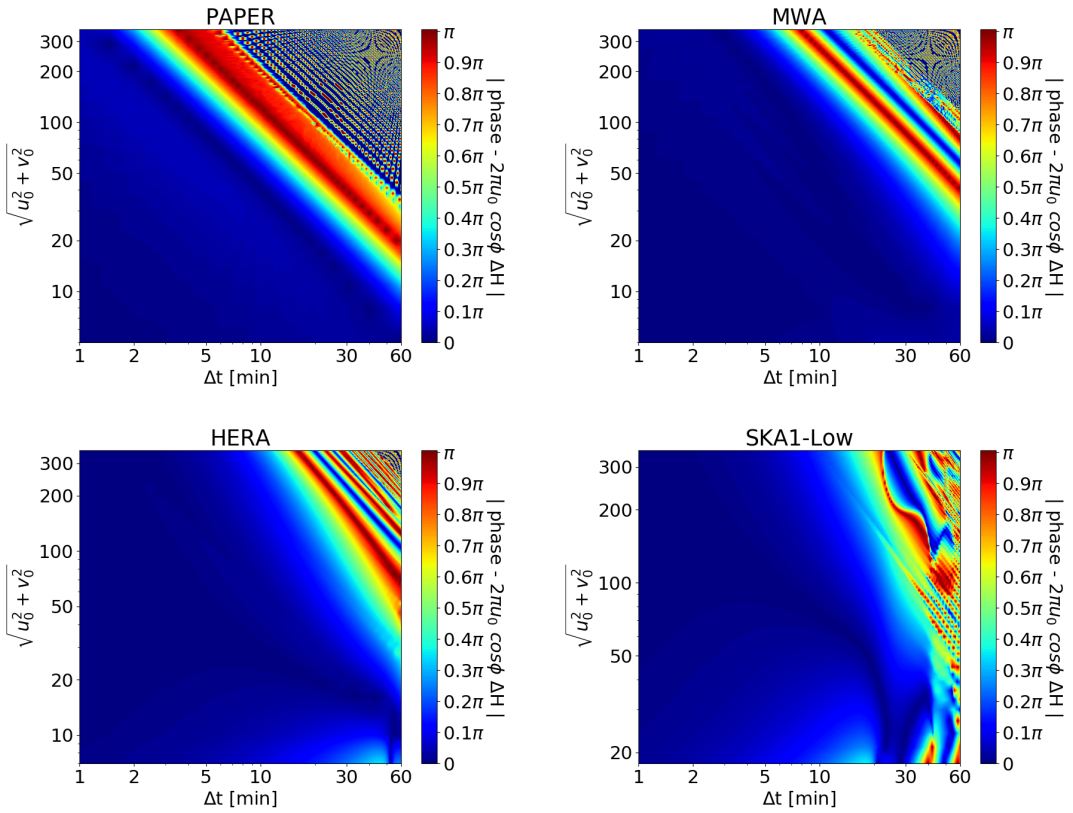

Figure 3.3: The figure shows the absolute value of the phase angle of the visibility correlation function (Eq. (3.26)) as a function of $\Delta t = t' - t$. This figure illustrates that the rapidly fluctuating component of the phase of the complex correlation function (Eq. (3.19)) can mostly be removed by multiplying it with $\exp(-i2\pi u_0 \cos\phi \Delta H)$. This allows us to determine the time scales for averaging the time-ordered visibilities in drift scans (section 3.2.1 and 3.4).

The multiplication by the additional phase allows for near cancellation of the phase term $\exp(ik_{\perp 1} r_0 \cos\phi \Delta H)$ in Eq. (3.16) (or a similar term in Eq. (3.10) for correlation in frequency space if u_0 and r_0 are replaced by u_ν and r_ν, respectively). In Figure 3.3 we present our numerical results. We notice that the phase angle defined by Eq. (3.26) is small for a wide range of Δt, as suggested by our analytic results. This means, as anticipated, that the phase of the correlation function is nearly $\exp(i2\pi u_0 \cos\phi \Delta H)$ [1]. The implication of this result for drift scan data analysis will be discussed below.

3.2.2 Approximations and input quantities

Our results use an input HI power spectrum, different primary beams, and a set of approximations to transform from frequency to delay space. We discuss the impact of these approximations and input physics on our analysis.

Dependence on input power spectrum and the shape of primary beam

The results shown in Figure 3.1 were derived using the HI power spectrum, $P(k) \simeq 1/k^n$, with $n \simeq 2$, for a range of scales (Furlanetto et al. [2006b]). We tested our results with different power-law HI power spectra with spectral indices in the range $n = 1$–3 and found our results to be insensitive to the input power spectra.

The lack of dependence of the visibility decorrelation time on the input HI power spectrum follows from our analysis. Eqs. (B.2) and (B.3) show that relevant approximations allow us to separate the input power spectrum from the time-dependent part of the correlation function, which means Figure 3.1 is independent of the HI power spectrum. These equations show that the time dependence of the correlation function is essentially captured by the response of the primary beam in Fourier space. Similar expression was derived in Parsons et al. [2016] (their equation 9) for cases when the Fourier beam (Eq. (3.11)) has a narrow response (e.g. PAPER).

The only cases not covered by this approximation are small primary beams and small baselines. However, for the limiting cases we discuss here, $|\mathbf{u}| \gtrsim 20$ and SKA1-Low primary beam, our numerical results show that the impact of the input HI power spectrum on the decorrelation time scale is negligible.

Our results are insensitive to the shape of the primary beam. We compare our numerical results for instrumental primary beams with a symmetric, separable Gaussian beam by roughly matching Ω_{0g} and the main lobe of the instrumental primary beam. We

[1] The origin of this phase can partly be explained by considering a simpler case: a single point source of flux F_ν at the phase center. In this case, the visibility $V_\nu(\mathbf{u}) = F_\nu A_\nu(0)$, where $A_\nu(0)$ defines the primary beam response at the phase center, $l = 0$ and $m = 0$. The correlation between visibilities separated by ΔH in time in a drift scan is $V_\nu(\mathbf{u}) V_\nu^*(\mathbf{u}) \simeq F_\nu^2 A_\nu^2(0) \exp(i2\pi u_\nu \cos\phi \Delta H)$. As discussed in section 3.3.1 the same factor scales out of the correlation function for a set of point sources also.

find excellent agreement in explaining the main features of Figures 3.1, 3.2 and 3.3. Eq. (B.3) adequately explains Figure 3.1, except for small baselines for HERA and SKA1-Low.

Approximations in transforming from frequency to delay space

Following Eq. (3.16) we discuss various approximations used in making the correlation function in delay space more tractable. In the tracking case, these approximations allow us to find a one-to-one linear relation between the Fourier modes of the HI signal with the variables of radio interferometers (e.g. Paul et al. [2016] and references therein). However, owing to the frequency dependence of the primary beam, the coordinate distance, and the baseline, these commonly-used relations are approximate. We assessed the impact of these approximations in Paul et al. [2016] for the tracking case. For a bandwidth $B = 10$ MHz ($\nu_0 = 154$ MHz) and MWA primary beam, the error in these relations is less than 5% for $k_\parallel \gtrsim 0.1\,\mathrm{Mpc}^{-1}$. The modes corresponding to $k_\parallel \lesssim 0.1\,\mathrm{Mpc}^{-1}$ are buried in the foreground wedge and therefore do not play a role in the detection of the HI signal (e.g. Paul et al. [2016]). The error increases with bandwidth and primary beam and therefore is expected to be smaller for HERA and SKA1-Low for the same bandwidth. As we also use these approximations in our work to separate the variables on the sky-plane from those along the line-of-sight, we re-assess these approximations for a drift scan and find these errors to be of similar magnitude for the drift scan. As in the tracking case, these approximations allow us to derive the relation between baseline and delay space parameter τ and Fourier modes of the HI signal. This simplification allows us to write the frequency-dependent terms in the form expressed in Eq. (3.17).

One outcome of this approximation for drift scans is that the functional form of the decorrelation time shown in Figure 3.1 is nearly the same in frequency and delay space. Therefore, Figure 3.1 can be interpreted as displaying the decorrelation time at the center of the bandpass. This assertion is borne out by Eq. (B.2).

Our study is based on the assumption $\nu_0 \simeq 154\,\mathrm{MHz}$ and $B \simeq 10\,\mathrm{MHz}$. It can readily be extended to a different frequency/bandpass by using Eqs. (B.2) and/or (B.3).

We discuss the approximation in transforming from frequency to delay space further with regard to foregrounds and the analysis of drift scan data in later sections (see footnote 1).

It is worthwhile to reiterate the scope of the main approximations we use: (a) For large primary beams and baselines, Eq. (B.2) provides an excellent approximation, (b) for small bandwidths and primary beams, Eq. (B.2) can readily be extended to Eq. (B.3), (c) for small baselines and primary beams, Eq. (B.2) might not be valid and Eq. (3.19)

has to be computed numerically.

3.3 Foregrounds in drift scans

In the tracking mode, the foregrounds can be isolated from the HI signal ('EoR window') by transforming to delay space if the two-dimensional foregrounds are spectrally smooth and therefore their correlation scales differ from the three-dimensional HI signal along the line of sight. However, in tracking mode, we cannot use the difference between correlation properties of foregrounds and the HI signal on the sky plane. In a drift scan, it is possible that the decorrelation time of the HI signal is different from components of foregrounds, which might give us yet another way to mitigate foregrounds.

The aim of this section is to study the decorrelation time scales of two components of foregrounds: near-isotropic distribution of point sources of flux above 1 Jy and statistically homogeneous and isotropic diffuse foregrounds. In our analysis, the delay space approach continues to be the primary method used to isolate foregrounds from the HI signal and we therefore present all our results in this space.

3.3.1 Point Sources

In a drift scan the phase center is held fixed while the intensity pattern changes. The changing intensity pattern owing to a set of point sources can be written as:

$$I_\nu(\boldsymbol{\theta},t) = \sum_m F_\nu^m \delta^2(\boldsymbol{\theta} - \boldsymbol{\theta}_m(t)) \tag{3.27}$$

Here F_ν^m is the flux of the m^{th} source and $\boldsymbol{\theta}_m(t)$ its angular position at time t. Here all the angles are measured with respect to the phase center which is assumed to be fixed at $\boldsymbol{\theta}_0 = 0$. The visibility (retaining the w-term) can readily be derived from the expression above:

$$V_\nu(\mathbf{u}_\nu, w_\nu, t) = \sum_m F_\nu^m A_\nu(\boldsymbol{\theta}_m(t)) \exp\left[-2\pi i \left(\mathbf{u}_\nu \cdot \boldsymbol{\theta}_m(t) + w_\nu(n_m(t) - 1)\right)\right] \tag{3.28}$$

To discern the main results of this section, we ignore the frequency dependence of source fluxes and primary beam, even though we allows these quantities to be frequency dependent in our simulations [1]. Using Eq. (3.15) the visibility of point sources

[1] We neglect the frequency dependence of the intensity pattern and the primary beam in this work. As we compare our analytic results against simulations in this section, it allows us to verify this assumption more explicitly. We find this assumption to be extremely good for bandwidth $B \simeq 10\,\text{MHz}$ around a central frequency of $\nu_0 \simeq 154\,\text{MHz}$. This approximation can be understood by considering a simpler case: a flat spectrum source at the phase center. While transforming to delay space, this source receives contribution from only the $\tau = 0$ mode. If the source is now assumed to have a spectral index, more

in the delay space is:

$$V_\tau(\mathbf{u}_0, w_0, t) \simeq \sum_m F_0^m A_0(\boldsymbol{\theta}_m(t)) B \,\mathrm{sinc}(\pi B \bar{\tau}^m(t)) e^{2\pi i \nu_0 \bar{\tau}^m(t)} \tag{3.29}$$

$$\text{where,} \qquad \bar{\tau}^m(t) = \tau - \frac{1}{\nu_0}\left(\mathbf{u}_0 \cdot \boldsymbol{\theta}_m(t) + w_0(n_m(t) - 1)\right) \tag{3.30}$$

The correlation function of the visibilities in delay space can be written as:

$$\begin{aligned}\left\langle V_\tau(\mathbf{u}_0, w_0, t) V_\tau^*(\mathbf{u}_0, w_0, t')\right\rangle \simeq B^2 \sum_m \sum_n F_0^m F_0^n A_0(\boldsymbol{\theta}_m(t)) A_0(\boldsymbol{\theta}_n(t')) \\ \times \,\mathrm{sinc}(\pi B \bar{\tau}^m(t)) \,\mathrm{sinc}(\pi B \bar{\tau}^n(t')) e^{2\pi i \nu_0 (\bar{\tau}^m(t) - \bar{\tau}^n(t'))}\end{aligned} \tag{3.31}$$

Here the ensemble average implies averages over all pairs of baselines and times for which $|\mathbf{u}_0|$ and $t' - t$ are held fixed. To understand Eq. (3.31) we first consider the tracking case in which source positions are independent of time. In this case the dominant contribution comes from $\tau = 2\pi \mathbf{u}_0.\boldsymbol{\theta}_m/\nu_0$. This defines the so-called foreground wedge which is bounded by the maximum value of θ_m which is given approximately by the size of the primary beam. It also follows from the equation that the sum is dominated by terms for which $m = n$ because for $m = n$ the phase term (exponent term) becomes small and thus causing lesser cancellations in the summation.

In a drift scan the source position changes with respect to the primary beam. It means the value of τ for which the sum in Eq. (3.31) peaks changes with time. While the broad wedge structure is the same in this case as in the tracking case as the dominant contribution comes from sources within the primary beam, the correlation structure becomes more complicated. As $\boldsymbol{\theta}_n(t') - \boldsymbol{\theta}_m(t)$ remains unchanged during a drift scan, the summation in this case would also generally be dominated by $m = n$ terms. However, it is possible that a source at one position at a time drifts close to the position of another source at another time. Even though the contribution of this pair could be negligible in tracking mode, it would not be if the visibilities are correlated at two different times. The impact of this effect requires details of point source distribution which we model using a simulation in this study.

For the case of $m = n$, the same source is correlated at two different times. In this case, it follows from Eq. (3.31) that the visibility correlation diminishes as the time separation increases due to the larger and different arguments of the two Sinc functions. As the additional time-dependent phase acquired in the drift is proportional to the

delay space modes close to $\tau = 0$ begin to contribute. We find that these modes do not contaminate the EoR window as they lie well within the wedge given the bandwidth and spectral index of interest. The leakage into the EoR window owing to finite bandwidth can be assuaged by using a frequency-space convolving function such as Blackman-Nuttall window or a Gaussian window we discuss in the section on diffuse foregrounds. The frequency dependence of baselines in the phase plays a more important role and is needed to explain the wedge structure for foregrounds (e.g. Paul et al. [2016]).

length of the baseline, the decorrelation time scale is expected to be shorter for longer baselines.

Point source simulations: We generate 15067 point sources brighter than 1 Jy distributed isotropically on the southern hemisphere (Hopkins et al. [2003]). We assume the spectral index of sources to be -0.7[1] For this source distribution we compute the power spectrum in delay space as a function of drift time. In a drift scan, the coordinates of these sources evolve according to Eq. (A.2) with respect to the fixed phase center.

We compute visibilities in delay space for a one-hour drift scan in the steps of 30 seconds. The visibilities are then correlated in time and the visibility correlation function is computed by averaging over the number of correlation pairs for which $t'-t$ and $|\mathbf{u}_0|$ are held fixed:

$$\left\langle V_\tau(\mathbf{u}_0,w_0,t)V_\tau^*(\mathbf{u}_0',w_0',t')\right\rangle = \frac{1}{N_{|\mathbf{u}_0|}}\sum_{|\mathbf{u}_0|}^{N_{|\mathbf{u}_0|}}\frac{1}{N_{tt'}}\sum_{t,t'}^{N_{tt'}}V_\tau(\mathbf{u}_0,w_0,t)V_\tau^*(\mathbf{u}_0',w_0',t') \tag{3.32}$$

Here $N_{|\mathbf{u}_0|}$ and $N_{tt'}$ and the number of baseline pairs for fixed $|\mathbf{u}_0|$ and $t-t'$, respectively.

To establish how the amplitude of the visibility correlation behaves as a function of time, baselines, and the number of points over which the average is computed, we choose two representative baselines $|\mathbf{u}_0| = 20, 100$. We carry out averages in a ring of width $\Delta|\mathbf{u}_0| = 4$ at every 30 seconds; each of these rings is populated, randomly and uniformly, with $N_{|\mathbf{u}_0|} = 25, 50, 100, 200, 400$. The observed *uv*-field and its baseline distributions of MWA phase I and II drift scan data are given in Figures (4.2) and (4.3) respectively.

In Figure 3.4, the visibility correlation functions are plotted for the two cases using the instrumental parameters of MWA (primary beam and ϕ) for $\tau = 0$ and $w_0 = 0$. We notice the following: (a) averaging over more baselines causes the correlation function to decorrelate faster when the number of baselines are small but the function converges as the number of baselines is increased, (b) the correlation function decorrelates faster for larger baselines, as anticipated earlier in the section based on the analytic expression, Eq. (3.31), (c) a comparison between Figures 3.4 and 3.1 shows the decorrelation time

[1]Foreground components from both the point sources and diffuse galactic emission are expected to be dominated by synchrotron radiation from power-law energy distribution of relativistic electrons. The galaxy is optically thin to these photons, therefore, the observed spectrum retains the form of the emitted spectrum, which is featureless. The main mechanism of the absorption of radio photons in the interstellar medium is free-free absorption off thermal and non-thermal electrons. The optical depth of free-free absorption: $\tau = 3.3\times10^{-7}(T/10^4)^{-1.35}\nu^{-2.1}$EM, where ν is in GHz and EM, the emission measure, is observationally determined to be: $EM = 5\,\mathrm{pc\,cm^{-3}}$ (e.g. Haffner et al. [1999]); the optical depth is negligible at frequencies of interest to us.

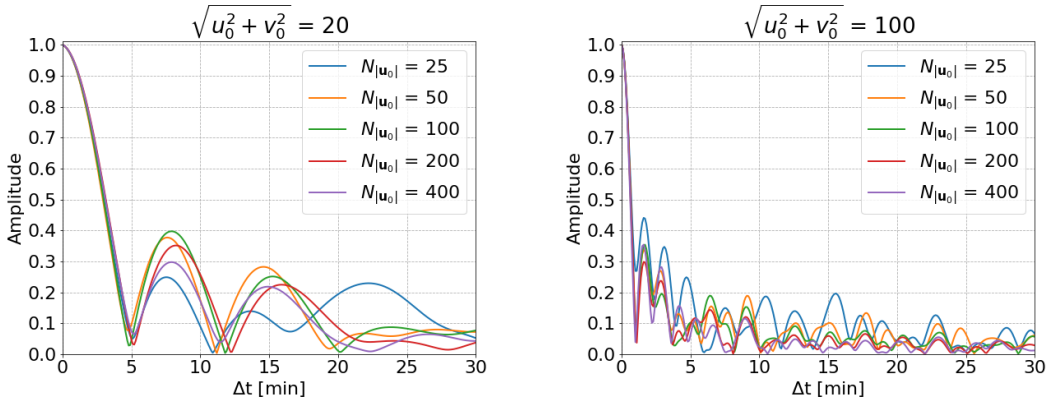

Figure 3.4: The visibility correlation function (Eq. (3.32)) is shown as a function of Δt (normalized to unity for $\Delta t = 0$) for two baselines $\sqrt{u_0^2+v_0^2} = 20, 100$ for $u_0 = v_0$, for MWA primary beam and latitude. The visibility correlation function is seen to fall to half its value in a few minutes.

scale for the HI signal is much larger than for a set of point sources. For $|\mathbf{u_0}| = 100$, the point sources decorrelate to 50% of the peak in less than a minute while this time is nearly 10 minutes for the HI signal.

The structure of the foreground wedge in a drift scan is expected to be similar to the tracking mode; we verify it using analytic estimates and simulations but do not show it here.

3.3.2 Diffuse correlated foregrounds

An important contribution to the foregrounds comes from diffuse galactic emission (DGE) which is correlated on the sky plane; this component of the foregrounds is dominated by optically-thin galactic synchrotron emission. The spatial and frequency dependence of this emission is separable if the emission is optically thin, which, as noted above, is a good assumption and is key to the separation of foregrounds from the HI signal. We consider statistically homogeneous and isotropic component of the diffuse foreground here. This case differs from the HI signal only in different frequency dependencies of the two signals. Therefore, the formulation is similar to the case of HI signal discussed above.

As we assume the DGE to be statistically homogeneous and isotropic, the two-point function of fluctuations on the plane of the sky in Fourier space could be characterized by a power spectrum C_q such that and $q = |\mathbf{q}| = \sqrt{q_1^2+q_2^2}$, where $\mathbf{q} = (q_1, q_2)$, with q_1 and q_2 being the two Fourier components on the sky plane. C_q can be expressed as:

$$\left\langle I_\nu(\mathbf{q}) I_{\nu'}(\mathbf{q}')\right\rangle = (2\pi)^2 C_q(\nu,\nu')\delta^2(\mathbf{q}-\mathbf{q}') \tag{3.33}$$

For our analysis we adopt the following form and normalization of C_q, as appropriate for $\nu \simeq 150$ (e.g. Ghosh et al. [2012] and references therein):

$$C_q(\nu,\nu') = a_0 \left(\frac{\nu}{\nu_0}\right)^{-\alpha} \left(\frac{\nu'}{\nu_0}\right)^{-\alpha} \left(\frac{q}{1000}\right)^{-\gamma} \tag{3.34}$$

where $\alpha = 0.52$ (Rogers and Bowman [2008]) is the spectral index and $\gamma = 2.34$ (Ghosh et al. [2012]) is the index of spatial power spectrum. The value of $a_0 = A_0 \left(2k_B\nu_0^2/c^2\right)^2$ is 237 Jy^2 at $\nu_0 = 154\,\mathrm{MHz}$. It rescales the amplitude factor, $A_0 = 513\mathrm{mK}^2$, given in Ghosh et al. [2012] from $(\mathrm{mK})^2$ at 150 MHz to Jy^2 at ν_0. For a single polarization this factor should be divided by 4.

Using the formalism used for analysing the HI signal it can readily be shown that the visibility correlation function in frequency space can be related to C_q as:

$$\left\langle V_\nu(\mathbf{u}_\nu, w_\nu, t) V^*_{\nu'}(\mathbf{u}'_{\nu'}, w'_{\nu'}, t') \right\rangle = \int \frac{d^2q}{(2\pi)^2} C_q(\nu,\nu') e^{iq_1 \cos\phi \Delta H} \times Q_\nu(\mathbf{q}, \mathbf{u}_\nu, w_\nu, \Delta H = 0) Q^*_{\nu'}(\mathbf{q}, \mathbf{u}'_{\nu'}, w'_{\nu'}, \Delta H) \tag{3.35}$$

where the Fourier beam of DGE is:

$$Q_\nu(\mathbf{q}, \mathbf{u}_\nu, w_\nu, \Delta H) = \int d^2\theta A_\nu(\boldsymbol{\theta}) \exp\left[-2\pi i \left(\boldsymbol{x}_u \cdot \boldsymbol{\theta} - \frac{1}{2} y\theta^2\right)\right] \tag{3.36}$$

with

$$x_u = u_\nu - \frac{1}{2\pi}(q_1 + q_2 \sin\phi \Delta H) \tag{3.37}$$

$$x_v = v_\nu - \frac{1}{2\pi}(q_2 - q_1 \sin\phi \Delta H) \tag{3.38}$$

$$y = w_\nu + \frac{1}{2\pi} q_1 \cos\phi \Delta H \tag{3.39}$$

In Eq. (3.36) we have used Q-integrals (or 2D Fourier beam) defined for the HI correlation function (Eq. (3.11)). Comparing Eq. (3.36) and Eq. (3.11) we note that the following relation between the Fourier modes of correlated diffuse foregrounds and the HI signal: $\mathbf{q} \simeq r_0 \mathbf{k}_\perp$.

As already shown for the HI signal, Eq. (3.36) can be made more tractable by assuming the primary beam to be separable and symmetric. To establish general characteristics of DGE foreground we carry out analytical calculations with a symmetric Gaussian beam: $e^{-(l^2+m^2)/\Omega_g}$, which allows us to extend the integration limits from $-\infty$ to $+\infty$. Following the HI analysis, we also expand n to the first order. This gives us:

$$Q_\nu(\mathbf{q}, \mathbf{u}_\nu, w_\nu, \Delta H) = \pi\Omega'_g \exp\left[-\pi^2 \Omega'_g \left(x_u^2 + x_v^2\right)\right] \tag{3.40}$$

where $\Omega'_g = \Omega_g/(1 - i\pi y \Omega_g)$. It should be noted that these variables can be read off directly from Q-integrals defined for the HI signal by putting $r_0 \mathbf{k}_\perp \simeq \mathbf{q}$. This shows the equivalence of the HI signal and diffuse foregrounds in the Fourier domain on the plane of the sky.

We next carry out frequency integrals to transform to delay space. As already discussed in section 3.3.1, the main results in the delay space can be obtained by retaining only the frequency dependence of baselines because the foregrounds wedge in the two-dimensional power spectrum of foregrounds arises largely due to the chromaticity of baselines (e.g. Paul et al. [2016]).

The frequency integral can be computed numerically for a finite bandpass. To carry out analytical calculations, the limits of the frequency integral can be extended to infinity. However, under this assumption, the baseline ($\mathbf{u}_\nu = \mathbf{u}_0 \nu/\nu_0$) also becomes infinity and the integral does not converge [1]. To correctly pick the relevant scales of diffuse foregrounds, we apply a Gaussian window function in frequency space ($\exp\left(-c_2(\nu-\nu_0)^2\right)$) which allows us to pick the relevant scales within the bandwidth (B) of the instrument and also enables us to extend the limits of integration. [2] This gives us:

$$\tilde{Q}(\mathbf{q}, \mathbf{u}_0, w_0, \Delta H) = \int_{\nu_0 - B/2}^{\nu_0 + B/2} d\nu e^{2\pi i \tau \nu} e^{-c_2(\nu-\nu_0)^2} Q_\nu(\mathbf{q}, \mathbf{u}_\nu, w_\nu, \Delta H)$$
$$= \pi \Omega'_g \sqrt{\frac{\pi}{c_1 + c_2}} \exp\left[-\frac{\pi^2 \tau^2}{c_1 + c_2}\right] \exp\left[2\pi i \tau \nu_0 \left(1 + \frac{c_1}{c_1 + c_2} \frac{1}{|\mathbf{q}_\mathbf{u}|} (a_1 + a_2 \sin\phi \Delta H)\right)\right]$$
$$\times \exp\left[-\frac{\Omega'_g}{4}\left(\frac{c_2}{c_1 + c_2}(a_1 + a_2 \sin\phi\Delta H)^2 + (a_2 - a_1 \sin\phi\Delta H - |\mathbf{q}_\mathbf{u}| \sin\phi \Delta H)^2\right)\right] \tag{3.41}$$

where $c_1 = (|\mathbf{q}_\mathbf{u}|/\nu_0)^2 \Omega'_g/4, c_2 = 1/(bB^2), \mathbf{q}_\mathbf{u} = 2\pi \mathbf{u}_0, a_1 = q_1 - 2\pi u_0, a_2 = q_2 - 2\pi \nu_0$. The parameter b is a numerical factor which can be tuned to get the desired width of the Gaussian window function. The argument of the factor $\exp\left[-2\pi^2\tau^2/(c_1+c_2)\right]$ in Eq. (3.41) yields the linear relation corresponding to the foreground wedge.

We can read off the correlation scales for diffuse correlation foregrounds from Eq. (3.41). A baseline $\mathbf{u}_0$ is most sensitive to the Fourier mode $\mathbf{q}_\mathbf{u}$. As in the case of the HI signal, the decorrelation time scale for a drift scan can be estimated readily by putting $\mathbf{q} = \mathbf{q}_u$

[1] This highlights the main difference between the HI signal and the two-dimensional diffuse foregrounds. In the former, the frequency integral picks the scale along the line-of-sight $k_\parallel$ while no such scale exists for diffuse foregrounds

[2] A similar window (e.g. Blackman-Nuttall window, e.g. Paul et al. [2016]) is applied to the data to prevent the leakage of foregrounds from the foreground wedge to the clean EoR window.

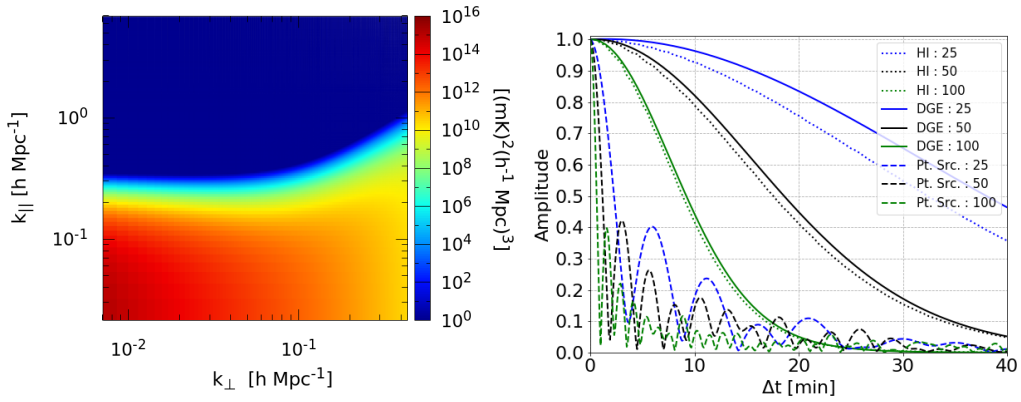

Figure 3.5: In the left panel, we show two-dimensional power spectrum of DGE ($\Delta H = 0$) in the $k_\parallel$–$k_\perp$ plane in units $(\mathrm{mK})^2(\mathrm{h}^{-1}\mathrm{Mpc})^3$. The figure assumes $\nu_0 = 154\,\mathrm{MHz}$ and bandwidth $B = 10\,\mathrm{MHz}$. The relation applicable to the HI signal is used to transform from the telescope variables (u_0, v_0, τ) to the Fourier modes ($\mathbf{k}_\perp$, $k_\parallel$), and to convert the power spectrum to the appropriate units (e.g. Paul et al. [2016]). The Figure highlights the separation of foregrounds from the EoR window; the bandwidth determines the extent of the flat region parallel to the $k_\parallel$ axis. In the right panel, the visibility correlation function (normalized to unity for $\Delta t = 0$) for DGE is shown for three baselines $\sqrt{u_0^2 + v_0^2} = 25, 50, 100$ (Eq. (3.42)). We also show the HI and point source visibility correlation functions for comparison.

and simplifying the expression. We finally obtain:

$$\left\langle V_\tau(\mathbf{u}_0, w_0, t) V_\tau^*(\mathbf{u}'_0, w'_0, t') \right\rangle = \iint_{\nu_0 - B/2}^{\nu_0 + B/2} d\nu d\nu' \left\langle V_\nu(\mathbf{u}_\nu, w_\nu, t) V_{\nu'}^*(\mathbf{u}'_{\nu'}, w'_{\nu'}, t') \right\rangle$$
$$= \int \frac{d^2q}{(2\pi)^2} C_q(\nu_0, \nu_0) e^{iq_1 \cos\phi \Delta H} \tilde{Q}(\mathbf{q}, \mathbf{u}_0, \Delta H = 0) \tilde{Q}^*(\mathbf{q}, \mathbf{u}'_0, \Delta H) \quad (3.42)$$

Eq. (3.42) gives the general expression for visibility correlation function in delay space for a drift scan observation. It can be computed by using Eqs. (3.34), (3.41) in Eq. (3.42). It reduces to the relevant expression for tracking observation for $\Delta H = 0$. In Figure 3.5 we show numerical results obtained from solving Eq. (3.42) for a Gaussian primary beam matched to the main lobe of MWA primary beam and $\phi = -26.7°$. We display the power spectrum in $k_\parallel$–$k_\perp$ plane for $\Delta H = 0$ and the correlation of diffuse correlated foregrounds as a function of time. Our main conclusions are:

1. Like the point sources, diffuse correlated foregrounds are confined to a wedge and the EoR window is clean for the detection of the HI signal.

2. The diffuse foregrounds decorrelate on time scales comparable to the HI signal. (We note that the difference between the two cases for the shortest baseline is partly because we use the exact MWA beam for the HI case while we use the Gaussian beam for diffuse foreground.) This should be contrasted with point-

source foregrounds that decorrelate on a much shorter time scale as compared to the HI signal.

3.4 Analysing drift scan data

Our study allows us to address the following question: over what time period can the time-ordered visibility data be averaged without diminishing the HI signal. We further seek optimal signal-to-noise for the detection of the HI signal. We computed two-point visibility correlation function to assess the coherence time scale of visibilities. Our results are shown in Figures 3.1–3.2 (amplitude of the correlation function as a function of Δt, baseline and primary beam) and 3.3 (the phase of the complex correlation function). Our study shows that the range of time scales over which time-ordered visibilities can be averaged without the loss of HI signal lies in the range of a few minutes to around 20 minutes.

Motivated by our theoretical analysis, we define the quantity:

$$\mathcal{C}_\tau(\mathbf{u}_0, w_0, t'-t) \equiv \exp(-i2\pi u_0 \cos\phi \Delta H)\left\langle V_\tau(\mathbf{u}_0, w_0, t) V_\tau^*(\mathbf{u}_0, w_0, t')\right\rangle \tag{3.43}$$

Notice that $\mathcal{C}_\tau(\mathbf{u}_0, w_0, t'-t) = \mathcal{C}_\tau^*(\mathbf{u}_0, w_0, t-t')$. Our analysis shows that the complex number $\mathcal{C}_\tau(\mathbf{u}_0, w_0, t'-t)$ is dominated by its real component with a phase which remains small over the coherence time scale of the amplitude (Figure 3.3 and Figure 3.2). Our aim is to extract $\mathcal{C}_\tau(\mathbf{u}_0, w_0, t'-t)$ from the data and then suitably weigh it to extract the HI signal, optimally and without the loss of HI signal[1]. We discuss two possible ways to extract the HI signal. The first is based on averaging the visibilities before computing the correlation function.

We consider visibilities measured with time resolution ΔH (ΔH is assumed to be much smaller than the coherence scale of visibilities for any baseline of interest to us, e.g. $\Delta H = 10\,\mathrm{sec}$). Let us denote the measured visibilities as, V_n, where n corresponds to the time stamp; each visibility is a function of baseline and either ν or τ. As noted above, we could use data in either frequency or delay space. For the discussion here, we consider delay space and express all quantities as functions of ν_0. For brevity, we

[1] To prevent the HI signal loss, the simplest way to extract the HI signal from drift scans would be to not use the coherence of visibilities in time. Assuming visibilities are measured with time resolution much shorter than the coherence time scale, visibilities with identical time stamps can be squared (after averaging over redundant baselines) to compute the power spectrum. This gives an unbiased estimator of the HI signal. However, in such a procedure, visibilities measured at two different times are treated as uncorrelated which results in an estimator with higher noise as compared to what is achievable using further information regarding coherence of visibilities in time. If the time resolution of visibilities is around 10 seconds and the coherence time is around 10 minutes, then the noise RMS of the visibility correlation is higher by roughly the square root of the ratio of these two times.

only retain the time dependence of measured visibilities. We define:

$$\mathcal{V} = \sum_{n=1}^{N} \exp(i2\pi u_0 \cos\phi \Delta H n) V_n \tag{3.44}$$

The total time of over which the visibilities are averaged $T = N\Delta H$ should be small enough such that the signal decorrelation is negligible (Figure 3.1). For instance, we could choose N such that the decorrelation is 0.9, which corresponds roughly to 10 minutes for MWA for $\sqrt{u_0^2 + v_0^2} \simeq 20$. It also follows that if the visibilities are averaged for a period much longer than the correlation scale of the signal, there would be serious loss of the HI signal. Even though we define $\mathcal{V}$ for a single baseline $\mathbf{u}_0$, it can also be obtained by averaging visibilities over all redundant baselines. The correlation function that extracts the HI signal $|\langle V_\tau(\mathbf{u}_0, w_0, t) V_\tau^*(\mathbf{u}_0, w_0, t)\rangle|$ then is:

$$\mathcal{C}_{\rm HI} \simeq \frac{1}{N^2} \mathcal{V}\mathcal{V}^* \tag{3.45}$$

Notice that $\mathcal{C}_{\rm HI}$ is nearly the same as the expression in Eq. (3.43) in this case. A longer stream of data of length, $K \gg N$, can be divided into time slices of $N\Delta H$. The correlation function can be estimated for each slice using this method (coherent averaging as the number of pairs is $\simeq N^2$) and then averaged further over different time slices (incoherent averaging over K/N slices). $\mathcal{C}_{\rm HI}$ is also optimal as the noise RMS is nearly the same for each pair of correlated visibilities. We note that the HI signal is mostly contained in the real part of this resulting function, as the phase angle is small for time scales over which the visibilities are averaged (Figure 3.3).

A much better method to utilize the functional form shown in Figure 3.1 is to use the estimator:

$$\mathcal{C}_{\rm HI} \simeq \frac{1}{N^2} \sum_{n'} \sum_{n} \exp(-i2\pi u_0 \cos\phi \Delta H (n' - n)) V_n V_{n'}^* g^{-1}(n' - n) \tag{3.46}$$

Here $g(n' - n)$ corresponds to the time decorrelation function shown in Figure 3.1; by construction, $g(n' - n)$ is real, $g(n - n) = 1$, and $g(n' - n) = g(n - n')$. The difference between this approach and the first method is that visibilities are correlated first and then averaged. This yields the same final expression as the first method if $g(n' - n)$ is applied for a suitable time interval such that it is close to unity. A distinct advantage of this method is that we could only retain cross-correlations such that $n' \neq n$, which allows us to avoid self-correlation or noise bias; the total number of cross-correlations are $\simeq N^2/2$ in this case. This estimator is unbiased with respect to the detection of HI signal but does not minimize noise RMS. The following estimator is both unbiased

and optimal:

$$\mathcal{C}_{\rm HI} = \frac{\sum_{n'}\sum_{n}\exp(-i2\pi u_0 \cos\phi\Delta H(n'-n))V_n V^*_{n'} g(n'-n)}{\sum_{n'}\sum_{n} g^2(n'-n)} \tag{3.47}$$

The estimator is unbiased for any choice of $g(n'-n)$. However, for using this estimator, small values of $g(n'-n)$ (e.g. $g(n'-n) < 0.3$) should be avoided to prevent averaging over very noisy visibility pairs. As in the first method, the real part of this function dominates the HI signal.

The amplitude of $\mathcal{C}_{\rm HI}$ for both the proposed estimators extracts the visibility correlation function at equal time, $\langle V_\tau(\mathbf{u}_0, w_0, t)V^*_\tau(\mathbf{u}_0, w_0, t)\rangle$, which is real. The estimation of HI power spectrum from this function has been extensively studied in the analysis of EoR tracking data (e.g. Paul et al. [2016]).

Our method has similarities with other approaches proposed to analyze the drift scan data. In Parsons et al. [2016], the fringe-rate filters have been applied on the visibility data. We apply a similar filter to reduce rapid oscillations of the phase of the correlation function. We note that the filter applied in Parsons et al. [2016] takes into all the components of earth's rotation (Eq. (A.4)). In our analysis, we identify the different roles played by these components. We show how the components responsible for the rotation and translation of the intensity pattern cause the decorrelation of the amplitude of the correlation function while the component that gives rise to the translation dominates the phase of the correlation function. In m-mode analysis (Shaw et al. [2014, 2015]) the intensity pattern is expanded using spherical harmonics and the time variation of the intensity pattern is solely owing to the the change in the azimuthal angle ϕ. This time variation can then be Fourier transformed to extract m-modes of the data. The filter we apply in Eq. (3.44) corresponds to a similar process. Eq. (3.44) can be viewed as a Fourier transform in which a single mode is extracted for a time-window of the duration given roughly by the decorrelation time of the amplitude of the correlation function. Our analysis shows that such a procedure, directly applied on measured visibilities, can extract the relevant information of the HI signal.

3.4.1 Impact on foregrounds

The measured visibilities are a linear sum of the HI signal, foregrounds, and the noise, which are uncorrelated with each other. In this study, we also compute the time scale of the decorrelation of a set of point source and statistically-homogeneous and isotropic diffuse foregrounds. Does our method allow us to mitigate foregrounds?

First, we notice that the phase factor $\exp(-i2\pi\cos\phi u_0\Delta H)$ we apply to curtail rapid oscillations of the correlation function of the HI signal has the same form for fore-

grounds (Eqs. (3.35) and (3.31)). Hence, it doesn't play a role in separating foregrounds from the HI signal.

However, the decorrelation time scale of point sources is smaller than the HI signal. In this case, the following situation is possible: two visibilities separated in time are correlated such that the HI component is fully extracted ($g(n'-n)=1$) but the point source component is uncorrelated. This means that there would be partial decorrelation of this component of foregrounds when either of the two methods discussed above are used to extract the HI signal. But this argument doesn't apply to diffuse foregrounds.

Therefore, it is possible to partly reduce the level of foregrounds in a drift scan but the primary method of separating foregrounds from the HI signal remains transforming to delay space, as in a tracking observation.

3.5 Summary

In this chapter, we address the following question: over what time scales are time-ordered visibilities coherent in a drift scan for the EoR HI signal, set of point sources, and diffuse correlated foregrounds. This is an extension of our earlier work (Paul et al. [2014a]) and has similarities with other approaches in the literature (Shaw et al. [2014], Parsons et al. [2016]). Our main theoretical tool is the complex two-point correlation function of visibilities measured at different times. We consider the primary beams of PAPER, MWA, HERA, and SKA1-Low for our analysis. Our main results can be summarized as:

- Figure 3.1 shows the amplitude of the correlation function of HI visibilities in time for four interferometers. The correlation time scales vary from a few minutes to nearly 20 minutes for the cases considered. We identify the three most important factors that cause decorrelation: (a) traversal time across a coherent feature, (b) rotation of sky intensity pattern, and (c) large field of view.

- The time variation of the phase of the HI correlation function is dominated by a filter function which is determinable in terms of measurable quantities (component of east-west baseline, latitude of the telescope, etc.). This filter function can be absorbed into an overall phase. The phase angle of the resultant function is small, which means the complex correlation function is dominated by its real part. The phase angle remains small over the coherence time scale of the amplitude of the correlation function (Figure 3.3).

- Our results are valid in both frequency and delay space and are insensitive to the input HI power spectrum. By implication they are directly applicable to the analysis of EoR drift scan data.

- The nature of foregrounds in a drift scan is different from the tracking mode owing to the time dependence of the sky intensity pattern. We consider two components of foregrounds for our analysis: set of point sources and statistically homogeneous diffuse correlated emission. The decorrelation time scales for these components are displayed in Figures 3.4 and 3.5. The point sources decorrelate faster than the HI signal. This provides a novel way to partly mitigate foregrounds using only information on the sky plane. However, the diffuse foreground decorrelation time scale is comparable to that of the HI signal and the contamination from this component cannot be removed in a drift scan on the sky plane. By implication, the delay space formalism remains the principal method for isolating foregrounds from the HI signal (Figure 3.5).

We discussed in detail how our formalism can be used to extract the HI signal from the drift scan data. We argued many different approaches might be possible for the lossless retrieval of the HI signal while optimizing the noise. In the next chapter, we apply our formalism to drift scan data from MWA.

Chapter 4

Power Spectra of the Drift Scan data from MWA using DSF [1]

4.1 Introduction

In the section 1.4.5 we have listed several existing and upcoming radio telescopes which aim to detect both the sky-averaged and the fluctuating component of the redshifted HI signal from EoR. Here, we focus on the fluctuating component of the HI signal. There are considerable difficulties in the detection of this signal. As mentioned the chapter 1, the theoretical studies suggest that the strength of the signal is of the order of 10 mK while the foregrounds are brighter than 100 K at 150 MHz. These contaminants include diffuse galactic synchrotron, extragalactic point, and bright, extended radio sources. Current experiments can reduce the thermal noise of the system to suitable levels in many hundreds of hours of integration. The foregrounds can potentially be mitigated by using the fact that the HI signal and its correlations emanate from the three-dimensional structures of mega-parsec scales at high redshifts. On the the other hand, the foreground contamination is dominated by spectrally smooth sources. This means that even if foregrounds can mimic the HI signal on the plane of the sky, the third axis, corresponding to the frequency, can be used to distinguish between the two. All ongoing experiments exploit this spectral distinction to isolate the HI signal from the foreground contamination (e.g. Parsons and Backer [2009], Parsons et al. [2012b]).

Many image and visibility-based pipelines have been developed to analyze the interferometric data. These have yielded upper limits on the HI signal (Paciga et al. [2011], Ali et al. [2015], Dillon et al. [2015], Paul et al. [2016], Beardsley et al. [2016], Choud-

[1] Based on:
Patwa, A. K., Sethi, S. 2019, The Astrophysical Journal, 887, 52
Patwa, A. K., Sethi, S., & Dwarakanath, K. S. 2021, MNRAS, 504, 2062

huri et al. [2016], Trott et al. [2016], Patil et al. [2017], Li et al. [2019], Barry et al. [2019], Kolopanis et al. [2019], Trott et al. [2020], Mertens et al. [2020]). The current best upper limits on the HI power spectrum lie in the range: $\simeq 50$–$75(\mathrm{mK})^2$ for $k \simeq 0.05$–$0.2\ h\mathrm{Mpc}^{-1}$ in the redshift range 6.5–10. Bowman et al. [2018] reported the detection of an absorption trough of strength 500 mK in the global HI signal in the redshift range $15 < z < 19$.

In this chapter, we present the results of the analysis of 7.5 hours of phase I and 55 hours of phase II EoR drift scan from MWA. The data were taken over 1 night in phase I and 10 nights in phase II with repeated scans of duration 5.5 hours over the same region of the sky. The feasibility of drift scan using MWA has been studied theoretically (Trott [2014], Paul et al. [2014a], Patwa and Sethi [2019]). We develop a pipeline for measuring the 21 cm power spectrum for drift scan observations in delay space. For this purpose, we use the Drift Scan Formalism (DSF) developed in the chapter 3 based on Patwa and Sethi [2019]. We work in delay space, which isolates foregrounds from the EoR window is therefore is the natural domain of power spectrum measurement (e.g. Datta et al. [2010], Parsons et al. [2012b]).

In the section 4.2, we describe the MWA EoR datasets and its pre-processing, e.g. flagging, time-averaging, and processing using CASA. We first characterize the noise properties of the data and study the stability of the system over the duration of the scan by comparing the data power spectrum with noise simulations. We then extract the HI power spectrum from the data in different representations of the HI signal in Fourier space. We finally study the behaviour of the foreground-dominated modes of the data in a drift scan. We summarize our results with concluding remarks in section 4.6.

As before, we use spatially-flat ΛCDM model for our work with $h = 0.67$, $\Omega_\Lambda = 0.6911, \Omega_m = 0.3089, \Omega_k = 0.0$ (Planck Collaboration et al. [2020]).

4.2 Drift Scan Data

Murchison Widefield Array (MWA) is a radio interferometer located in Western Australia at a latitude of $-26.7°$ and longitude of $116.7°$. MWA has 128 tiles (a tile would be referred to as an antenna in the paper) and each tile consists of 16 crossed dipoles placed on a square mesh of length ~ 4 m in a 4x4 arrangement. It operates in a frequency range of 80–300 MHz with the observational bandwidth of 30 MHz and frequency resolution (channel width) of 40 kHz. The visibility data is recorded at an interval of 2 minutes with the temporal resolution of 0.5 s. In each 2-minute snapshot, the duration of observation is 112 s. The phase I of MWA design has tightly packed core in the diameter of 100 m and full array extends upto 1.5 km. In the phase II design, 64 antennas are placed in a compact Hex configuration to increase the number of short

and redundant baselines primarily for EoR studies (Figure 2.5). The instantaneous baseline distributions of both configurations for a zenith scan is shown in Figure 4.2 (e.g. see Tingay et al. [2013], Wayth et al. [2018] for the detailed description of the design of MWA).

4.2.1 Metadata

In Figure 4.1 we display the region of the sky covered by the both scans. The scanned region covers a portion of the sky roughly from the position of the EoR0 $(0\text{h}, -27^\circ)$ to the EoR1 $(0\text{h}16\text{m}12\text{s}, -27^\circ)$ fields of the MWA. In the phase I, the one night scan spanned for 7 hrs 29 minutes on 2013-12-03 from 11:40 UTC to 19:09 UTC. In the phase II, each scan lasted 5 hours 24 minutes and was repeated across the same region of sky for 10 consecutive nights from 2016-Oct-03 to 2016-Oct-12. Each night scan was carried out between 14:39 UTC and 19:28 UTC. On the sixth night, the first two hours of data was missing and the scan lasted only 3 hrs 10 minutes.

The reported sky temperature in the regions covered by the scan varies between 210 K to 267 K. The observation also passes over Fornax A which is an extended radio source with a core and two radio lobes. Its angular extent spans the region, RA 3h25m to 3h20m30s and Dec $-37^\circ30'$ to $-36^\circ54'$. The total flux density of this source at 154 MHz is 750 Jy (McKinley et al. [2015]).

4.2.2 Flagging, calibration, and averaging

Cotter is a pre-processing pipeline which flags RFI, bad antennas, and channels (Offringa et al. [2015]). It also does cable correction, can average data, and produce CASA readable *Measurement Sets* (called MS tables or files). We apply COTTER on all 2 minute snapshots individually and average them to 10 s time resolution, with the frequency resolution kept intact (40 kHz). In each 2-minute data file, as noted above, the observation span is 112s. Thus, after time-averaging there are 11 data chunks in each 2-minute data file. We then apply bandpass and flux calibration with a strong and unresolved calibrator source Pictor A.[1]

The calibration solution tables also help in identifying and flagging unresponsive or irregularly behaving antennas and baselines manually. Next we flag the channels situated at the either ends of the coarse bands of MWA bandpass. [2]

[1] Based on Jacobs et al. [2013], Pictor A has (RA, Dec) = $(5\text{h}20\text{m}22\text{s}, -45.8^\circ)$, flux density $S_\nu = (381.88 \pm 5.36)$ Jy at 150MHz, and flux spectral index $\alpha = -0.76 \pm 0.01$.

[2] MWA's frequency band consists of 24 coarse bands, giving total observing bandwidth of 30.72 MHz. Each coarse band has 32 channels. MWA by design has missing frequency channels in each coarse band. In all data files, we flag 4 channels at both ends and 1 channel at center of each coarse band. That is if we number channels from 0 to 31, channel number 0, 1, 2, 3, 16, 28, 29, 30, 31 are flagged.

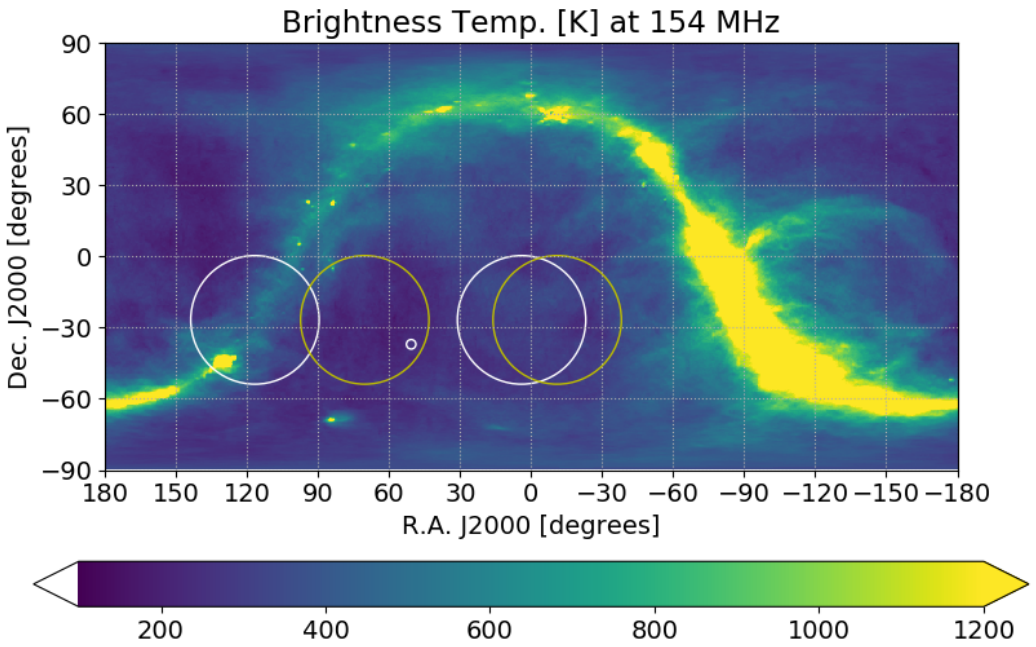

Figure 4.1: This figure displays the Haslem map scaled to 154 MHz assuming the brightness temperature spectral index $\alpha = -2.52$ (Rogers and Bowman [2008]). The big circles correspond to the main lobe of the MWA primary beam at $\nu = 154\,\mathrm{MHz}$. The scan starts roughly at the location of the big circle on the right and lasts until the big circle on the left. The sky covered in the phase I and II are shown using big white and yellow circles, respectively. The smaller white circle shows the angular position of Fornax A.

These processes yield calibrated time-ordered visibility data-sets of 10 nights (phase II) and 1 night (phase I). For the phase II, we then performed averaging over data from different nights. Since the drift scans cover the same region of the sky, we carry out LST stacking (this is the usual procedure to add data for all transit radio telescopes e.g. Bandura et al. [2014]) which constitutes aligning and averaging data snapshots with the same tracking centers, baseline bins (see below for more details), and frequency channels observed on different nights. After LST stacking, we obtain the equivalent of 5 hrs of phase II drift scan data over the same region of the sky which are suitable for the EoR power spectrum analysis.

4.3 Data analysis methodology

Many operational radio interferometers rely on drift scans to extract the power spectrum of the intensity of redshifted HI line from the EoR and low redshift data (Bandura et al. [2014], Kolopanis et al. [2019], Parsons et al. [2016], DeBoer et al. [2017]). CHIME adopt m-mode decomposition of the time-ordered visibility data, which relies upon Fourier transforming the data stream. PAPER and HERA use weighted averages of the visibility data. In Patwa and Sethi [2019] (hereafter PS19), we proposed many different approaches to analysing the drift scan data and showed similarities and differences between existing methods. In this paper, we adopt a method based on cross-correlating time-ordered visibilities (for details see PS19).

The main aim of all the analysis pipelines is to construct an unbiased and optimal estimator to extract the HI power spectrum from the visibility data in frequency or delay space. Unlike the tracking data, the intensity pattern in a drift scan changes, and the analysis of these time-dependent visibilities arising from a changing intensity pattern presents new challenges.

All the methods of extracting the HI power spectrum directly from the visibility data are based on the correlation properties of the measured visibility, $V_\nu(\mathbf{u}_\nu, w_\nu, t)$ in different domains. These properties have been well studied for the tracking data for frequency and baseline domains and can readily be extended to the drift scan data (e.g. PS19). Here our focus is the correlation of measured visibilities in the time domain. PS19 derived the decorrelation profile for the primary beams of many operational and future interferometers. Even though this behaviour is a complex function of baseline length, the de-correlation time varies between a few minutes to 10 minutes for most interferometers. As the visibility data generally has higher time resolution, e.g. we use MWA data with 10 second resolution in this paper, multiple methods can be used to analyse the data. In the analysis of PAPER data, a time filter is used to average over visibilities which contribute coherently to the HI data (e.g. Kolopanis et al. [2019]

uses 43-second time filters). As already noted above, CHIME data analysis is based on Fourier transforming time-ordered visibility data (for details see PS19).

In our work, we adopt the method based on cross-correlation of visibilities in time (PS19). This method is applicable to both frequency and delay space data. In this work, we transform visibility to delay space to isolate foregrounds. The HI power spectrum is extracted using the estimator (Eq. (45) of PS19):

$$\mathcal{C}_\tau(\mathbf{u}_0, w_0, t'-t) = \frac{\sum_{t'}\sum_t \exp(-i2\pi u_0 \cos\phi \Delta H) V_\tau(\mathbf{u}_0, w_0, t) V_\tau(\mathbf{u}_0, w_0, t')^* g(t'-t)}{\sum_{t'}\sum_t g^2(t'-t)} \tag{4.1}$$

Here $g(t-t')$ is the function that captures the de-correlation of visibilities as a function of the time difference $t-t'$ (Figure 1 of PS19). $g(t-t')$ is nearly unity for $t-t' \simeq$ 20 minutes for the shortest baselines we consider in this paper, $\sqrt{u^2+v^2} \simeq 4\lambda$ and this decorrelation time scale falls to around 5 minutes for the longest baselines, $\sqrt{u^2+v^2} \simeq$ 300. ΔH is the difference of the hour angle between times t and t'. τ is the delay space parameter and $\mathbf{u}_0 \equiv (u_0, v_0)$ and w_0 are the baselines and the w-term at the center of the band. As shown in PS19, this estimator is both unbiased and optimal for the extraction of the HI signal[1]. The measured quantity (Eq. (4.1)) is converted to the variables of the HI signal using relations given below.

4.4 Normalization

Here we describe briefly the conversion of measured quantity (Eq. (4.1)) to the variables of the HI signal. The parameters of the radio interferometer can be related to the Fourier variables of the HI signal as (e.g. Bharadwaj and Sethi [2001], Morales and Hewitt [2004], Morales and Wyithe [2010]):

$$k_{\perp 1} = \frac{2\pi}{r_0} u_0, k_{\perp 2} = \frac{2\pi}{r_0} v_0, k_\parallel = \frac{2\pi}{|\dot{r}_0|}\tau \tag{4.2}$$

Here $k_{\perp 1}$ and $k_{\perp 2}$ are the Fourier components on the sky plane while $k_\parallel$ lies along the line of sight. r_0 is the coordinate distance to the location from which the observed redshifted frequency is ν_0 and $\dot{r}_0 = dr/d\nu$ at $\nu = \nu_0$. MWA has a wide primary beam ($\sim 26^\circ$) which allows us to use the δ-function approximation for its Fourier beam in Eq. 3.19. With this assumptions, the HI power spectrum can be written in terms of the

[1] Eq. (4.1) can be understood more easily by assuming $g(t-t')$ to be unity for $t-t' \leq t_0$, where t_0 is some fixed time that depends on the baseline, and zero for $t-t' > t_0$. All the cross-correlation for $t-t' \leq t_0$ can be used for computing the HI power spectrum (or equivalently visibilities can be averaged over this time interval using a filter e.g. Kolopanis et al. [2019]). This process will yield an unbiased and optimal estimator. If the time over which the visibilities are cross-correlated is shorter than t_0, then the estimator is still unbiased but it is not optimal. If the time is chosen to be longer than t_0, then the HI signal gets uncorrelated and consequently, the estimator is neither unbiased nor optimal.

visibility correlation function using:

$$P_{\rm HI}(k) \simeq \frac{9|\dot{r}_0|r_0^2}{4\bar{I}_0^2 B\Omega_0}\left\langle V_\tau(\mathbf{u}_0, w_0=0, t)V_\tau'^*(\mathbf{u}_0, w_0=0, t)\right\rangle \tag{4.3}$$

Here $\Omega_0 = \frac{\lambda_0^2}{A_{\rm eff}}$ is the solid angle of the primary beam of MWA (the effective area of an MWA tile, $A_{\rm eff} = 21.5\,{\rm m}^2$ at $\nu = 154\,{\rm MHz}$; for details see Tingay et al. [2013]) and $k = \sqrt{k_{\perp 1}^2 + k_{\perp 2}^2 + k_\parallel^2}$. $\bar{I}$ is the mean intensity of the HI signal. For a single polarization (either XX or YY correlation), $\bar{I}_0 = k_B T_B/\lambda_0^2$, where T_B is the mean HI brightness temperature and k_B is the Boltzmann constant. For computing the mean intensity, we assume a neutral hydrogen fraction of 0.5 at $z = 8.21$ (154.24MHz), which yields $T_B = 12.6$ mK. This gives us the normalization needed to convert visibility correlation from $({\rm JyHz})^2$ to $({\rm mK})^2({\rm h}^{-1}{\rm Mpc})^3$, the units of the HI power spectrum:

$$\frac{9\lambda_0^4|\dot{r}_0|r_0^2}{4k_B^2 B\Omega_0} = 4.18\times10^{-3}\frac{({\rm mK})^2({\rm h}^{-1}{\rm Mpc})^3}{({\rm JyHz})^2} \tag{4.4}$$

The factor of 9/4 in the normalization is specific to the MWA primary beam. We use Eqs. (4.4) and (4.3) for the analysis of data.

4.5 Data Analysis

As noted above, we work in the delay space to isolate foregrounds from the EoR window. The visibilities in delay space can be derived from the visibilities in the frequency space by performing a discrete Fourier transform:

$$V_\tau(\mathbf{u}_0, w_0, t) = \Delta\sum_{\nu_0-\frac{B}{2}}^{\nu_0+\frac{B}{2}} V_\nu(\mathbf{u}_\nu, w_\nu, t)B_\nu e^{2\pi i\tau\nu} \tag{4.5}$$

For our analysis, the central frequency, $\nu_0 = 154.24\,{\rm MHz}$ and $B = 10.24\,{\rm MHz}$, which yields 256 channels of channel width $\Delta = 40\,{\rm KHz}$. B_ν corresponds to Blackman-Nuttall window (Nuttall [1981]), which helps reduce power leakage from one delay bin to another. Our analysis is entirely based on analysing visibilities and their correlations and at no stage do we transform to the image domain.

4.5.1 Gridding of *uv* field and power spectrum estimation

In Figure 4.2, we display the baseline distribution of MWA phase I and II for our observational setting (zenith scan). In a drift scan, *uv* distribution and the *w*-term are left unchanged. For zenith scans, the *w*-term is generally small, $|w_0| \leq 3\lambda_0$ in the data, and its impact on the interpretation of data can be neglected (for details e.g. see PS19).

We select a square *uv* field with u_0 and v_0 in the range $[-250\lambda_0, +250\lambda_0]$. This allows us to include all the *uv* regions in which the density of baselines is large for MWA phase-II in comparison with phase I baselines (Figure 4.2).

For analysing the data, we grid the *uv* field, with the size of a pixel determined by the expected behaviour of the HI signal. It can readily be shown that, for MWA, the HI signal de-correlates for visibilities separated by baselines that differ by more than few wavelengths (e.g. Morales and Hewitt [2004], Paul et al. [2016] and references therein). We choose a square pixel of $0.5\lambda_0$ so that the equal-time visibilities are coherent inside a grid; the baselines are assigned the same value inside a pixel. We also assume inter-pixel visibilities to be uncorrelated. Each *uv* pixel also has non-zero width $(1/\Delta)$ along the line of sight owing to finite bandwidth. For every *uv* grid, the HI signal is coherent within this width (e.g. PS19, Paul et al. [2014a], Parsons et al. [2016] and references therein) We refer to this three-dimensional grid, labelled by $\mathbf{u}_0, \tau$, a voxel in the rest of the paper.

We populate the gridded *uv* field (for a given τ) with visibility data (each data point corresponds to an integration time $t_{\rm int} = 10s$). The number of occupied grids and maximum occupancy for the data are 5427 & 55 (phase II) and 3330 & 3 (phase I), respectively (Figure 4.2).

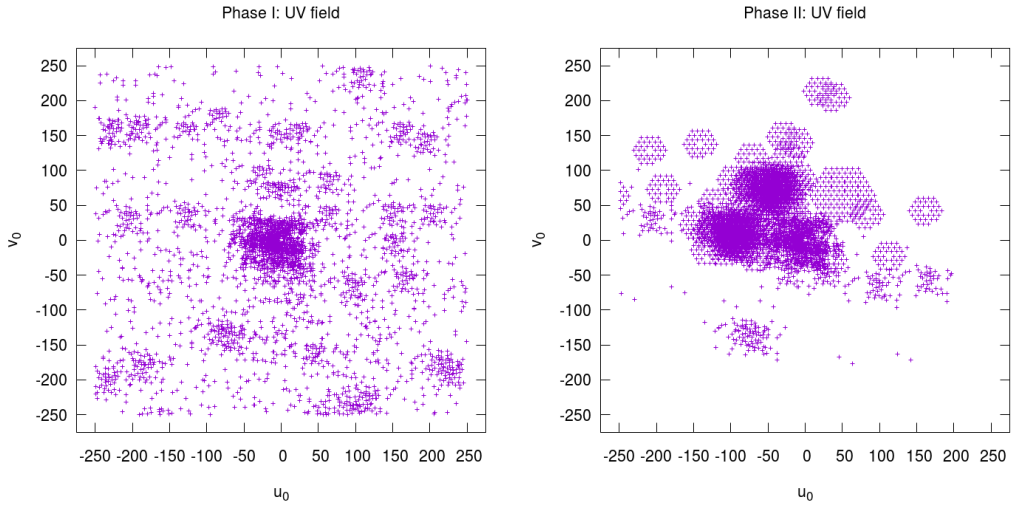

Figure 4.2: MWA phase I and II *uv* distribution for a zenith drift scan (in units of $\lambda_0 = 1.945$ m). In phase II, 64 antennas are placed in two compact hex configuration to increase the number of short and redundant baselines.

The correlation function (Eq. (4.1)) (or the power spectrum) can be computed from the gridded data. This procedure allows us to compute: (a) the mean power spectrum for one voxel, (b) a set of voxels for a given $k_\parallel$ and $|\mathbf{k}_\perp|$ or (c) a set of voxels for a fixed $|\mathbf{k}| = \sqrt{{\mathbf{k}_\perp}^2 + k_\parallel^2}$. All these quantities can be estimated as a function of inte-

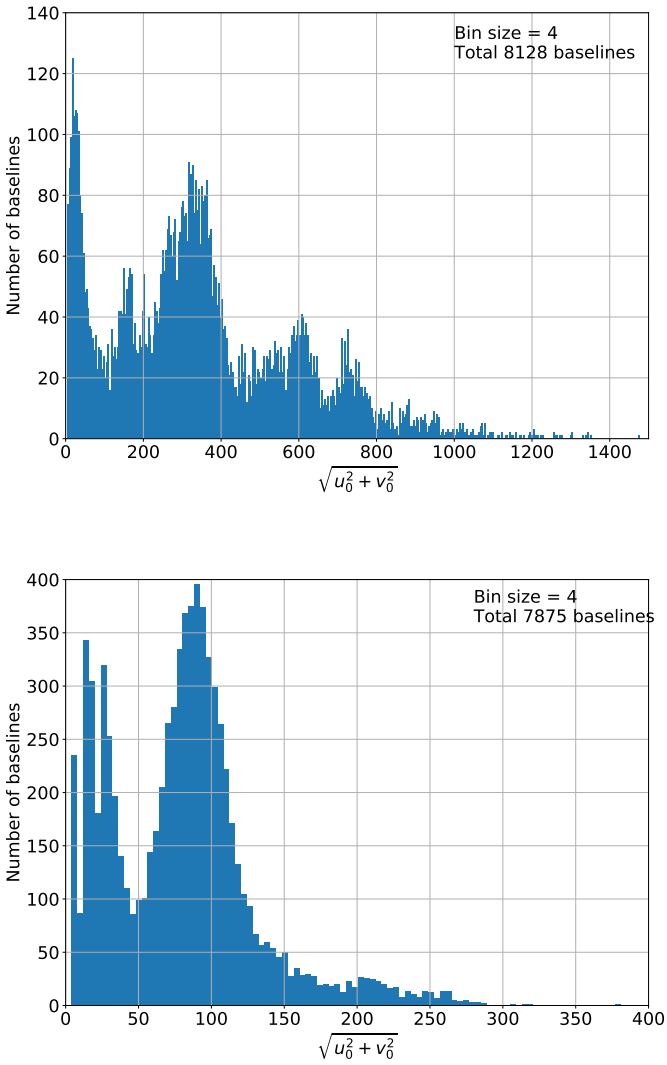

Figure 4.3: The baseline distribution of phase I (top) and II (bottom) drift scan data used in this work. MWA phase II configuration has compact hex arrangement which creates a lot of short redundant baselines suited for EoR studies.

gration (or drift) time[1]. These averages are in units of $(\mathrm{JyHz})^2$; they are converted to $(\mathrm{mK})^2(\mathrm{h}^{-1}\mathrm{Mpc})^3$ using Eq. (4.3). The estimated power spectrum is a complex number. Throughout this paper, while displaying the power spectrum, we plot the absolute value of this complex number.

[1]In this paper we use terms integration time and drift time interchangeably and plot power spectra and their RMS as a function of drift time. These concepts do not necessarily mean the same thing and therefore further clarification is needed. The occupation of a grid increases with the time of the drift scan. For a scan of duration t' all cross-correlations of time difference $\Delta t < t'$ are included in our analysis. An increase in the number of realizations (cross-correlation plus incoherent averaging over different grids) causes, for noise-dominated data, a decrease of the mean power spectrum and its RMS as a function of time which is similar to the outcome of integrating longer in a tracking observation. One case in which drift time and integration time differ is when there is missing data, e.g. on the sixth night, two hours of data is missing. In all the figures, the x-axis denotes the drift time.

4.5.2 Noise characteristics

Given that the expected HI signal can be only be detected after hundreds of hours of integration, it is imperative that the noise of the instrument is characterized precisely—this allows us to gauge the stability of the system, e.g. primary beam and bandpass, and the extent of foreground contamination. In this paper, we analyze multi-night drift scan data and expect the data (the cleanest modes in delay space) to be dominated by noise. We attempt to verify this hypothesis in this section.

There are multiple ways to compare the data with noise simulations. The most straightforward would be to compare the HI power spectrum extracted from data against simulated visibilities. We do not adopt this method for the following reason. If there are N visibility measurements in a pixel, there could be a total of $N(N-1)/2$ cross-correlations. However, the HI power spectrum is based on only a fraction of these cross-correlations as the HI signal decorrelates for $t'-t$ exceeding 20 minutes for even the shortest baselines we study here. For noise characterization, we give equal weight to all cross-correlations, which is equivalent to $g(t-t')=1$ in Eq. (4.1). This also allows us to use the pipeline developed for the extraction of HI signal with minor modifications on the data and simulated visibilities.

We perform this test on both phase I and II data-sets. For comparison with data, we simulate visibility data using Gaussian random noise. In this case, each visibility cross-correlation has zero mean (because all visibilities are uncorrelated), and an RMS σ given by (Christiansen and Hoegbom [1969]):

$$\sigma = \frac{1}{\eta_s}\frac{2k_B T_{sys}}{A_{\rm eff}\sqrt{\Delta\nu t_{\rm int}}} \tag{4.6}$$

For our simulation, we assume MWA system parameters for our the scan: $A_{\rm eff} = 21.4m^2$, $\Delta\nu = 40$ kHz, $t_{\rm int} = 10$ s. Further, we assume: $\eta_s = 1$ and $T_{\rm sys} = 400$ K which gives $\sigma = 81.8$ Jy. We note that the comparison of noise simulations with data allows us to determine $\eta_s T_{\rm sys}$[1]. We transform these simulated visibilities to delay domain for the baseline distribution of MWA Phase II. Since the cross-correlation is a

[1]Noise simulations allow us to establish the extent to which the data behaves like thermal noise. In the ideal case of equally filled grids it also allows us to get analytic estimates of the projected noise. Let us assume the total number of visibilities is N (each visibility corresponds to an integration time of 10 s) distributed in M grids, or the occupancy of each grid is $K = N/M$. Let us further assume the signal adds coherently in each grid and incoherently across grids. Neglecting self-correlation, the number of cross-correlations in each grid are $R \simeq K^2/2$, which gives the expected RMS for each grid to be $\sigma_{\rm pix} = \sigma/\sqrt{R}$. If these cross-correlations are further averaged incoherently across M grids, the final expected RMS is $\sigma_{\rm fin} = \sigma_{\rm pix}/\sqrt{M}$. We do not reach this noise level for a multitude of theoretical and experimental reasons. First, each cross-correlation inside a grid doesn't receive the same weight for the expected theoretical HI signal, as already discussed above. Second, the occupancy of each grid is determined by the baseline distribution of the interferometer (Figure 4.2) and it is not uniform. Third, we expect foreground contamination which is expected to increase the RMS above the Gaussian noise.

a $[10^{10}$ $(\mathrm{mK})^2(\mathrm{h}^{-1}\mathrm{Mpc})^3]$	XX	YY
Night 1	5.9	7.4
Night 2	5.3	6.9
Night 3	7.3	9
Night 4	5.6	7.4
Night 5	6.4	8.3
Night 6	4.2	5.4
Night 7	6.3	8
Night 8	5.8	7.3
Night 9	6.2	8.1
Night 10	5.8	7.5

Table 4.1: The table displays the normalization defined in Eq. (4.7) for the 10-night data for both XX and YY polarizations.

product of two visibilities, the RMS is proportional to σ^2, which scales as $1/\sqrt{N}$, with N being the number of total cross-correlations. In a given pixel, the number of cross-correlations increase as t^2. Therefore, the RMS of the power spectrum computed from all cross-correlation within a pixel is expected to scale as $1/t$. This motivates us to define the following function for comparing the simulated noise with the data:

$$f(t) = a\left(\frac{2}{t}\right) \tag{4.7}$$

where a and t are in units of $(\mathrm{mK})^2(\mathrm{h}^{-1}\mathrm{Mpc})^3$ and minutes, respectively. In Table (4.1) we display the results of 10 nights of data. The coefficient a in Eq. (4.7) is computed using the first half an hour data on every night. Night 6 data gives a smaller value because there is no data on that night for the first two hours and the data flow starts from a slightly cooler region of the sky. From simulated visibilities we obtain $a \simeq 11.7 \times 10^{10}$, which is higher than the data for $\eta_s T_{\mathrm{sys}} = 400\,\mathrm{K}$. A comparison with data allows us to infer $250\,\mathrm{K} < \eta_s T_{\mathrm{sys}} < 330\,\mathrm{K}$. For $\eta_s \simeq 1$, the estimated system temperature is in good agreement with the reported range of system temperatures in the scanned region of the sky.

When the data from all the nights is combined, we obtain $a = 8.4 \times 10^9$ (XX) and $a = 10.4 \times 10^9$ (YY). A comparison with the values in Table (4.1) shows that the improvement for combined 10 nights of data is nearly a factor of 7 while the decrement under the ideal conditions would be closer to a factor of 10.

Figure 4.4 shows both the simulated noise and the data as a function of drift time. The figures display the mean power spectra and the RMS of mean power spectra for Gaussian Noise (GN) simulations and the combined data sets of 10 nights. Different lines (129 lines) in the figures correspond to the values of the delay parameter τ (including $\tau = 0$). The data is also compared to the expected analytic function (Eq. (4.7)).

Figures 4.4 also show that the RMS in noise simulation and the lower envelope of the data (both XX and YY polarizations) fall as expected from Eq. (4.7). For the lower envelope of the data which correspond to the cleanest delay parameters, there is reduction of noise by nearly two orders of magnitude over nearly 5 hrs, as anticipated by the analytic fit (Eq. (4.7)). The excellent agreement between the data and the simulated noise shows that nearly 30% of the data is noise-dominated while the remaining likely suffer from some level of foreground contamination.

The second notable feature in the data is a bump in the mean power and the RMS towards the end of the scan. This increase can be understood from Figure 4.1. It is caused when the strong radio source Fornax A enters the main lobe of the primary beam and the primary beam sidelobes get contaminated by the emission from the galactic plane.

To test the hypothesis that this increase in the power towards the end of the scan is caused by extended sources such as Fornax and the galactic plane, we re-analyse data by excluding smaller baselines ($< 100\lambda_0$). We find that this procedure removes the bump. This shows that extended sources, even with complex structures, can be removed if small baselines are ignored in power spectra computation. However, since the HI signal is expected to be stronger on smaller baselines, this procedure is only used for testing and not for the final analysis of data.

In the foregoing, we performed all the visibility cross-correlations (with the same weight) inside a pixel and computed the average and the RMS of this quantity over all the pixels (5427 pixels for a given delay parameter τ). This yields the mean power spectrum and the RMS of the power spectrum of a pixel as a function of drift time. We show that this quantity has the behaviour expected of noise. We also carry out the noise test at the second level. At this level, all the pixels are divided into sets of randomly-selected 100 pixels. This yields 54 sets for a given τ. The power spectrum is computed for each set and then the mean and RMS is computed by performing weighted averaging over all the sets. For pure noise, we expect the RMS to reduce by a factor of $\sqrt{100}$. Figure 4.6 shows the RMS after this procedure. The ratio of the new to the other lower envelope is nearly a factor of 10, in consonance with the expected decrement. We do not show the mean of the signal in Figures 4.6 because the computation of the mean involves a linear process so it does not matter whether it is computed using all the grids or first computed over 100 grids and then averaged over the remaining grids.

We performed the noise tests on both observations. Both data-sets show similar noise behaviour. It allows us to use only phase II data to explain the general features in the noise characterisation. Further, the second test provides further evidence that a fraction of the data is uncorrupted by either systematic errors or foregrounds and therefore is useful for the detection of the HI signal. Another interesting feature of the figures is

gradual decrease in the power for the modes that are contaminated by foregrounds. This will be discussed in detail in the next section.

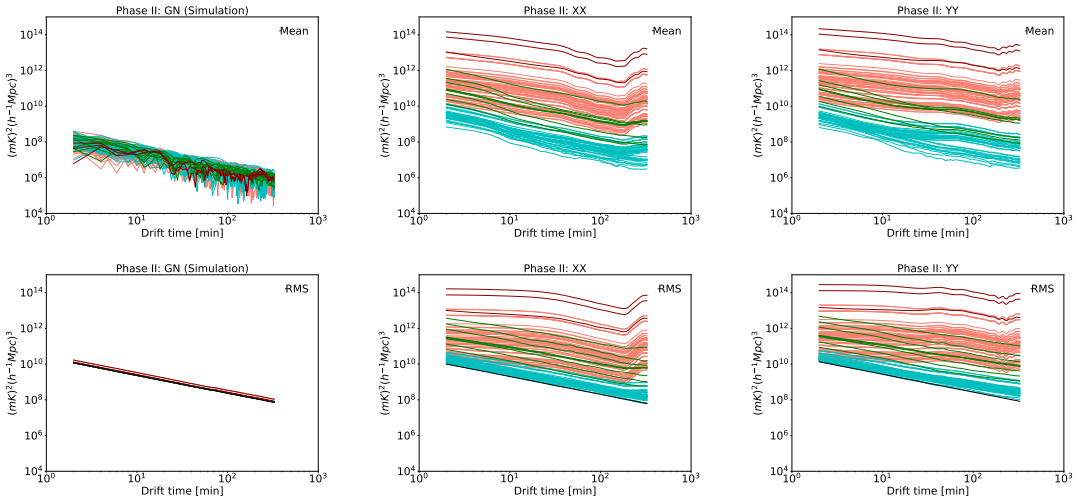

Figure 4.4: **Phase II**: The mean and RMS of power spectra of one *uv* pixel is displayed as a function of drift time. The Left column shows the outcome of Gaussian noise (GN) simulations for the baseline distribution of MWA Phase II. The second and third columns give results for XX and YY polarization, respectively. The first row shows the mean power spectrum while the second row shows the RMS of the power spectra. The horizontal axis in all the plots correspond to drift time. There are 129 curves in every panel, each corresponding to a different value of the delay space parameter τ (including $\tau = 0$). The dark and the light red coloured curves represent the wedge and horizontal bands (including two modes on either side of the band, respectively. The rest of the 'clean' modes in the EoR window are divided in two colours: intermediate values of τ in green and the cleanest modes corresponding to $\tau \geq 22$ (in units of B^{-1}) in light blue. Thick black line in the RMS plots correspond to the function $2a/t$, where t and a are in units of minutes and $(\mathrm{mK})^2(\mathrm{h}^{-1}\mathrm{Mpc})^3$, respectively.

4.5.3 The HI power spectrum

In this section again, we analyze both data-sets and present the resultant figures and values. We use only the phase II analysis to keep the narrative cleaner.
As explained above, the HI power spectrum can be estimated from the gridded visibility data using Eq. (4.1) and the relations given in section (4.4). The main input into this estimation is the function $g(t-t')$ which determines the time dependence of the coherence of the HI signal, as a function of baseline, for the primary beam of MWA (for further details see PS19). In this section we present results for the HI power spectrum and its RMS for the combined 10-night data.

In Figure 4.8, we show the mean of the HI power spectrum for a voxel as a function of the drift time. The mean HI power spectrum is computed by carrying out a weighted average over 5427 voxels for a fixed delay parameter τ.

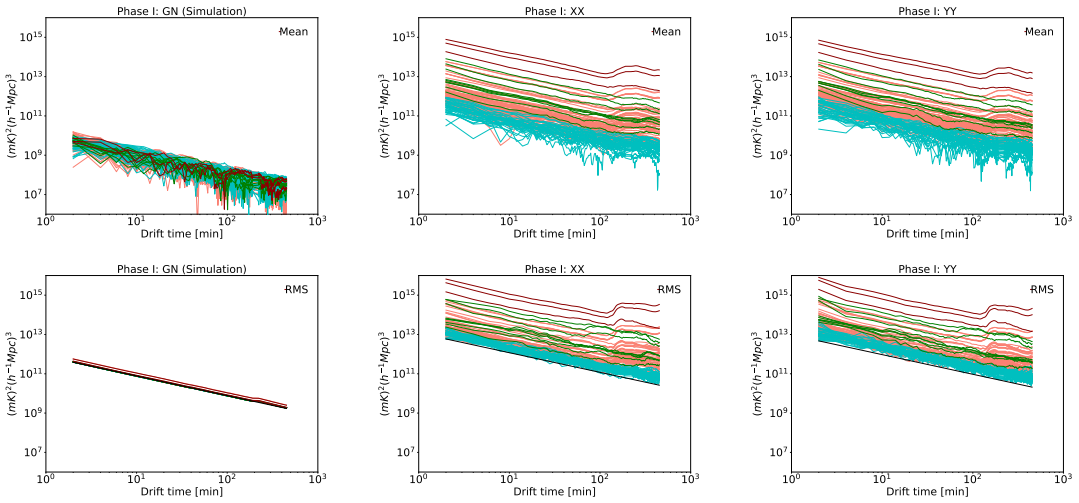

Figure 4.5: **Phase I**: It displays the counterpart of Figure 4.4 for phase I data-sets. The RMS plots in the lower row panels clearly show the $1/t$ fall (lower black envelope) as per our expectations from simulations (left panels). For phase I, on comparison with the corresponding noise simulations, we find $a = 592 \times 10^{10}$ (XX) and $a = 472 \times 10^{10}$ (YY).

Figure 4.10 shows the RMS for a voxel and for a set of 100 voxels. The RMS of the power spectrum in the latter case is computed by first defining the power spectrum as weighted average over 100 randomly chosen voxels (for a fixed τ) and then using these sets (54 sets) to compute the RMS. As noted above the mean is left unchanged by the second level of averaging as it only involves linear operations on the data. The lower envelope of the Figure 4.6 is plotted in the RMS plot for comparison.

Based on the discussion in the previous section, in which $g(t-t')$ was assumed to be unity, we can anticipate the behaviour of the the RMS of the HI power spectrum as a function of the drift time. Even for the shortest baselines we consider, the function $g(t-t')$ falls sharply after $t-t' \simeq 20\,\mathrm{min}$. Therefore, we expect the following time dependence of the RMS: for a period of time for which $g(t-t') \simeq 1$, all the visibilities inside a pixel can be considered coherent. During this period, the RMS falls as $1/t$, for the reasons discussed in the previous section. The other limiting case occurs for $t-t'$ such that $g(t-t') \simeq 0$. A pair of visibilities that satisfy this condition are incoherent. In this case, the RMS is expected to fall as $1/\sqrt{t}$. As the period of the drift scan far exceeds the coherence time scale of visibilities, the time dependence of visibilities is expected to make a transition for $1/t$ to $1/\sqrt{t}$. Figure 4.10 demonstrates this transition. Also, a comparison between the upper and the lower panels of the figures shows that the decrement in the RMS from a single voxel to 100 randomly chosen voxels is nearly a factor of 10 for the cleanest delay parameters. This result provides further proof that these delay parameters are noise dominated.

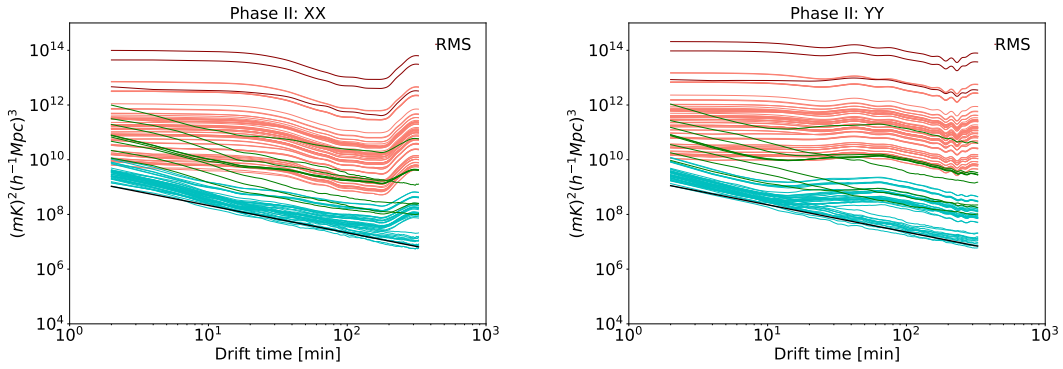

Figure 4.6: **Phase II:** These plots display the RMS of the power spectrum by re-defining the power spectrum as the average over randomly-chosen 100 grids which yields 54 data sets. The RMS is computed from these sets. The mean power spectrum is left unchanged by this procedure. The colour scheme is the same as in Figure 4.4. These plots enable us to distinguish between modes which are dominated by thermal noise from those that are not: the expected decrement in RMS for thermal noise is approximately a factor of 10, which is seen in clean modes; the wedge and the horizontal bands which are foreground dominated show a more complicated behaviour.

4.5.4 The 2-D Power Spectra and the Foreground Wedge

Figures 4.8 and 4.10 adequately capture the time-dependence of the power spectra for different delay parameters and the separation of foreground-dominated modes from noise-dominated modes. To further analyze the complex structure of the signal in the Fourier domain, we show the signal in the usual $k_\perp$–$k_\parallel$ domain in Figures 4.12 and 4.13. In these figures, cylindrical averaging for a fixed $k_\perp = \sqrt{k_{\perp 1}^2 + k_{\perp 2}^2}$ is performed.

We notice the characteristic features of delay space power spectra for MWA: foreground dominated wedge, cleaner EoR window, and the horizontal bands owing to missing MWA spectral channels. As we already noted above, to reduce power leakage between $k_\parallel$ bins we apply Blackman-Nuttall window on visibilities before taking Fourier transform along the frequency axis (Eq. (4.5)). While the application of this window reduces the leakage and therefore the EoR window is cleaner, it thickens the horizontal bands.

The two-dimensional power spectrum should be viewed alongside Figure 4.8. Figure 4.8 shows the mean power spectrum computed by averaging over all the baselines of fixed $k_\parallel$ while the two-dimensional power spectra provide additional information for a given $|\mathbf{k}_\perp|$. The time dependence in both the cases is similar: as the drift scan time is increased from 2 minutes to 120 minutes, the EoR window gets cleaner by up to two orders of magnitude owing to the reduction of noise.

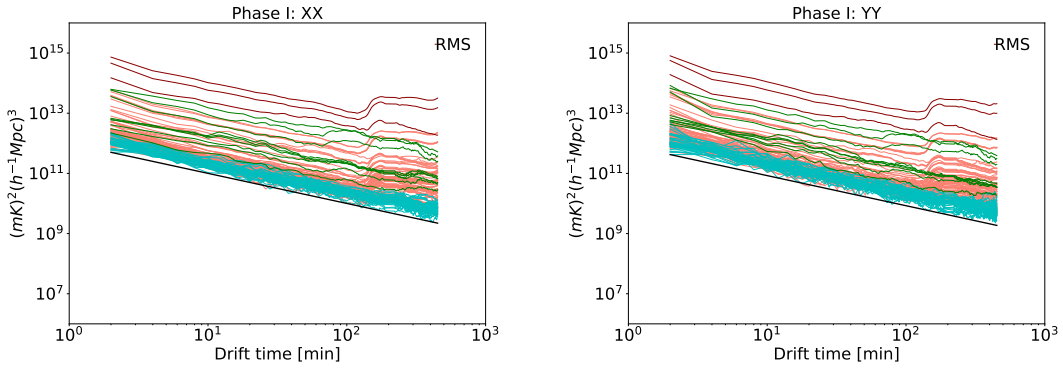

Figure 4.7: **Phase I:** This figure is the counterpart of Figure 4.6 for phase I data-sets. After the second level of averaging, it again follows the expected $1/t$ profile and we find $a = 50.2 \times 10^{10}$ (XX) and $a = 42.2 \times 10^{10}$ (YY). The ratio of old to new a values are 11.8 and 11.2.

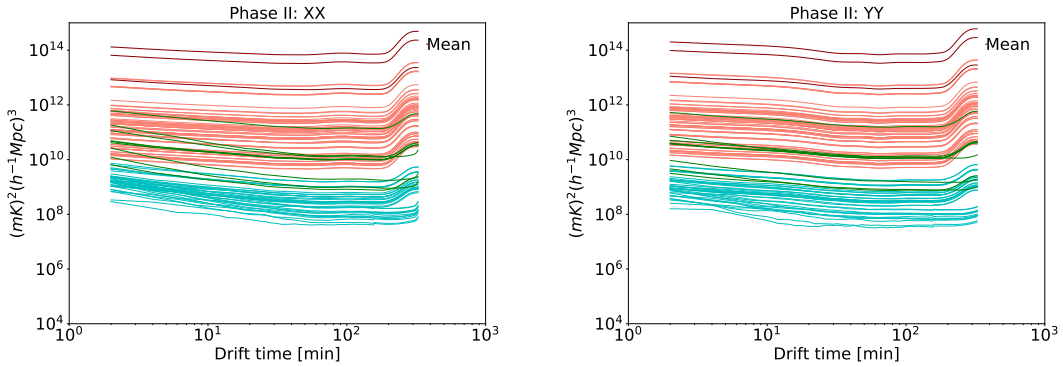

Figure 4.8: The mean of the HI power spectra for a voxel are shown for the MWA data for both XX and YY polarizations. The mean power spectra are computed using 5254 pixels for a given delay parameter τ. The colour scheme is the same as in Figure 4.4.

4.5.5 Foregrounds in the Drift Scans

The focus of this subsection are modes dominated by foregrounds. As shown in PS19, the behaviour of foregrounds in a drift scan could be markedly different from tracking observations (for another perspective on foregrounds in a drift scan see Shaw et al. [2014]). The coherence time scale of the HI signal is larger than the extragalactic point sources while it is comparable to the coherence time scale of the diffuse sources (modelled as a statistically homogeneous process in PS19). This means point sources can get uncorrelated in the process of extracting the HI signal.

We first consider Figure 4.4 which assumes $g(t-t') = 1$. In this case, all the cross-correlations within a voxel are assigned equal weight. As the time of the scan is much larger than the coherence scale of all the components, we expect partial decorrelation of point sources, the HI signal, and diffuse foregrounds. We notice a decline of power by nearly an order of magnitude in the foreground-dominated modes until late in the

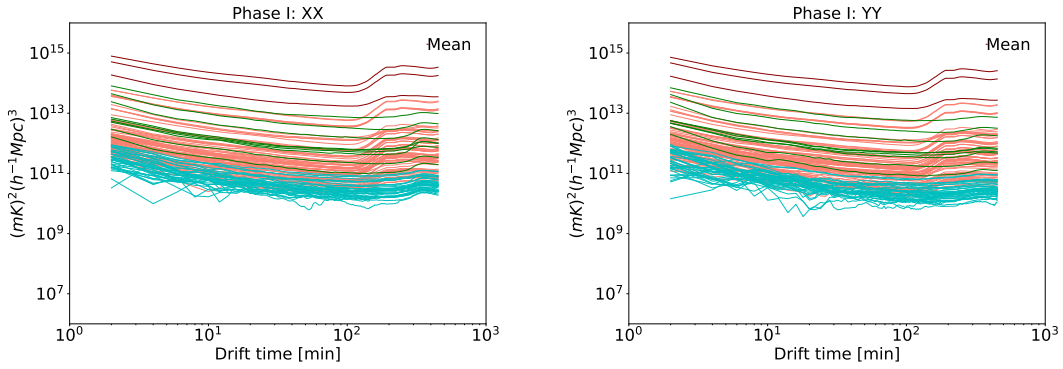

Figure 4.9: The counterpart of Figure 4.8 for MWA phase I data-sets.

scan when Fornax/galactic plane start contributing significantly. This behaviour should be compared to Figure 4.8 in which $g(t-t')$ corresponds the coherence function for HI signal for MWA. In this case, only a fraction of cross-correlations inside a voxel are carried out, which prevents the decorrelation of the HI signal. In this case, the decrement of the power in foreground dominated modes is also shallower because this process also prevents the decorrelation of diffuse foregrounds.

The complexity of the time-dependence of foregrounds in a drift scan is further revealed in Figures 4.12 and 4.13. In these figures, the power in Fourier modes in the plane of the sky is separated from the modes along the line of sight. Unlike Figure 4.8 which displays the power spectra averaged over all $|\mathbf{k}_\perp|$ for a given $k_\parallel$, Figures 4.12 and 4.13 show the results a fixed $|\mathbf{k}_\perp|$. This allows us to discern the baseline dependence of the decorrelation process in a drift scan. From Figure 1 of PS19, we note that the decorrelation time of the HI signal varies from nearly 20 minutes to 5 minutes from the shortest to the longest baselines we consider in our study, $\sqrt{u^2+v^2} \simeq 20$–300.

Figure 4.12 clearly show the depletion of power in foreground-dominated modes as the drift time increases from 2 minutes to 120 minutes. However, it is difficult to get more precise information from the figures, which underlines the complexity of the structure of foregrounds, in particular the diffuse foregrounds.

Spherically averaged 1-D Power Spectrum: The information displayed in Figures 4.8 and 4.13 can be partially summarized with one-dimensional power spectrum defined as: $\Delta^2(k) = k^3 P(k)/(2\pi^2)$ with $k = \sqrt{\mathbf{k}_\perp^2 + k_\parallel^2}$. For the EoR window, MWA baseline distribution gives $k_\parallel \gg |\mathbf{k}_\perp|$ and therefore the one-dimensional power spectrum can be computed by averaging over all $\mathbf{k}_\perp$ for a fixed $k_\parallel$ (it is partly the motivation of using the format of Figure 4.8). The one-dimensional power spectrum as a function of time can be read off from Figure 4.8 (or Figure 4.13). The best data is obtained for nearly 200 minutes of integration as clearly seen in Figure 4.13. The contamination from Fornax/galactic plane prevent any further improvement.

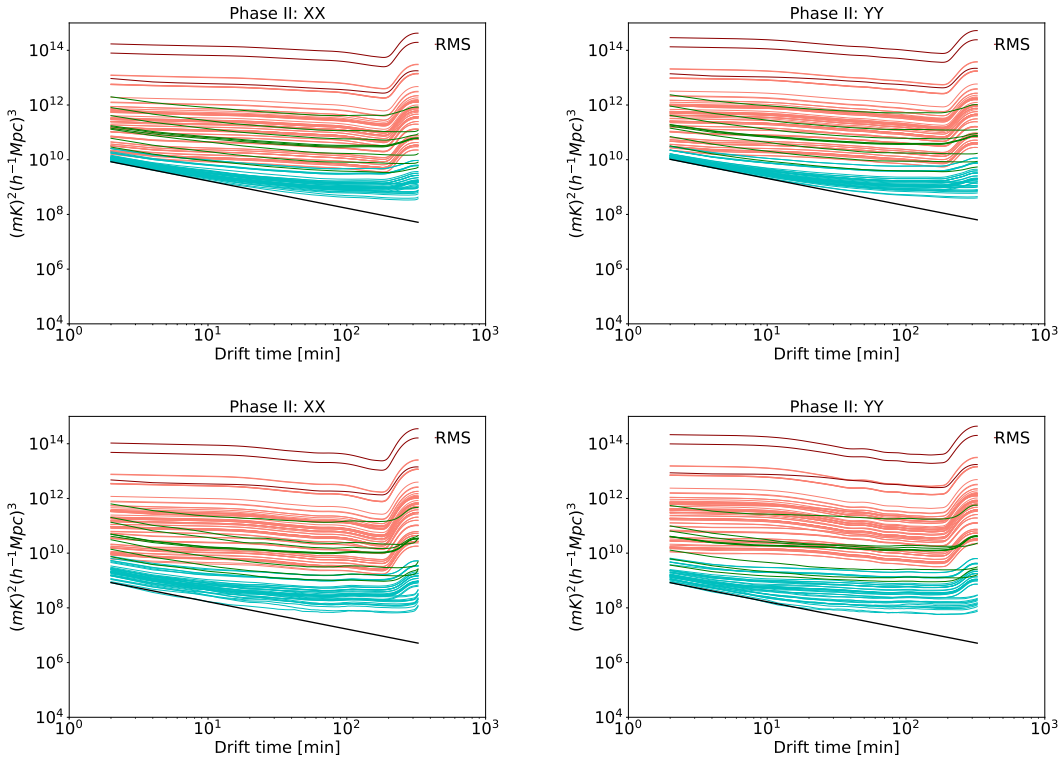

Figure 4.10: These plots are obtained from further averaging the power spectra shown in Figure 4.8 over randomly-chosen 100 grids which yields 54 sets the MWA Phase II data. The mean power spectrum is left unchanged by this procedure. The colour scheme is the same as in Figure 4.4.

Figure 4.13 shows that the largest scales in the EoR window that can be probed with MWA correspond to $k \simeq 0.2h\,\mathrm{Mpc}^{-1}$, which gives us $\Delta^2(k) \simeq (1000\ \mathrm{mK})^2$ for both XX and YY polarizations. Figure 4.13 also shows that the cleanest modes are obtained for much smaller scales. For $k \simeq 1h\,\mathrm{Mpc}^{-1}$, the one-dimensional power spectrum $\Delta^2(k) \simeq (1000\ \mathrm{mK})^2$, comparable to the value at larger scales.

The RMS of the HI power spectrum can be computed from Figure 4.10. It is based on 54 sets with each set obtained from weighted average over 100 voxels. This yields an RMS of $\simeq (1000\ \mathrm{mK})^2$ for clean modes in the range $k \simeq 0.02$–$1\ h\,\mathrm{Mpc}^{-1}$. The RMS estimate can be further improved by averaging over all the data for a fixed τ (this leaves the mean unchanged for reasons outlined in the foregoing) and then computing the RMS using bootstrapping (e.g. Kolopanis et al. [2019]).

We plot the power spectra for both the XX and YY polarizations in the same figure to emphasize the long-term system stability in a drift scan. Our calibration doesn't involve a polarized source so both the polarizations are assigned equal weight in the beginning of the scan. Our results show that no significant deviation emerges after nearly 5 hrs. As the HI signal is unpolarized, the power spectra for the two polarizations can be added in quadrature to yield a further improvement in RMS by nearly a factor

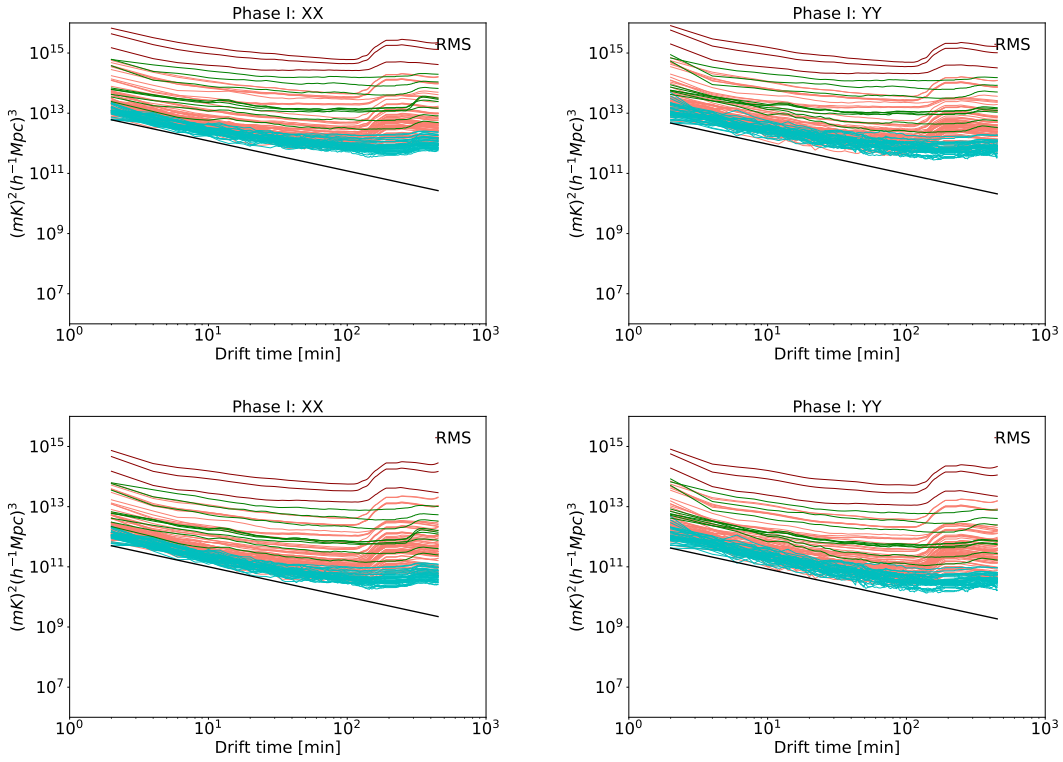

Figure 4.11: The phase I counterpart of Figure 4.10.

of $\sqrt{2}$.

4.6 Summary

The use of drift scan data to extract the HI power spectrum from high and low redshift data is an established method (e.g. Bandura et al. [2014], Kolopanis et al. [2019], Parsons et al. [2016], DeBoer et al. [2017]). Drift scans are expected to yield superior system stability which is one of the key requirements for the detection of the weak HI signal. In this paper we report the analysis of nearly 7.5 hours of phase I and 55 hours of phase II publicly-available MWA EoR drift scan data. Our analysis is based on a novel method proposed in PS19, which is an extension of formalism given by Paul et al. [2014a]. We develop a pipeline which works in two modes: (a) noise testing: the aim of this mode is to test system stability by comparing the data power spectrum against uncorrelated noise as a function of the drift time, (b) HI mode: the HI power spectrum is computed in this mode. We summarize our main results and findings:

- *Noise testing*: Figures 4.4 and 4.6 show the main results. The figures demonstrate that the data agree with the behaviour of the thermal noise for a drift scan of nearly 5 hrs—the RMS falls as $1/t$ during this period. The provides reasonable proof that the system parameters (primary beam, bandpass) are stable over the duration of the scan. This test also allows us to estimate the mean system

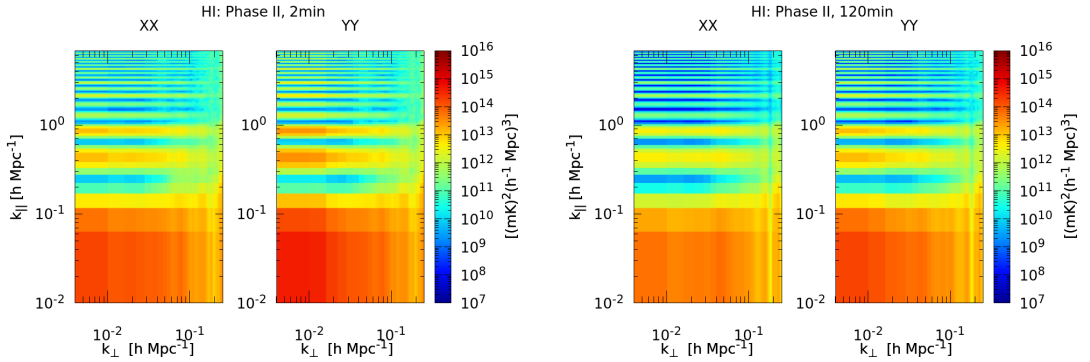

Figure 4.12: 2D Power spectra $\left[(\mathrm{mK})^2(\mathrm{h}^{-1}\mathrm{Mpc})^3\right]$ of 2- and 120-minute drift scans of MWA phase II.

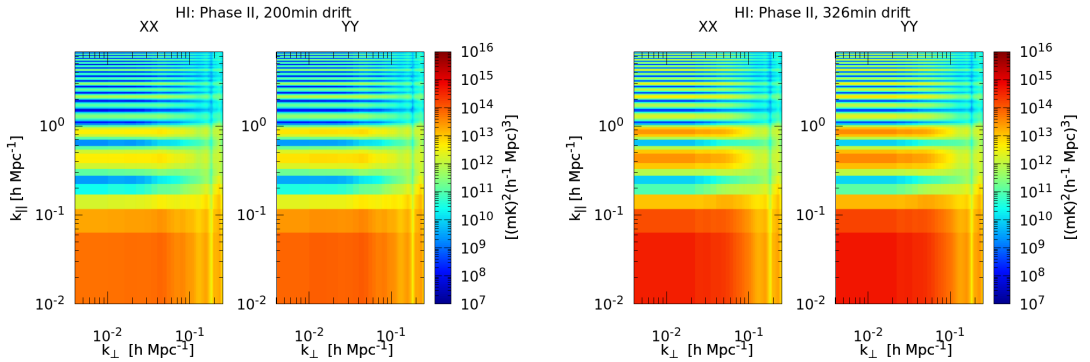

Figure 4.13: The 10-night combined data are displayed for 200 minutes and 326 minutes of drift scan.

temperature during the scan, which is in agreement with the reported values.

- *HI power spectrum*: The main results are shown in Figures 4.8 and 4.10. The two-dimensional plots (Figures 4.12 and 4.13) show the HI power spectrum in $k_\perp$–$k_\parallel$ space. These results are in line with the expectations: the RMS of the mean HI power spectrum initially falls as $1/t$ and then as $1/\sqrt{t}$ for the cleanest modes. This transition occurs when the drift time exceeds the coherence time of the HI signal.

The detection of the HI signal from the epoch of reionization remains a challenge. Given the small HI signal buried under strong foregrounds and hundreds of hours of integration time needed to reduce the thermal noise to acceptable levels, it is perhaps imperative that multiple approaches are employed to understand and analyse the signal. Drift scans exploit the stability of the system.

Acknowledgements: This scientific work makes use of the Murchison Radio-astronomy Observatory operated by CSIRO. We acknowledge the Wajarri Yamatji people as the traditional owners of the Observatory site. Support for the operation of the MWA is provided by the Australian Government (NCRIS), under a contract to Curtin Univer-

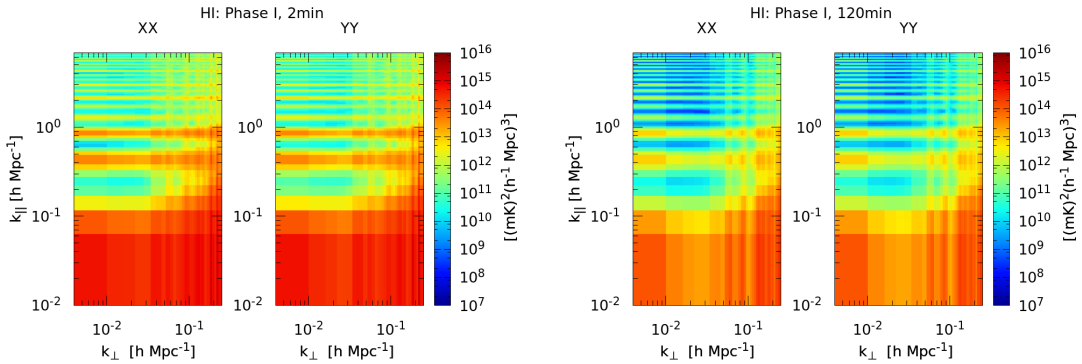

Figure 4.14: 2D Power spectra $\left[(\mathrm{mK})^2(\mathrm{h}^{-1}\mathrm{Mpc})^3\right]$ of 2- and 120-minute drift scans of MWA phase I. With the data integration the noise reduces in the EoR window. However, the modes $k_\perp > 0.1h\mathrm{Mpc}^{-1}$ appears to be contaminated.

sity administered by Astronomy Australia Limited. We also acknowledge the Pawsey Supercomputing Centre which is supported by the Western Australian and Australian Governments.

Chapter 5

Summary and Conclusions

The CD/EoR is the part of the history of the Universe when the first luminous sources formed and the electromagnetic radiation from these sources changed the state of the IGM by ionizing and heating it. The signatures of this phase transition are imprinted on the redshifted HI signal, which can give us insight into the formation and growth of large scale structures and the astrophysics of the first stars and galaxies, etc. The detection of the HI signal, both the global and the fluctuating component, remains an outstanding problem in the modern cosmology due to various challenges such as strong foreground contamination and lack of precise calibration of the instrument, etc. In this thesis we focused on the detection of the HI power spectrum using the drift scan mode of observation with existing and planned radio interferometers. We summarize the thesis and mention the main results below.

In the first chapter we reviewed the early developments of cosmology and then gave a detailed introduction to the 21 cm cosmology. In the spectra of 19 quasars in the redshift range $5.74 \lesssim z \lesssim 6.42$, Fan et al. [2006] showed the presence of Lyman-α forest which was predicted by Gunn and Peterson [1965] (section 1.3.1). It suggested that the reionization of the Universe was complete by $z \sim 6$. The Lyman-α emitters and Lyman Break galaxies are additional probe to observe the evolution of neutral hydrogen in the redshift range $6 \lesssim z \lesssim 8.5$ (section 1.3.2). In Malhotra and Rhoads [2004], the constraints on reionization redshift derived using LAEs agree with the findings of Fan et al. [2006]. Another evidence of reionization of the IGM come from the CMB observations (section 1.3.3), in which the optical depth integrated along the line-of-sight is measured and is used to estimate the mid-reionization redshift ($z_{\rm re} \simeq 7.8$ Planck Collaboration et al. [2020]). As discussed in detail in the section 1.4, the 21 cm emission of the neutral hydrogen is expected to be the richest probe of the EoR. The brightness temperature measured with respect to the microwave background radiation (CMB), the HI signal traces the evolution of the fluctuations in the baryonic matter density, heat-

ing caused by X-rays, and the Lyman-α radiation (section 1.4.1). Within the standard framework of the 21 cm cosmology, the HI signal is very faint (-200 mK to 20 mK in the redshift range $25 > z > 8$), while the foreground contamination and the system noise are of the order of 100s of Kelvins in the same frequency band (Madau et al. [1997], Tozzi et al. [2000], Morales and Wyithe [2010]). This makes the detection an extremely challenging task.

In theory, while a single antenna is sufficient to measure the full sky averaged global component of the HI signal ($\langle \Delta T_{21} \rangle(z)$), an antenna array is required to estimate the fluctuating component, e.g. the power spectrum $P_{21}(k)$, of the HI signal (section 2.3). The output of a radio interferometer array, visibility $V(\boldsymbol{u}, \nu)$, maps the 3-D Universe and captures information in the 2-D Fourier space ($\boldsymbol{k}_\perp = 2\pi \boldsymbol{u}/r$) and 1-D real space ($\nu$). In a visibility based formalism, the visibilities are taken to 3-D Fourier space by performing a Fourier transform along the frequency axis, and the amplitude-squared of these visibilities give the power spectrum of the matter distribution in the observed field (section 2.3). It is well established in the 21 cm cosmology literature that a baseline vector $\boldsymbol{u}$ in an array is primarily sensitive to a Fourier mode $\boldsymbol{k}_\perp$ in the sky (e.g. Bharadwaj and Sethi [2001], Morales and Hewitt [2004]). However, for a small primary beam, (section 3.2.1), the two closely spaced baselines ($|\boldsymbol{u}_1 - \boldsymbol{u}_2| \lesssim \mathrm{FWHM}^{-1}$) can be correlated to measure the power spectrum (Bharadwaj and Sethi [2001], Paul et al. [2014b], Patwa and Sethi [2019]).

The detection of the HI power spectrum is complicated owing to the weakness of the HI signal, the presence of the strong foreground contaminations, the thermal noise of the system, and the frequency dependent systematics (section 2.5). Each of these obstacles require dedicated treatment as discussed in this thesis and in the literature. The thermal noise is the easiest to deal with in principle as the reduction of thermal noise requires only the large integration time ($\gtrsim$ 1000 hrs). The foregrounds, galactic (resolved and diffuse) and extragalactic (unresolved and point-like), have smooth spectra with different spectral indices unlike the HI signal (section 3.3). The smoothness of the spectra put the foreground contaminations in the low $k_\parallel$ modes in Fourier domain (the foreground wedge) as shown by various simulations (e.g. Datta et al. [2010]) and the real data (e.g. MWA Beardsley et al. [2016]). The foregrounds are treated by avoidance, subtraction, or a mix of both. Further, the missing or flagged frequency channels leak the foreground contamination from the wedge to the EoR window. Such systematics can be improved with better instruments. An ideal telescope and observational setting for measuring the EoR power spectrum would have, but not limited to, the following properties—no RFI and ionospheric distortions, minimal flagging, excellent *uv* coverage from short to long baselines, identical antennas, stable and achromatic system response (beam and bandpass), coplanar array, etc.

In the chapter 3, we extended the formalism introduced in Paul et al. [2014a] to delay space. The drift scan formalism (DSF) offers advantages (smaller w-term, system stability etc.) over tracking observations to deal with the some of the challenges. In Eq. (3.19), we computed a general visibility correlation function in the delay space (τ) as a function of drift time (Δt), the antenna beam, and the latitude (ϕ) of the telescope. The amplitude and phase of the correlation function are plotted in Figures 3.1 and 3.3 for PAPER, MWA, HERA, and SKA1-Low. We found that the coherence/decorrelation time scales of the amplitude and the phase of the correlation function are affected by different system parameters: e.g. the baseline length ($|\boldsymbol{u}| = \sqrt{u^2+v^2}$) and the rotational motion of sky affect the amplitude (section 3.2.1) while the east-west component u and the traversal motion of sky influence the phase of the correlation function (section 3.2.1). We discovered and explained a turn-around feature, which demarcates the rotation and the translation dominated regimes, in the decorrelation time plots (see Figures 3.1 and 3.3). Since, our formalism is analytical, we were able to derive a compact formula for this demarcation. The decorrelation times scales of the telescopes like MWA and HERA was found to range from a few to 20 minutes depending on the baselines.
Further, in section 3.3, we applied the drift scan formalism on diffuse galactic foreground and extragalactic point-like sources with their respective power laws for spectra and derived analytical expressions for the correlation functions. The point source foregrounds get decorrelated within a few minutes regardless of the baselines but the decorrelation time scales for the diffuse sources are of the order of that of the HI signal (Figure 3.5). Based on this study, one could suggest that a part of the foreground contamination (point sources) can be mitigated in the power spectrum analysis of drift scan observations.

The drift scan formalism developed in this thesis is applied on the EoR drift scan data from MWA phase I (1 night) and phase II (10 nights). The visibility data obtained on different nights are averaged in the same LST bins to reduce the thermal noise while keeping the HI signal intact. The cross-correlation of visibilities in our work make sure that the noise bias are removed. We used the correlations calculated from DSF as weights for each visibility pairs to retain the HI signal (Eq. 4.1). The cylindrically averaged 2-D power spectra (Figures 4.13 and 4.14) clearly show the reduction of the thermal noise in the EoR window. We also performed some noise characterization tests on the data along with a realistic Gaussian noise simulations. The behaviour of noise in the noise dominated modes in EoR window match with our expectations and are consistent with the Gaussian noise simulations (Eq. 4.4). Finally, we computed the spherically averaged 1-D power spectra by avoiding the foreground dominated modes and found the lowest estimate to be $(1000\ \mathrm{mK})^2$ at $k = 0.02$–$1\ h\mathrm{Mpc}^{-1}$ and $z = 8.2$.

MWA has a good bandpass and is a stable system (see Figure 4.4). However, the main issue in the current datasets is the periodic missing frequency channels, which may be removed in the phase III of the design. So, even though we chose only the noise dominated modes to calculate the 1-D power spectra, the results have foreground residuals and systematics.

5.1 Current Upper Limits on The HI Power Spectrum

For the sake of completion, we include the latest upper limits on the HI power spectrum from EoR. Although each experiment given below has published a range of results, here we mention only the lowest estimates from the running experiments because they are primarily limited by systematics and foreground contaminations at the moment.

- **GMRT:** $\Delta^2(k) \leq (248\ \mathrm{mK})^2$ at $k = 0.5h\ \mathrm{Mpc}^{-1}, z = 8.6$ (Paciga et al. [2013])
- **PAPER:** $\Delta^2(k) \leq (200\ \mathrm{mK})^2$ at $k = 0.37h\ \mathrm{Mpc}^{-1}, z = 8.4$ (Kolopanis et al. [2019])
- **MWA:** $\Delta^2(k) \leq (43.1\ \mathrm{mK})^2$ at $k = 0.14h\ \mathrm{Mpc}^{-1}, z = 6.5$ (Trott et al. [2020])
- **LOFAR:** $\Delta^2(k) \leq (73\ \mathrm{mK})^2$ at $k = 0.075h\ \mathrm{Mpc}^{-1}, z = 9.1$ (Mertens et al. [2020])

5.2 Concluding Remarks and Future Works

The 21 cm cosmology has grown rapidly in the last two decades. However, our understanding of the Epoch of Reionization is still limited. Currently, there are multiple theoretical models of the EoR which are plausible, many of which would be ruled out with future telescopes like the SKA. The EoR community has learnt a lot from the first generation telescopes. MWA is expected to improve its shortcomings in the next phase of its design. The lessons learnt from PAPER and its power spectrum pipeline are incorporated in HERA which will put better upper limits on the HI power spectrum given its highly redundant array configuration and large number of short baselines. LOFAR has gone deeper with their newly developed technique (GPR) to mitigate the foreground residuals. These experiments and their data analysis pipelines continue to provide unique insights which are helpful to other efforts as well.

In the same direction, our work in this thesis is a contribution to the 21 cm cosmology, in which we studied the underlying time correlations in the drift scan observations. This formalism can be applied on data from other telescopes with smooth bandpass (e.g. HERA, LOFAR). It should be emphasized that the DSF is a general formalism to study the last scale matter distribution with an interferometer. Thus, even though we applied DSF to study the HI distribution in EoR, it can readily be applied to post-

EoR HI distribution for telescopes like CHIME, HIRAX, and Tianlai with a few minor changes. With statistical methods such as cross-correlations, auto-correlations, and stacking, the delay spectrum based DSF provides us another technique to probe the post-EoR Universe.

Appendix

A Coordinate Transformation

Here we discuss sky coordinate system (l,m,n) in terms of (δ,ϕ,H) with δ,ϕ,H representing the declination, the terrestrial latitude of the telescope, and the hour angle, respectively. From Eq. (A4.7) of Christiansen and Hoegbom [1969]:

$$\begin{aligned} l &= \cos\delta \sin H \\ m &= \cos\delta \cos H \sin\phi - \sin\delta\cos\phi \\ n &= \cos\delta\cos H\cos\phi + \sin\delta\sin\phi \end{aligned} \tag{A.1}$$

In a drift scan, the primary beam remains unchanged with respect to a fixed phase center chosen to be $l = m = 0$. The coordinates of intensity pattern (l,m,n) change with time, in the first order in ΔH, as:

$$\begin{aligned} \Delta l &= (m\sin\phi + n\cos\phi)\,\Delta H \\ \Delta m &= -l\sin\phi\Delta H \\ \Delta n &= -l\cos\phi\Delta H \end{aligned} \tag{A.2}$$

The change in hour angle, ΔH, can be expressed in terms of radians as:

$$\Delta H[\text{in rad}] = \frac{\pi}{12}\frac{\Delta t[\text{in min}]}{60} \tag{A.3}$$

We use Eq. (A.2) to express the time-dependent part of Eq. (3.10) explicitly in terms of change in hour angle ΔH. Eq. (A.3) can be used to express ΔH in terms of drift time Δt for a zenith scan.

$$\begin{aligned} -\frac{r_0}{2\pi}\mathbf{k}_\perp\cdot\Delta\boldsymbol{\vartheta}(\Delta t) &= -\frac{r_0}{2\pi}\left(k_{\perp 1}\Delta l + k_{\perp 2}\Delta m\right) \\ &= -\frac{r_0}{2\pi}\left(k_{\perp 1}\left(m\sin\phi + n\cos\phi\right)\Delta H - k_{\perp 2} l\sin\phi\Delta H\right) \\ &\simeq -\frac{r_0}{2\pi}\left(k_{\perp 1}\cos\phi\Delta H + \left(-lk_{\perp 2} + mk_{\perp 1}\right)\sin\phi\Delta H\right) + \frac{1}{2}\left(l^2+m^2\right)\frac{r_0}{2\pi}k_{\perp 1}\cos\phi\Delta H \end{aligned} \tag{A.4}$$

We use the flat-sky approximation $n \simeq 1 - \frac{1}{2}\left(l^2+m^2\right)$ in writing Eq. (A.4).

B Further simplification of visibility correlation function

In this appendix we discuss how the visibility correlation function can be further simplified for large primary beams and long baselines. This allows us to discern several generic properties of the correlation function. We start with the HI visibility correlation function in frequency space (Eq. (3.10)):

$$\left\langle V_\nu(\mathbf{u}_\nu, w_\nu, t) V^*_{\nu'}(\mathbf{u}'_{\nu'}, w'_{\nu'}, t') \right\rangle = \bar{I}_\nu \bar{I}_{\nu'} \int \frac{d^3k}{(2\pi)^3} P_{HI}(k) e^{ik_\parallel |\dot{r}_0| \Delta\nu} \\ e^{ir_\nu k_{\perp 1} \cos\phi \Delta H} Q_\nu(\mathbf{k}_\perp, \mathbf{u}_\nu, w_\nu, \Delta H = 0) Q^*_{\nu'}(\mathbf{k}_\perp, \mathbf{u}'_{\nu'}, w'_{\nu'}, \Delta H)$$

The Fourier beam can be expressed as (Eq. (3.11)):

$$Q_\nu(\mathbf{k}_\perp, \mathbf{u}_\nu, w_\nu, \Delta H) = \int d^2\theta A_\nu(\boldsymbol{\theta}) \exp\left[-2\pi i \left(\boldsymbol{x}_u \cdot \boldsymbol{\theta} - \frac{1}{2} y \theta^2\right)\right] \tag{B.1}$$

with

$$x_u = u_\nu - \frac{r_\nu}{2\pi} (k_{\perp 1} + k_{\perp 2} \sin\phi \Delta H) \\ x_v = v_\nu - \frac{r_\nu}{2\pi} (k_{\perp 2} - k_{\perp 1} \sin\phi \Delta H) \\ y = w_\nu + \frac{r_\nu}{2\pi} k_{\perp 1} \cos\phi \Delta H$$

We consider a Gaussian beam: $A(l,m) = e^{-(l^2+m^2)/\Omega_g}$ to compute the Fourier beam:

$$Q_\nu(\mathbf{k}_\perp, \mathbf{u}_\nu, w_\nu, \Delta H) = Q(x_u, x_v, y) = \frac{\pi\Omega_g}{1 - i\pi y \Omega_g} \exp\left[-\frac{\pi^2 \Omega_g (x_u^2 + x_v^2)}{1 - i\pi y \Omega_g}\right]$$

For $\Omega'_g \equiv \Omega_g / (1 - i\pi y \Omega_g)$

$$Q_\nu(\mathbf{k}_\perp, \mathbf{u}_\nu, w_\nu, \Delta H) = Q(x_u, x_v, y) = \pi\Omega'_g \exp\left[-\pi^2 \Omega'_g (x_u^2 + x_v^2)\right]$$

If Ω_g is large, e.g. PAPER or MWA beams, we can use δ-function approximation for solving $Q_\nu(\mathbf{k}_\perp, \mathbf{u}_\nu, w_\nu, \Delta H = 0)$, which gives us:

$$Q_\nu(\mathbf{k}_\perp, \mathbf{u}_\nu, w_\nu, \Delta H = 0) = \delta\left(u_\nu - \frac{r_\nu}{2\pi} k_{\perp 1}\right) \delta\left(v_\nu - \frac{r_\nu}{2\pi} k_{\perp 2}\right) \\ Q_\nu(\mathbf{k}_\perp, \mathbf{u}_\nu, w_\nu, \Delta H = 0) = \left(\frac{2\pi}{r_\nu}\right)^2 \delta^2\left(\mathbf{k}_\perp - \frac{2\pi}{r_\nu} \mathbf{u}_\nu\right)$$

This allows us to express HI visibility correlation function in frequency space as:

$$\left\langle V_\nu(\mathbf{u}_\nu,w_\nu,t)V^*_{\nu'}(\mathbf{u}'_{\nu'},w'_{\nu'},t')\right\rangle = \frac{\bar{I}_\nu\bar{I}_{\nu'}}{r_\nu^2}e^{2\pi i u_\nu\cos\phi\Delta H}Q^*_{\nu'}(\mathbf{k}_\perp,\mathbf{u}'_{\nu'},w'_{\nu'},\Delta H) \int\frac{dk_\parallel}{2\pi}P_{HI}(k)e^{ik_\parallel|\dot{r}_0|\Delta\nu} \tag{B.2}$$

In the previous equation we have used, $\mathbf{k}_\perp = 2\pi\mathbf{u}_\nu/r_\nu$. Eq. (B.2) gives an excellent approximation for MWA and PAPER, and for HERA and SKA1-Low for long baselines in frequency space. This can be readily be computed at any frequency and explains the features seen in Figure 3.1.

We can extend our analysis to HI visibility correlation function in delay space (Eq. (3.16)):

$$\left\langle V_\tau(\mathbf{u}_0,w_0,t)V^*_\tau(\mathbf{u}'_0,w'_0,t')\right\rangle = \iint_{\nu_0-B/2}^{\nu_0+B/2}d\nu d\nu'\left\langle V_\nu(\mathbf{u}_\nu,w_\nu,t)V^*_{\nu'}(\mathbf{u}'_{\nu'},w'_{\nu'},t')\right\rangle e^{-2\pi i\tau\Delta\nu}$$

Here B is the observational bandwidth. We make the same approximations discussed in section 3.2.1, which gives us:

$$\begin{aligned}\left\langle V_\tau(\mathbf{u}_0,w_0,t)V^*_\tau(\mathbf{u}'_0,w'_0,t')\right\rangle &= \frac{\bar{I}_0^2}{r_0^2}e^{2\pi i u_0\cos\phi\Delta H}Q^*_{\nu_0}(\mathbf{k}_\perp,\mathbf{u}'_0,w'_0,\Delta H) \\ &\quad \int\frac{dk_\parallel}{2\pi}P_{HI}(k)\iint_{\nu_0-B/2}^{\nu_0+B/2}d\nu d\nu' e^{i\Delta\nu(k_\parallel|\dot{r}_0|-2\pi\tau)} \\ \left\langle V_\tau(\mathbf{u}_0,w_0,t)V^*_\tau(\mathbf{u}'_0,w'_0,t')\right\rangle &\simeq \frac{\bar{I}_0^2}{r_0^2}e^{2\pi i u_0\cos\phi\Delta H}Q^*_{\nu_0}(\mathbf{k}_\perp,\mathbf{u}'_0,w'_0,\Delta H) \\ &\quad \int\frac{dk_\parallel}{2\pi}P_{HI}(k)\frac{2\pi B}{|\dot{r}_0|}\delta\left(k_\parallel-\frac{2\pi\tau}{|\dot{r}_0|}\right)\end{aligned}$$

In deriving this equation, we use the following result from section 3.2.1:

$$\iint_{\nu_0-B/2}^{\nu_0+B/2}d\nu d\nu' e^{i\Delta\nu(k_\parallel|\dot{r}_0|-2\pi\tau)} = B^2\,\mathrm{sinc}^2\left[\pi B\left(\tau-\frac{|\dot{r}_0|}{2\pi}k_\parallel\right)\right] \simeq \frac{2\pi B}{|\dot{r}_0|}\delta\left(k_\parallel-\frac{2\pi\tau}{|\dot{r}_0|}\right)$$

The HI signal is strongly correlated when $|\mathbf{u}_0-\mathbf{u}'_0|\lesssim 2/\Omega_g^{1/2}$, which allows us to use $\mathbf{u}'_0\approx\mathbf{u}_0$. This gives us:

$$\left\langle V_\tau(\mathbf{u}_0,w_0,t)V^*_\tau(\mathbf{u}'_0,w'_0,t')\right\rangle \simeq \frac{\bar{I}_0^2 B}{r_0^2|\dot{r}_0|}e^{2\pi i u_0\cos\phi\Delta H}Q^*_{\nu_0}(\mathbf{k}_\perp,\mathbf{u}_0,w'_0,\Delta H)P_{HI}(k) \tag{B.3}$$

where $k=\sqrt{(2\pi\tau/|\dot{r}_0|)^2+(2\pi u_0/r_0)^2+(2\pi v_0/r_0)^2}$. Though Eq. (B.3) was derived using a Gaussian beam, it is in excellent agreement with the numerical results for MWA and PAPER and for HERA and SKA1-Low for longer baselines ($|\mathbf{u}|\gtrsim 150$) shown in Figure 3.1. Eq. (B.3) also shows that the decorrelation time is expected to be nearly

independent of the delay parameter τ.

We next give explicit forms of the amplitude and the phase of the Fourier beam. We have:

$$Q_\nu(\mathbf{k}_\perp, \mathbf{u}_\nu, w_\nu, \Delta H) = Q(x_u, x_v, y) = \frac{\pi\Omega_g}{1 - i\pi y\Omega_g} \exp\left[-\frac{\pi^2\Omega_g(x_u^2 + x_v^2)}{1 - i\pi y\Omega_g}\right]$$

where $x_u^2 + x_v^2 = |\mathbf{u}_\nu|^2 \sin^2\phi\Delta H^2$ and $y = w_\nu + u_\nu \cos\phi\Delta H$. Then,

$$\begin{aligned}
Q_\nu(\mathbf{k}_\perp, \mathbf{u}_\nu, w_\nu, \Delta H) &= \pi z_1 z_2 = \pi a_1 e^{i\psi_1} a_2 e^{i\psi_2} = \pi a_1 a_2 e^{i(\psi_1+\psi_2)} \\
\text{Amp}\left[Q_\nu(\mathbf{k}_\perp, \mathbf{u}_\nu, w_\nu, \Delta H)\right] &= \pi a_1 a_2 \\
\text{Arg}\left[Q_\nu(\mathbf{k}_\perp, \mathbf{u}_\nu, w_\nu, \Delta H)\right] &= \psi_1 + \psi_2 \\
z_1 = a_1 e^{i\psi_1} &= \frac{\Omega_g}{1 - i\pi y\Omega_g} \\
z_2 = a_2 e^{i\psi_2} &= \exp\left[-\frac{\pi^2\Omega_g(x_u^2 + x_v^2)}{1 - i\pi y\Omega_g}\right]
\end{aligned}$$

On solving a_1, ψ_1, a_2, ψ_2 in terms of known quantities, we find;

$$\begin{aligned}
a_1 &= \frac{\Omega_g}{\sqrt{1 + \pi^2\Omega_g^2 y^2}} \\
\psi_1 &= \arctan(\pi\Omega_g y) \\
a_2 &= \exp\left[-\pi^2(x_u^2 + x_v^2) a_1 \cos\psi_1\right] = \exp\left[-\pi^2(x_u^2 + x_v^2)\frac{\Omega_g}{1 + \pi^2\Omega_g^2 y^2}\right] \\
\psi_2 &= -\pi^2(x_u^2 + x_v^2) a_1 \sin\psi_1 = -\pi^2(x_u^2 + x_v^2)\frac{\Omega_g}{1 + \pi^2\Omega_g^2 y^2}(\pi\Omega_g y)
\end{aligned}$$

Hence,

$$\begin{aligned}
\text{Amp}\left[Q_\nu(\mathbf{k}_\perp, \mathbf{u}_\nu, w_\nu, \Delta H)\right] &= \pi a_1 a_2 = \frac{\pi\Omega_g}{\sqrt{1 + \pi^2\Omega_g^2 y^2}} \exp\left[-\pi^2(x_u^2 + x_v^2)\frac{\Omega_g}{1 + \pi^2\Omega_g^2 y^2}\right] \\
\text{Arg}\left[Q_\nu(\mathbf{k}_\perp, \mathbf{u}_\nu, w_\nu, \Delta H)\right] &= \psi_1 + \psi_2 = \arctan(\pi\Omega_g y) - \pi^2(x_u^2 + x_v^2)\frac{\Omega_g}{1 + \pi^2\Omega_g^2 y^2}(\pi\Omega_g y)
\end{aligned} \tag{B.4}$$

The total phase acquired by the HI visibility correlation function is $2\pi u_0 \cos\phi\Delta H + \psi_1 + \psi_2$.

Bibliography

Z. S. Ali, A. R. Parsons, H. Zheng, J. C. Pober, A. Liu, J. E. Aguirre, R. F. Bradley, G. Bernardi, C. L. Carilli, C. Cheng, D. R. DeBoer, M. R. Dexter, J. Grobbelaar, J. Horrell, D. C. Jacobs, P. Klima, D. H. E. MacMahon, M. Maree, D. F. Moore, N. Razavi, I. I. Stefan, W. P. Walbrugh, and A. Walker. PAPER-64 Constraints on Reionization: The 21 cm Power Spectrum at z = 8.4. ApJ, 809:61, August 2015. doi: 10.1088/0004-637X/809/1/61. 77

B. S. Arora, J. Morgan, S. M. Ord, S. J. Tingay, N. Hurley-Walker, M. Bell, G. Bernardi, N. D. R. Bhat, F. Briggs, J. R. Callingham, A. A. Deshpand e, K. S. Dwarakanath, A. Ewall-Wice, L. Feng, B. Q. For, P. Hancock, B. J. Hazelton, L. Hindson, D. Jacobs, M. Johnston-Hollitt, A. D. Kapińska, N. Kudryavtseva, E. Lenc, B. McKinley, D. Mitchell, D. Oberoi, A. R. Offringa, B. Pindor, P. Procopio, J. Riding, L. Staveley-Smith, R. B. Wayth, C. Wu, Q. Zheng, J. D. Bowman, R. J. Cappallo, B. E. Corey, D. Emrich, R. Goeke, L. J. Greenhill, D. L. Kaplan, J. C. Kasper, E. Kratzenberg, C. J. Lonsdale, M. J. Lynch, S. R. McWhirter, M. F. Morales, E. Morgan, T. Prabu, A. E. E. Rogers, A. Roshi, N. Udaya Shankar, K. S. Srivani, R. Subrahmanyan, M. Waterson, R. L. Webster, A. R. Whitney, A. Williams, and C. L. Williams. Ionospheric Modelling using GPS to Calibrate the MWA. I: Comparison of First Order Ionospheric Effects between GPS Models and MWA Observations. PASA, 32:e029, August 2015. doi: 10.1017/pasa.2015.29. 39

Kevin Bandura, Graeme E. Addison, Mandana Amiri, J. Richard Bond, Duncan Campbell-Wilson, Liam Connor, Jean-François Cliche, Greg Davis, Meiling Deng, Nolan Denman, Matt Dobbs, Mateus Fandino, Kenneth Gibbs, Adam Gilbert, Mark Halpern, David Hanna, Adam D. Hincks, Gary Hinshaw, Carolin Höfer, Peter Klages, Tom L. Landecker, Kiyoshi Masui, Juan Mena Parra, Laura B. Newburgh, Ue-li Pen, Jeffrey B. Peterson, Andre Recnik, J. Richard Shaw, Kris Sigurdson, Mike Sitwell, Graeme Smecher, Rick Smegal, Keith Vanderlinde, and Don Wiebe. Canadian Hydrogen Intensity Mapping Experiment (CHIME) pathfinder, volume 9145 of Society of Photo-Optical Instrumentation Engineers (SPIE) Conference Series, page 914522. 2014. doi: 10.1117/12.2054950. 81, 95

R. Barkana. Possible interaction between baryons and dark-matter particles revealed by the first stars. Nature, 555:71–74, March 2018. doi: 10.1038/nature25791. 21

R. Barkana and A. Loeb. In the beginning: the first sources of light and the reionization of the universe. Phys. Rep., 349:125–238, July 2001. doi: 10.1016/S0370-1573(01)00019-9. 4

N. Barry, M. Wilensky, C. M. Trott, B. Pindor, A. P. Beardsley, B. J. Hazelton, I. S. Sullivan, M. F. Morales, J. C. Pober, J. Line, B. Greig, R. Byrne, A. Lanman, W. Li, C. H. Jordan, R. C. Joseph, B. McKinley, M. Rahimi, S. Yoshiura, J. D. Bowman, B. M. Gaensler, J. N. Hewitt, D. C. Jacobs, D. A. Mitchell, N. Udaya Shankar, S. K. Sethi, R. Subrahmanyan, S. J. Tingay, R. L. Webster, and J. S. B. Wyithe. Improving the EoR Power Spectrum Results from MWA Season 1 Observations. arXiv e-prints, art. arXiv:1909.00561, Sep 2019. 78

A. P. Beardsley, B. J. Hazelton, I. S. Sullivan, P. Carroll, N. Barry, M. Rahimi, B. Pindor, C. M. Trott, J. Line, Daniel C. Jacobs, M. F. Morales, J. C. Pober, G. Bernardi, Judd D. Bowman, M. P. Busch, F. Briggs, R. J. Cappallo, B. E. Corey, A. de Oliveira-Costa, Joshua S. Dillon, D. Emrich, A. Ewall-Wice, L. Feng, B. M. Gaensler, R. Goeke, L. J. Greenhill, J. N. Hewitt, N. Hurley-Walker, M. Johnston-Hollitt, D. L. Kaplan, J. C. Kasper, H. S. Kim, E. Kratzenberg, E. Lenc, A. Loeb, C. J. Lonsdale, M. J. Lynch, B. McKinley, S. R. McWhirter, D. A. Mitchell, E. Morgan, A. R. Neben, Nithyanandan Thyagarajan, D. Oberoi, A. R. Offringa, S. M. Ord, S. Paul, T. Prabu, P. Procopio, J. Riding, A. E. E. Rogers, A. Roshi, N. Udaya Shankar, Shiv K. Sethi, K. S. Srivani, R. Subrahmanyan, M. Tegmark, S. J. Tingay, M. Waterson, R. B. Wayth, R. L. Webster, A. R. Whitney, A. Williams, C. L. Williams, C. Wu, and J. S. B. Wyithe. First Season MWA EoR Power spectrum Results at Redshift 7. ApJ, 833(1):102, Dec 2016. doi: 10.3847/1538-4357/833/1/102. 77, 100

A. P. Beardsley, M. Johnston-Hollitt, C. M. Trott, J. C. Pober, J. Morgan, D. Oberoi, D. L. Kaplan, C. R. Lynch, G. E. Anderson, P. I. McCauley, S. Croft, C. W. James, O. I. Wong, C. D. Tremblay, R. P. Norris, I. H. Cairns, C. J. Lonsdale, P. J. Hancock, B. M. Gaensler, N. D. R. Bhat, W. Li, N. Hurley-Walker, J. R. Callingham, N. Seymour, S. Yoshiura, R. C. Joseph, K. Takahashi, M. Sokolowski, J. C. A. Miller-Jones, J. V. Chauhan, I. Bojičić, M. D. Filipović, D. Leahy, H. Su, W. W. Tian, S. J. McSweeney, B. W. Meyers, S. Kitaeff, T. Vernstrom, G. Gürkan, G. Heald, M. Xue, C. J. Riseley, S. W. Duchesne, J. D. Bowman, D. C. Jacobs, B. Crosse, D. Emrich, T. M. O. Franzen, L. Horsley, D. Kenney, M. F. Morales, D. Pallot, K. Steele, S. J. Tingay, M. Walker, R. B. Wayth, A. Williams, and C. Wu. Science with the Murchi-

son Widefield Array: Phase I results and Phase II opportunities. PASA, 36:e050, December 2019. doi: 10.1017/pasa.2019.41. 42

Robert H. Becker, Xiaohui Fan, Richard L. White, Michael A. Strauss, Vijay K. Narayanan, Robert H. Lupton, James E. Gunn, James Annis, Neta A. Bahcall, J. Brinkmann, A. J. Connolly, István Csabai, Paul C. Czarapata, Mamoru Doi, Timothy M. Heckman, G. S. Hennessy, Željko Ivezić, G. R. Knapp, Don Q. Lamb, Timothy A. McKay, Jeffrey A. Munn, Thomas Nash, Robert Nichol, Jeffrey R. Pier, Gordon T. Richards, Donald P. Schneider, Chris Stoughton, Alexand er S. Szalay, Aniruddha R. Thakar, and D. G. York. Evidence for Reionization at z~6: Detection of a Gunn-Peterson Trough in a z=6.28 Quasar. AJ, 122(6):2850–2857, December 2001. doi: 10.1086/324231. 5

C. L. Bennett, D. Larson, J. L. Weiland, N. Jarosik, G. Hinshaw, N. Odegard, K. M. Smith, R. S. Hill, B. Gold, M. Halpern, E. Komatsu, M. R. Nolta, L. Page, D. N. Spergel, E. Wollack, J. Dunkley, A. Kogut, M. Limon, S. S. Meyer, G. S. Tucker, and E. L. Wright. Nine-year Wilkinson Microwave Anisotropy Probe (WMAP) Observations: Final Maps and Results. ApJS, 208(2):20, October 2013. doi: 10.1088/0067-0049/208/2/20. 8

S. Bharadwaj and S. K. Sethi. HI Fluctuations at Large Redshifts: I–Visibility correlation. Journal of Astrophysics and Astronomy, 22:293–307, December 2001. doi: 10.1007/BF02702273. 17, 33, 35, 36, 82, 100

J. D. Bowman and A. E. E. Rogers. A lower limit of $\Delta z<0.06$ for the duration of the reionization epoch. Nature, 468:796–798, December 2010. doi: 10.1038/nature09601. 20

J. D. Bowman, I. Cairns, D. L. Kaplan, T. Murphy, D. Oberoi, and others. Science with the Murchison Widefield Array. PASA, 30:e031, April 2013. doi: 10.1017/pas.2013.009. 42

J. D. Bowman, A. E. E. Rogers, R. A. Monsalve, T. J. Mozdzen, and N. Mahesh. An absorption profile centred at 78 megahertz in the sky-averaged spectrum. Nature, 555:67–70, March 2018. doi: 10.1038/nature25792. xix, 17, 20, 21, 78

Judd D. Bowman, Alan E. E. Rogers, and Jacqueline N. Hewitt. Toward Empirical Constraints on the Global Redshifted 21 cm Brightness Temperature During the Epoch of Reionization. ApJ, 676(1):1–9, March 2008. doi: 10.1086/528675. 20

John E. Carlstrom, Gilbert P. Holder, and Erik D. Reese. Cosmology with the Sunyaev-Zel'dovich Effect. ARA&A, 40:643–680, January 2002. doi: 10.1146/annurev.astro.40.060401.093803. 10

E. Chapman, S. Zaroubi, and F. Abdalla. Foreground Removal vs. Foreground Avoidance: Contamination of the EoR Window. ArXiv/1408.4695, August 2014. 39

C. Cheng, A. R. Parsons, M. Kolopanis, D. C. Jacobs, A. Liu, S. A. Kohn, J. E. Aguirre, J. C. Pober, Z. S. Ali, G. Bernardi, R. F. Bradley, C. L. Carilli, D. R. DeBoer, M. R. Dexter, J. S. Dillon, P. Klima, D. H. E. MacMahon, D. F. Moore, C. D. Nunhokee, W. P. Walbrugh, and A. Walker. Characterizing Signal Loss in the 21 cm Reionization Power Spectrum: A Revised Study of PAPER-64. ApJ, 868:26, November 2018. doi: 10.3847/1538-4357/aae833. xii, 47, 48

Hong-Yee Chiu. Gravitational Collapse. Physics Today, 17(5):21, January 1964. doi: 10.1063/1.3051610. 5

S. Choudhuri, S. Bharadwaj, S. Chatterjee, S. S. Ali, N. Roy, and A. Ghosh. The visibility-based tapered gridded estimator (TGE) for the redshifted 21-cm power spectrum. MNRAS, 463:4093–4107, December 2016. doi: 10.1093/mnras/stw2254. 77

W. N. Christiansen and J. A. Hoegbom. Radiotelescopes. 1969. 28, 86, 105

Matthew Colless, Gavin Dalton, Steve Maddox, Will Sutherland , Peder Norberg, Shaun Cole, Joss Bland -Hawthorn, Terry Bridges, Russell Cannon, Chris Collins, Warrick Couch, Nicholas Cross, Kathryn Deeley, Roberto De Propris, Simon P. Driver, George Efstathiou, Richard S. Ellis, Carlos S. Frenk, Karl Glazebrook, Carole Jackson, Ofer Lahav, Ian Lewis, Stuart Lumsden, Darren Madgwick, John A. Peacock, Bruce A. Peterson, Ian Price, Mark Seaborne, and Keith Taylor. The 2dF Galaxy Redshift Survey: spectra and redshifts. MNRAS, 328(4):1039–1063, December 2001. doi: 10.1046/j.1365-8711.2001.04902.x. 5

T. J. Cornwell, K. Golap, and S. Bhatnagar. The Noncoplanar Baselines Effect in Radio Interferometry: The W-Projection Algorithm. IEEE Journal of Selected Topics in Signal Processing, 2:647–657, November 2008. doi: 10.1109/JSTSP.2008.2005290. 56, 58

Tim Cornwell and Ed B. Fomalont. Self-Calibration. In G. B. Taylor, C. L. Carilli, and R. A. Perley, editors, Synthesis Imaging in Radio Astronomy II, volume 180 of Astronomical Society of the Pacific Conference Series, page 187, January 1999. 41

A. Datta, J. D. Bowman, and C. L. Carilli. Bright Source Subtraction Requirements for Redshifted 21 cm Measurements. ApJ, 724:526–538, November 2010. doi: 10.1088/0004-637X/724/1/526. 48, 78, 100

Abhirup Datta, Richard Bradley, Jack O. Burns, Geraint Harker, Attila Komjathy, and T. Joseph W. Lazio. Effects Of The Ionosphere On Ground-Based Detection Of The Global 21 CM Signal From The Cosmic Dawn And The Dark Ages. arXiv e-prints, art. arXiv:1409.0513, September 2014. 39

P. de Bernardis, P. A. R. Ade, J. J. Bock, J. R. Bond, J. Borrill, A. Boscaleri, K. Coble, B. P. Crill, G. De Gasperis, P. C. Farese, P. G. Ferreira, K. Ganga, M. Giacometti, E. Hivon, V. V. Hristov, A. Iacoangeli, A. H. Jaffe, A. E. Lange, L. Martinis, S. Masi, P. V. Mason, P. D. Mauskopf, A. Melchiorri, L. Miglio, T. Montroy, C. B. Netterfield, E. Pascale, F. Piacentini, D. Pogosyan, S. Prunet, S. Rao, G. Romeo, J. E. Ruhl, F. Scaramuzzi, D. Sforna, and N. Vittorio. A flat Universe from high-resolution maps of the cosmic microwave background radiation. Nature, 404(6781):955–959, April 2000. doi: 10.1038/35010035. 2

D. R. DeBoer, A. R. Parsons, J. E. Aguirre, P. Alexander, Z. S. Ali, A. P. Beardsley, G. Bernardi, J. D. Bowman, R. F. Bradley, C. L. Carilli, C. Cheng, E. de Lera Acedo, J. S. Dillon, A. Ewall-Wice, G. Fadana, N. Fagnoni, R. Fritz, S. R. Furlanetto, B. Glendenning, B. Greig, J. Grobbelaar, B. J. Hazelton, J. N. Hewitt, J. Hickish, D. C. Jacobs, A. Julius, M. Kariseb, S. A. Kohn, T. Lekalake, A. Liu, A. Loots, D. MacMahon, L. Malan, C. Malgas, M. Maree, Z. Martinot, N. Mathison, E. Matsetela, A. Mesinger, M. F. Morales, A. R. Neben, N. Patra, S. Pieterse, J. C. Pober, N. Razavi-Ghods, J. Ringuette, J. Robnett, K. Rosie, R. Sell, C. Smith, A. Syce, M. Tegmark, N. Thyagarajan, P. K. G. Williams, and H. Zheng. Hydrogen Epoch of Reionization Array (HERA). PASP, 129(4):045001, April 2017. doi: 10.1088/1538-3873/129/974/045001. 23, 81, 95

Mark Dijkstra. Constraining Reionization with Lyα Emitting Galaxies, volume 423 of Astrophysics and Space Science Library, page 145. 2016. doi: 10.1007/978-3-319-21957-8_5. xix, 8

Mark Dijkstra, Stuart Wyithe, Zoltán Haiman, Andrei Mesinger, and Laura Pentericci. Evolution in the escape fraction of ionizing photons and the decline in strong Lyα emission from z > 6 galaxies. MNRAS, 440(4):3309–3316, June 2014. doi: 10.1093/mnras/stu531. 7

Joshua S. Dillon, Abraham R. Neben, Jacqueline N. Hewitt, Max Tegmark, N. Barry, A. P. Beardsley, J. D. Bowman, F. Briggs, P. Carroll, A. de Oliveira-Costa, A. Ewall-Wice, L. Feng, L. J. Greenhill, B. J. Hazelton, L. Hernquist, N. Hurley-Walker, D. C. Jacobs, H. S. Kim, P. Kittiwisit, E. Lenc, J. Line, A. Loeb, B. McKinley, D. A. Mitchell, M. F. Morales, A. R. Offringa, S. Paul, B. Pindor, J. C. Pober, P. Procopio, J. Riding, S. Sethi, N. Udaya Shankar, R. Subrahmanyan, I. Sullivan, Nithyanandan Thyagarajan, S. J. Tingay, C. Trott, R. B. Wayth, R. L. Webster, S. Wyithe,

G. Bernardi, R. J. Cappallo, A. A. Deshpande, M. Johnston-Hollitt, D. L. Kaplan, C. J. Lonsdale, S. R. McWhirter, E. Morgan, D. Oberoi, S. M. Ord, T. Prabu, K. S. Srivani, A. Williams, and C. L. Williams. Empirical covariance modeling for 21 cm power spectrum estimation: A method demonstration and new limits from early Murchison Widefield Array 128-tile data. Phys. Rev. D, 91(12):123011, June 2015. doi: 10.1103/PhysRevD.91.123011. 77

M. W. Eastwood, M. M. Anderson, R. M. Monroe, G. Hallinan, B. R. Barsdell, S. A. Bourke, M. A. Clark, S. W. Ellingson, J. Dowell, H. Garsden, L. J. Greenhill, J. M. Hartman, J. Kocz, T. J. W. Lazio, D. C. Price, F. K. Schinzel, G. B. Taylor, H. K. Vedantham, Y. Wang, and D. P. Woody. The Radio Sky at Meter Wavelengths: m-mode Analysis Imaging with the OVRO-LWA. AJ, 156:32, July 2018. doi: 10.3847/1538-3881/aac721. 47

A. Einstein. Cosmological considerations on the general theory of relativity, pages 175–188. 1952. 1

A. Ewall-Wice, T. C. Chang, J. Lazio, O. Doré, M. Seiffert, and R. A. Monsalve. Modeling the Radio Background from the First Black Holes at Cosmic Dawn: Implications for the 21 cm Absorption Amplitude. ApJ, 868(1):63, November 2018. doi: 10.3847/1538-4357/aae51d. 21

H. I. Ewen and E. M. Purcell. Observation of a Line in the Galactic Radio Spectrum: Radiation from Galactic Hydrogen at 1,420 Mc./sec. Nature, 168:356, September 1951. doi: 10.1038/168356a0. 12

X. Fan, M. A. Strauss, R. H. Becker, R. L. White, J. E. Gunn, G. R. Knapp, G. T. Richards, D. P. Schneider, J. Brinkmann, and M. Fukugita. Constraining the Evolution of the Ionizing Background and the Epoch of Reionization with z˜6 Quasars. II. A Sample of 19 Quasars. AJ, 132:117–136, July 2006. doi: 10.1086/504836. xix, 4, 6, 9, 99

G. B. Field. Excitation of the Hydrogen 21-CM Line. Proceedings of the IRE, 46: 240–250, January 1958. doi: 10.1109/JRPROC.1958.286741. 14, 15

G. B. Field. The Time Relaxation of a Resonance-Line Profile. ApJ, 129:551, May 1959. doi: 10.1086/146654. 14

D. J. Fixsen, E. S. Cheng, D. A. Cottingham, Jr. Eplee, R. E., R. B. Isaacman, J. C. Mather, S. S. Meyer, P. D. Noerdlinger, R. A. Shafer, R. Weiss, E. L. Wright, C. L. Bennett, N. W. Boggess, T. Kelsall, S. H. Moseley, R. F. Silverberg, G. F. Smoot, and D. T. Wilkinson. Cosmic Microwave Background Dipole Spectrum Measured by the COBE FIRAS Instrument. ApJ, 420:445, January 1994. doi: 10.1086/173575. 2

Ed B. Fomalont and Richard A. Perley. Calibration and Editing. In G. B. Taylor, C. L. Carilli, and R. A. Perley, editors, Synthesis Imaging in Radio Astronomy II, volume 180 of Astronomical Society of the Pacific Conference Series, page 79, January 1999. 41

S. Fraser, A. Hektor, G. Hütsi, K. Kannike, C. Marzo, L. Marzola, A. Racioppi, M. Raidal, C. Spethmann, V. Vaskonen, and H. Veermäe. The EDGES 21 cm anomaly and properties of dark matter. Physics Letters B, 785:159–164, October 2018. doi: 10.1016/j.physletb.2018.08.035. 21

A. Friedmann. Über die Krümmung des Raumes. Zeitschrift fur Physik, 10:377–386, January 1922. doi: 10.1007/BF01332580. 1

S. R. Furlanetto, S. P. Oh, and F. H. Briggs. Cosmology at low frequencies: The 21 cm transition and the high-redshift Universe. Phys. Rep., 433:181–301, October 2006a. doi: 10.1016/j.physrep.2006.08.002. 21

S. R. Furlanetto, S. P. Oh, and F. H. Briggs. Cosmology at low frequencies: The 21 cm transition and the high-redshift Universe. Phys. Rep., 433:181–301, October 2006b. doi: 10.1016/j.physrep.2006.08.002. 4, 5, 53, 62

B. K. Gehlot, L. V. E. Koopmans, A. G. de Bruyn, S. Zaroubi, M. A. Brentjens, K. M. B. Asad, M. Hatef, V. Jelić, M. Mevius, A. R. Offringa, V. N. Pandey, and S. Yatawatta. Wide-field LOFAR-LBA power-spectra analyses: impact of calibration, polarization leakage, and ionosphere. MNRAS, 478(2):1484–1501, August 2018. doi: 10.1093/mnras/sty1095. 40

E. M. George, C. L. Reichardt, K. A. Aird, B. A. Benson, L. E. Bleem, J. E. Carlstrom, C. L. Chang, H. M. Cho, T. M. Crawford, A. T. Crites, T. de Haan, M. A. Dobbs, J. Dudley, N. W. Halverson, N. L. Harrington, G. P. Holder, W. L. Holzapfel, Z. Hou, J. D. Hrubes, R. Keisler, L. Knox, A. T. Lee, E. M. Leitch, M. Lueker, D. Luong-Van, J. J. McMahon, J. Mehl, S. S. Meyer, M. Millea, L. M. Mocanu, J. J. Mohr, T. E. Montroy, S. Padin, T. Plagge, C. Pryke, J. E. Ruhl, K. K. Schaffer, L. Shaw, E. Shirokoff, H. G. Spieler, Z. Staniszewski, A. A. Stark, K. T. Story, A. van Engelen, K. Vanderlinde, J. D. Vieira, R. Williamson, and O. Zahn. A Measurement of Secondary Cosmic Microwave Background Anisotropies from the 2500 Square-degree SPT-SZ Survey. ApJ, 799(2):177, February 2015. doi: 10.1088/0004-637X/799/2/177. 10

A. Ghosh, J. Prasad, S. Bharadwaj, S. S. Ali, and J. N. Chengalur. Characterizing foreground for redshifted 21 cm radiation: 150 MHz Giant Metrewave Radio Telescope observations. MNRAS, 426:3295–3314, November 2012. doi: 10.1111/j.1365-2966.2012.21889.x. 38, 68

David J. Griffiths. Introduction to Quantum Mechanics. Pearson international edition. Pearson Prentice Hall, 2 edition, 2005. ISBN 9780131118928. 11

T. L. Grobler, G. Bernardi, J. S. Kenyon, A. R. Parsons, and O. M. Smirnov. Redundant interferometric calibration as a complex optimization problem. MNRAS, 476(2): 2410–2420, May 2018. doi: 10.1093/mnras/sty357. 41

J. E. Gunn and B. A. Peterson. On the Density of Neutral Hydrogen in Intergalactic Space. ApJ, 142:1633–1641, November 1965. doi: 10.1086/148444. 5, 99

James E. Gunn, Walter A. Siegmund, Edward J. Mannery, Russell E. Owen, Charles L. Hull, R. French Leger, Larry N. Carey, Gillian R. Knapp, Donald G. York, William N. Boroski, Stephen M. Kent, Robert H. Lupton, Constance M. Rockosi, Michael L. Evans, Patrick Waddell, John E. Anderson, James Annis, John C. Barentine, Larry M. Bartoszek, Steven Bastian, Stephen B. Bracker, Howard J. Brewington, Charles I. Briegel, Jon Brinkmann, Yorke J. Brown, Michael A. Carr, Paul C. Czarapata, Craig C. Drennan, Thomas Dombeck, Glenn R. Federwitz, Bruce A. Gillespie, Carlos Gonzales, Sten U. Hansen, Michael Harvanek, Jeffrey Hayes, Wendell Jordan, Ellyne Kinney, Mark Klaene, S. J. Kleinman, Richard G. Kron, Jurek Kresinski, Glenn Lee, Siriluk Limmongkol, Carl W. Lindenmeyer, Daniel C. Long, Craig L. Loomis, Peregrine M. McGehee, Paul M. Mantsch, Jr. Neilsen, Eric H., Richard M. Neswold, Peter R. Newman, Atsuko Nitta, Jr. Peoples, John, Jeffrey R. Pier, Peter S. Prieto, Angela Prosapio, Claudio Rivetta, Donald P. Schneider, Stephanie Snedden, and Shu-i. Wang. The 2.5 m Telescope of the Sloan Digital Sky Survey. AJ, 131(4):2332–2359, April 2006. doi: 10.1086/500975. 5

L. M. Haffner, R. J. Reynolds, and S. L. Tufte. WHAM Observations of Hα, [S II], and [N II] toward the Orion and Perseus Arms: Probing the Physical Conditions of the Warm Ionized Medium. ApJ, 523:223–233, September 1999. doi: 10.1086/307734. 66

B. J. Hazelton, M. F. Morales, and I. S. Sullivan. The Fundamental Multi-baseline Mode-mixing Foreground in 21 cm Epoch of Reionization Observations. ApJ, 770: 156, June 2013. doi: 10.1088/0004-637X/770/2/156. 36

Richard Hills, Girish Kulkarni, P. Daniel Meerburg, and Ewald Puchwein. Concerns about modelling of the EDGES data. Nature, 564(7736):E32–E34, December 2018. doi: 10.1038/s41586-018-0796-5. 21

G. Hinshaw, D. Larson, E. Komatsu, D. N. Spergel, C. L. Bennett, J. Dunkley, M. R. Nolta, M. Halpern, R. S. Hill, N. Odegard, L. Page, K. M. Smith, J. L. Weiland, B. Gold, N. Jarosik, A. Kogut, M. Limon, S. S. Meyer, G. S. Tucker, E. Wollack,

and E. L. Wright. Nine-year Wilkinson Microwave Anisotropy Probe (WMAP) Observations: Cosmological Parameter Results. ApJS, 208:19, October 2013. doi: 10.1088/0067-0049/208/2/19. 2

J. A. Högbom. Aperture Synthesis with a Non-Regular Distribution of Interferometer Baselines. A&AS, 15:417, June 1974. 31

A. M. Hopkins, J. Afonso, B. Chan, L. E. Cram, A. Georgakakis, and B. Mobasher. The Phoenix Deep Survey: The 1.4 GHz Microjansky Catalog. AJ, 125:465–477, February 2003. doi: 10.1086/345974. 66

W. Hu and M. White. A CMB polarization primer. New A, 2:323–344, October 1997. doi: 10.1016/S1384-1076(97)00022-5. 8

Edwin Hubble. A Relation between Distance and Radial Velocity among Extra-Galactic Nebulae. Proceedings of the National Academy of Science, 15(3):168–173, March 1929. doi: 10.1073/pnas.15.3.168. 1

D. C. Jacobs, A. R. Parsons, J. E. Aguirre, Z. Ali, J. Bowman, R. F. Bradley, C. L. Carilli, D. R. DeBoer, M. R. Dexter, N. E. Gugliucci, P. Klima, D. H. E. MacMahon, J. R. Manley, D. F. Moore, J. C. Pober, I. I. Stefan, and W. P. Walbrugh. A Flux Scale for Southern Hemisphere 21 cm Epoch of Reionization Experiments. ApJ, 776:108, October 2013. doi: 10.1088/0004-637X/776/2/108. 79

Karl G. Jansky. Radio Waves from Outside the Solar System. Nature, 132(3323):66, July 1933. doi: 10.1038/132066a0. 27

C. H. Jordan, S. Murray, C. M. Trott, R. B. Wayth, D. A. Mitchell, M. Rahimi, B. Pindor, P. Procopio, and J. Morgan. Characterization of the ionosphere above the Murchison Radio Observatory using the Murchison Widefield Array. MNRAS, 471 (4):3974–3987, November 2017. doi: 10.1093/mnras/stx1797. 40

Akanksha Kapahtia, Pravabati Chingangbam, Stephen Appleby, and Changbom Park. A novel probe of ionized bubble shape and size statistics of the epoch of reionization using the contour Minkowski Tensor. J. Cosmology Astropart. Phys., 2018(10):011, October 2018. doi: 10.1088/1475-7516/2018/10/011. 22

Shahideh Kiehbadroudinezhad, Nor Kamariah Noordin, A. Sali, and Zamri Zainal Abidin. Optimization of an Antenna Array Using Genetic Algorithms. AJ, 147 (6):147, June 2014. doi: 10.1088/0004-6256/147/6/147. xx, 32

Matthew Kolopanis, Daniel C. Jacobs, Carina Cheng, Aaron R. Parsons, Saul A. Kohn, Jonathan C. Pober, James E. Aguirre, Zaki S. Ali, Gianni Bernardi, Richard F.

Bradley, Christopher L. Carilli, David R. DeBoer, Matthew Dexter, Joshua S. Dillon, Joshua Kerrigan, Patricia Klima, Adrian Liu, Dave MacMahon, David F. Moore, Nithyanandan Thyagarajan, Chuneeta Devi Nunhokee, William Walbrughp, and Andre Walker. A simplified, lossless re-analysis of PAPER-64. arXiv e-prints, art. arXiv:1909.02085, Sep 2019. 78, 81, 82, 94, 95, 102

L. Koopmans, J. Pritchard, G. Mellema, J. Aguirre, K. Ahn, R. Barkana, I. van Bemmel, G. Bernardi, A. Bonaldi, F. Briggs, A. G. de Bruyn, T. C. Chang, E. Chapman, X. Chen, B. Ciardi, P. Dayal, A. Ferrara, A. Fialkov, F. Fiore, K. Ichiki, I. T. Illiev, S. Inoue, V. Jelic, M. Jones, J. Lazio, U. Maio, S. Majumdar, K. J. Mack, A. Mesinger, M. F. Morales, A. Parsons, U. L. Pen, M. Santos, R. Schneider, B. Semelin, R. S. de Souza, R. Subrahmanyan, T. Takeuchi, H. Vedantham, J. Wagg, R. Webster, S. Wyithe, K. K. Datta, and C. Trott. The Cosmic Dawn and Epoch of Reionisation with SKA. Advancing Astrophysics with the Square Kilometre Array (AASKA14), art. 1, April 2015a. 23

L. Koopmans, J. Pritchard, G. Mellema, J. Aguirre, K. Ahn, R. Barkana, I. van Bemmel, G. Bernardi, A. Bonaldi, F. Briggs, A. G. de Bruyn, T. C. Chang, E. Chapman, X. Chen, B. Ciardi, P. Dayal, A. Ferrara, A. Fialkov, F. Fiore, K. Ichiki, I. T. Illiev, S. Inoue, V. Jelic, M. Jones, J. Lazio, U. Maio, S. Majumdar, K. J. Mack, A. Mesinger, M. F. Morales, A. Parsons, U. L. Pen, M. Santos, R. Schneider, B. Semelin, R. S. de Souza, R. Subrahmanyan, T. Takeuchi, H. Vedantham, J. Wagg, R. Webster, S. Wyithe, K. K. Datta, and C. Trott. The Cosmic Dawn and Epoch of Reionisation with SKA. In Advancing Astrophysics with the Square Kilometre Array (AASKA14), page 1, April 2015b. 41

Adam E. Lanman and Jonathan C. Pober. Fundamental uncertainty levels of 21 cm power spectra from a delay analysis. MNRAS, 487(4):5840–5853, Aug 2019. doi: 10.1093/mnras/stz1639. 47

G. Lemaître. Un Univers homogène de masse constante et de rayon croissant rendant compte de la vitesse radiale des nébuleuses extra-galactiques. Annales de la Société Scientifique de Bruxelles, 47:49–59, January 1927. 1

W. Li, J. C. Pober, B. J. Hazelton, N. Barry, M. F. Morales, I. Sullivan, A. R. Parsons, Z. S. Ali, J. S. Dillon, A. P. Beardsley, J. D. Bowman, F. Briggs, R. Byrne, P. Carroll, B. Crosse, D. Emrich, A. Ewall-Wice, L. Feng, T. M. O. Franzen, J. N. Hewitt, L. Horsley, D. C. Jacobs, M. Johnston-Hollitt, C. Jordan, R. C. Joseph, D. L. Kaplan, D. Kenney, H. Kim, P. Kittiwisit, A. Lanman, J. Line, B. McKinley, D. A. Mitchell, S. Murray, A. Neben, A. R. Offringa, D. Pallot, S. Paul, B. Pindor, P. Procopio, M. Rahimi, J. Riding, S. K. Sethi, N. Udaya Shankar, K. Steele, R. Subrahmanian, M. Tegmark, N. Thyagarajan, S. J. Tingay, C. Trott, M. Walker, R. B.

Wayth, R. L. Webster, A. Williams, C. Wu, and S. Wyithe. Comparing Redundant and Sky-model-based Interferometric Calibration: A First Look with Phase II of the MWA. ApJ, 863(2):170, August 2018. doi: 10.3847/1538-4357/aad3c3. 41

W. Li, J. C. Pober, N. Barry, B. J. Hazelton, M. F. Morales, C. M. Trott, A. Lanman, M. Wilensky, I. Sullivan, A. P. Beardsley, T. Booler, J. D. Bowman, R. Byrne, B. Crosse, D. Emrich, T. M. O. Franzen, K. Hasegawa, L. Horsley, M. Johnston-Hollitt, D. C. Jacobs, C. H. Jordan, R. C. Joseph, T. Kaneuji, D. L. Kaplan, D. Kenney, K. Kubota, J. Line, C. Lynch, B. McKinley, D. A. Mitchell, S. Murray, D. Pallot, B. Pindor, M. Rahimi, J. Riding, G. Sleap, K. Steele, K. Takahashi, S. J. Tingay, M. Walker, R. B. Wayth, R. L. Webster, A. Williams, C. Wu, J. S. B. Wyithe, S. Yoshiura, and Q. Zheng. First Season MWA Phase II Epoch of Reionization Power Spectrum Results at Redshift 7. ApJ, 887(2):141, December 2019. doi: 10.3847/1538-4357/ab55e4. 78

Adrian Liu, Max Tegmark, Scott Morrison, Andrew Lutomirski, and Matias Zaldarriaga. Precision calibration of radio interferometers using redundant baselines. MNRAS, 408(2):1029–1050, October 2010. doi: 10.1111/j.1365-2966.2010.17174.x. 41

Adrian Liu, Aaron R. Parsons, and Cathryn M. Trott. Epoch of reionization window. I. Mathematical formalism. Phys. Rev. D, 90(2):023018, July 2014a. doi: 10.1103/PhysRevD.90.023018. 36

Adrian Liu, Aaron R. Parsons, and Cathryn M. Trott. Epoch of reionization window. II. Statistical methods for foreground wedge reduction. Phys. Rev. D, 90(2):023019, July 2014b. doi: 10.1103/PhysRevD.90.023019. 39

S. T. Loi, I. H. Cairns, T. Murphy, P. J. Erickson, M. E. Bell, A. Rowlinson, B. S. Arora, J. Morgan, R. D. Ekers, N. Hurley-Walker, and D. L. Kaplan. Density duct formation in the wake of a travelling ionospheric disturbance: Murchison Widefield Array observations. Journal of Geophysical Research (Space Physics), 121:1569–1586, February 2016. doi: 10.1002/2015JA022052. 39

Shyeh Tjing Loi, Cathryn M. Trott, Tara Murphy, Iver H. Cairns, Martin Bell, Natasha Hurley-Walker, John Morgan, Emil Lenc, A. R. Offringa, L. Feng, P. J. Hancock, D. L. Kaplan, N. Kudryavtseva, G. Bernardi, J. D. Bowman, F. Briggs, R. J. Cappallo, B. E. Corey, A. A. Deshpande, D. Emrich, B. M. Gaensler, R. Goeke, L. J. Greenhill, B. J. Hazelton, M. Johnston-Hollitt, J. C. Kasper, E. Kratzenberg, C. J. Lonsdale, M. J. Lynch, S. R. McWhirter, D. A. Mitchell, M. F. Morales, E. Morgan, D. Oberoi, S. M. Ord, T. Prabu, A. E. E. Rogers, A. Roshi, N. Udaya Shankar,

K. S. Srivani, R. Subrahmanyan, S. J. Tingay, M. Waterson, R. B. Wayth, R. L. Webster, A. R. Whitney, A. Williams, and C. L. Williams. Power spectrum analysis of ionospheric fluctuations with the Murchison Widefield Array. Radio Science, 50(7): 574–597, July 2015. doi: 10.1002/2015RS005711. 39

P. Madau, A. Meiksin, and M. J. Rees. 21 Centimeter Tomography of the Intergalactic Medium at High Redshift. ApJ, 475:429–444, February 1997. doi: 10.1086/303549. 100

S. Malhotra and J. E. Rhoads. Luminosity Functions of Lyα Emitters at Redshifts z=6.5 and z=5.7: Evidence against Reionization at z$\leq$6.5. ApJ, 617:L5–L8, December 2004. doi: 10.1086/427182. 7, 9, 99

Sangeeta Malhotra and James E. Rhoads. Large Equivalent Width Lyα line Emission at z=4.5: Young Galaxies in a Young Universe? ApJ, 565(2):L71–L74, February 2002. doi: 10.1086/338980. 7

J. C. Mather, E. S. Cheng, R. E. Eplee, Jr., R. B. Isaacman, S. S. Meyer, R. A. Shafer, R. Weiss, E. L. Wright, C. L. Bennett, N. W. Boggess, E. Dwek, S. Gulkis, M. G. Hauser, M. Janssen, T. Kelsall, P. M. Lubin, S. H. Moseley, Jr., T. L. Murdock, R. F. Silverberg, G. F. Smoot, and D. T. Wilkinson. A preliminary measurement of the cosmic microwave background spectrum by the Cosmic Background Explorer (COBE) satellite. ApJ, 354:L37–L40, May 1990. doi: 10.1086/185717. 2

B. McKinley, R. Yang, M. López-Caniego, F. Briggs, N. Hurley-Walker, R. B. Wayth, A. R. Offringa, R. Crocker, G. Bernardi, P. Procopio, B. M. Gaensler, S. J. Tingay, M. Johnston-Hollitt, M. McDonald, M. Bell, N. D. R. Bhat, J. D. Bowman, R. J. Cappallo, B. E. Corey, A. A. Deshpande, D. Emrich, A. Ewall-Wice, L. Feng, R. Goeke, L. J. Greenhill, B. J. Hazelton, J. N. Hewitt, L. Hindson, D. Jacobs, D. L. Kaplan, J. C. Kasper, E. Kratzenberg, N. Kudryavtseva, E. Lenc, C. J. Lonsdale, M. J. Lynch, S. R. McWhirter, D. A. Mitchell, M. F. Morales, E. Morgan, D. Oberoi, S. M. Ord, B. Pindor, T. Prabu, J. Riding, A. E. E. Rogers, D. A. Roshi, N. Udaya Shankar, K. S. Srivani, R. Subrahmanyan, M. Waterson, R. L. Webster, A. R. Whitney, A. Williams, and C. L. Williams. Modelling of the spectral energy distribution of Fornax A: leptonic and hadronic production of high-energy emission from the radio lobes. MNRAS, 446:3478–3491, February 2015. doi: 10.1093/mnras/stu2310. 79

M. McQuinn, A. Lidz, O. Zahn, S. Dutta, L. Hernquist, and M. Zaldarriaga. The morphology of HII regions during reionization. MNRAS, 377:1043–1063, May 2007. doi: 10.1111/j.1365-2966.2007.11489.x. 22

Matthew McQuinn, Steven R. Furlanetto, Lars Hernquist, Oliver Zahn, and Matias Zaldarriaga. The Kinetic Sunyaev-Zel'dovich Effect from Reionization. ApJ, 630 (2):643–656, September 2005. doi: 10.1086/432049. 10

F. G. Mertens, M. Mevius, L. V. E. Koopmans, A. R. Offringa, G. Mellema, S. Zaroubi, M. A. Brentjens, H. Gan, B. K. Gehlot, V. N. Pand ey, A. M. Sardarabadi, H. K. Vedantham, S. Yatawatta, K. M. B. Asad, B. Ciardi, E. Chapman, S. Gazagnes, R. Ghara, A. Ghosh, S. K. Giri, I. T. Iliev, V. Jelić, R. Kooistra, R. Mondal, J. Schaye, and M. B. Silva. Improved upper limits on the 21 cm signal power spectrum of neutral hydrogen at z $\approx$ 9.1 from LOFAR. MNRAS, 493(2):1662–1685, April 2020. doi: 10.1093/mnras/staa327. 78, 102

Raul A. Monsalve, Alan E. E. Rogers, Judd D. Bowman, and Thomas J. Mozdzen. Results from EDGES High-band. I. Constraints on Phenomenological Models for the Global 21 cm Signal. ApJ, 847(1):64, September 2017. doi: 10.3847/1538-4357/aa88d1. 20

M. F. Morales and J. Hewitt. Toward Epoch of Reionization Measurements with Wide-Field Radio Observations. ApJ, 615:7–18, November 2004. doi: 10.1086/424437. 23, 24, 33, 35, 82, 84, 100

M. F. Morales and J. S. B. Wyithe. Reionization and Cosmology with 21-cm Fluctuations. ARA&A, 48:127–171, September 2010. doi: 10.1146/annurev-astro-081309-130936. 4, 17, 82, 100

A. H. Nuttall. Some Windows with Very Good Sidelobe Behavior. IEEE Transactions on Acoustics Speech and Signal Processing, 29:84–91, 1981. 83

A. R. Offringa. AOFlagger: RFI Software, October 2010. 40

A. R. Offringa, R. B. Wayth, N. Hurley-Walker, D. L. Kaplan, N. Barry, A. P. Beardsley, M. E. Bell, G. Bernardi, J. D. Bowman, F. Briggs, J. R. Callingham, R. J. Cappallo, P. Carroll, A. A. Deshpande, J. S. Dillon, K. S. Dwarakanath, A. Ewall-Wice, L. Feng, B.-Q. For, B. M. Gaensler, L. J. Greenhill, P. Hancock, B. J. Hazelton, J. N. Hewitt, L. Hindson, D. C. Jacobs, M. Johnston-Hollitt, A. D. Kapińska, H.-S. Kim, P. Kittiwisit, E. Lenc, J. Line, A. Loeb, C. J. Lonsdale, B. McKinley, S. R. McWhirter, D. A. Mitchell, M. F. Morales, E. Morgan, J. Morgan, A. R. Neben, D. Oberoi, S. M. Ord, S. Paul, B. Pindor, J. C. Pober, T. Prabu, P. Procopio, J. Riding, N. Udaya Shankar, S. Sethi, K. S. Srivani, L. Staveley-Smith, R. Subrahmanyan, I. S. Sullivan, M. Tegmark, N. Thyagarajan, S. J. Tingay, C. M. Trott, R. L. Webster, A. Williams, C. L. Williams, C. Wu, J. S. Wyithe,

and Q. Zheng. The Low-Frequency Environment of the Murchison Widefield Array: Radio-Frequency Interference Analysis and Mitigation. PASA, 32:e008, March 2015. doi: 10.1017/pasa.2015.7. 79

Yoshiaki Ono, Masami Ouchi, Bahram Mobasher, Mark Dickinson, Kyle Penner, Kazuhiro Shimasaku, Benjamin J. Weiner, Jeyhan S. Kartaltepe, Kimihiko Nakajima, Hooshang Nayyeri, Daniel Stern, Nobunari Kashikawa, and Hyron Spinrad. Spectroscopic Confirmation of Three z-dropout Galaxies at z = 6.844-7.213: Demographics of Lyα Emission in z ~7 Galaxies. ApJ, 744(2):83, January 2012. doi: 10.1088/0004-637X/744/2/83. 7

J. P. Ostriker and E. T. Vishniac. Generation of Microwave Background Fluctuations from Nonlinear Perturbations at the ERA of Galaxy Formation. ApJ, 306:L51, July 1986. doi: 10.1086/184704. 10

Gregory Paciga, Tzu-Ching Chang, Yashwant Gupta, Rajaram Nityanada, Julia Odegova, Ue-Li Pen, Jeffrey B. Peterson, Jayanta Roy, and Kris Sigurdson. The GMRT Epoch of Reionization experiment: a new upper limit on the neutral hydrogen power spectrum at z$\approx$ 8.6. MNRAS, 413(2):1174–1183, May 2011. doi: 10.1111/j.1365-2966.2011.18208.x. 23, 77

Gregory Paciga, Joshua G. Albert, Kevin Bandura, Tzu-Ching Chang, Yashwant Gupta, Christopher Hirata, Julia Odegova, Ue-Li Pen, Jeffrey B. Peterson, Jayanta Roy, J. Richard Shaw, Kris Sigurdson, and Tabitha Voytek. A simulation-calibrated limit on the H I power spectrum from the GMRT Epoch of Reionization experiment. MNRAS, 433(1):639–647, July 2013. doi: 10.1093/mnras/stt753. 102

A. Parsons, J. Pober, M. McQuinn, D. Jacobs, and J. Aguirre. A Sensitivity and Array-configuration Study for Measuring the Power Spectrum of 21 cm Emission from Reionization. ApJ, 753:81, July 2012a. doi: 10.1088/0004-637X/753/1/81. 37

A. R. Parsons and D. C. Backer. Calibration of Low-Frequency, Wide-Field Radio Interferometers Using Delay/Delay-Rate Filtering. AJ, 138:219–226, July 2009. doi: 10.1088/0004-6256/138/1/219. 77

A. R. Parsons, J. C. Pober, J. E. Aguirre, C. L. Carilli, D. C. Jacobs, and D. F. Moore. A Per-baseline, Delay-spectrum Technique for Accessing the 21 cm Cosmic Reionization Signature. ApJ, 756:165, September 2012b. doi: 10.1088/0004-637X/756/2/165. 24, 34, 35, 36, 48, 77, 78

A. R. Parsons, A. Liu, Z. S. Ali, and C. Cheng. Optimized Beam Sculpting with Generalized Fringe-rate Filters. ApJ, 820:51, March 2016. doi: 10.3847/0004-637X/820/1/51. 47, 62, 73, 74, 81, 84, 95

R. B. Partridge and P. J. E. Peebles. Are Young Galaxies Visible? II. The Integrated Background. ApJ, 148:377, May 1967. doi: 10.1086/149161. 7

A. H. Patil, S. Yatawatta, L. V. E. Koopmans, A. G. de Bruyn, M. A. Brentjens, S. Zaroubi, K. M. B. Asad, M. Hatef, V. Jelić, M. Mevius, A. R. Offringa, V. N. Pandey, H. Vedantham, F. B. Abdalla, W. N. Brouw, E. Chapman, B. Ciardi, B. K. Gehlot, A. Ghosh, G. Harker, I. T. Iliev, K. Kakiichi, S. Majumdar, G. Mellema, M. B. Silva, J. Schaye, D. Vrbanec, and S. J. Wijnholds. Upper Limits on the 21 cm Epoch of Reionization Power Spectrum from One Night with LOFAR. ApJ, 838(1): 65, March 2017. doi: 10.3847/1538-4357/aa63e7. 78

Nipanjana Patra, Ravi Subrahmanyan, A. Raghunathan, and N. Udaya Shankar. SARAS: a precision system for measurement of the cosmic radio background and signatures from the epoch of reionization. Experimental Astronomy, 36(1-2):319–370, August 2013. doi: 10.1007/s10686-013-9336-3. 20

Akash Kumar Patwa and Shiv Sethi. Detecting the 21 cm Signal from the Epoch of Reionization Using Drift Scans: Correlation of Time-ordered Visibilities. ApJ, 887 (1):52, December 2019. doi: 10.3847/1538-4357/ab5185. xii, 78, 81, 100

Akash Kumar Patwa, Shiv Sethi, and K. S. Dwarakanath. Extracting the 21 cm EoR signal using MWA drift scan data. MNRAS, 504(2):2062–2072, June 2021. doi: 10.1093/mnras/stab989. xii

S. Paul, S. K. Sethi, R. Subrahmanyan, N. Udaya Shankar, K. S. Dwarakanath, A. A. Deshpande, G. Bernardi, J. D. Bowman, F. Briggs, R. J. Cappallo, B. E. Corey, D. Emrich, B. M. Gaensler, R. F. Goeke, L. J. Greenhill, B. J. Hazelton, J. N. Hewitt, M. Johnston-Hollitt, D. L. Kaplan, J. C. Kasper, E. Kratzenberg, C. J. Lonsdale, M. J. Lynch, S. R. McWhirter, D. A. Mitchell, M. F. Morales, E. H. Morgan, D. Oberoi, S. M. Ord, T. Prabu, A. E. E. Rogers, A. A. Roshi, K. S. Srivani, S. J. Tingay, R. B. Wayth, M. Waterson, R. L. Webster, A. R. Whitney, A. J. Williams, and C. L. Williams. Study of Redshifted H I from the Epoch of Reionization with Drift Scan. ApJ, 793:28, September 2014a. doi: 10.1088/0004-637X/793/1/28. xi, xii, 34, 35, 36, 47, 51, 52, 58, 74, 78, 84, 95, 101

S. Paul, S. K. Sethi, R. Subrahmanyan, N. Udaya Shankar, K. S. Dwarakanath, A. A. Deshpande, G. Bernardi, J. D. Bowman, F. Briggs, R. J. Cappallo, B. E. Corey, D. Emrich, B. M. Gaensler, R. F. Goeke, L. J. Greenhill, B. J. Hazelton, J. N. Hewitt, M. Johnston-Hollitt, D. L. Kaplan, J. C. Kasper, E. Kratzenberg, C. J. Lonsdale, M. J. Lynch, S. R. McWhirter, D. A. Mitchell, M. F. Morales, E. H. Morgan, D. Oberoi, S. M. Ord, T. Prabu, A. E. E. Rogers, A. A. Roshi, K. S. Srivani, S. J. Tingay, R. B. Wayth, M. Waterson, R. L. Webster, A. R. Whitney, A. J. Williams,

and C. L. Williams. Study of Redshifted H I from the Epoch of Reionization with Drift Scan. ApJ, 793:28, September 2014b. doi: 10.1088/0004-637X/793/1/28. 100

S. Paul, S. K. Sethi, M. F. Morales, K. S. Dwarkanath, N. Udaya Shankar, R. Subrahmanyan, N. Barry, A. P. Beardsley, J. D. Bowman, F. Briggs, P. Carroll, A. de Oliveira-Costa, J. S. Dillon, A. Ewall-Wice, L. Feng, L. J. Greenhill, B. M. Gaensler, B. J. Hazelton, J. N. Hewitt, N. Hurley-Walker, D. J. Jacobs, H.-S. Kim, P. Kittiwisit, E. Lenc, J. Line, A. Loeb, B. McKinley, D. A. Mitchell, A. R. Neben, A. R. Offringa, B. Pindor, J. C. Pober, P. Procopio, J. Riding, I. S. Sullivan, M. Tegmark, N. Thyagarajan, S. J. Tingay, C. M. Trott, R. B. Wayth, R. L. Webster, J. S. B. Wyithe, R. Cappallo, M. Johnston-Hollitt, D. L. Kaplan, C. J. Lonsdale, S. R. McWhirter, E. Morgan, D. Oberoi, S. M. Ord, T. Prabu, K. S. Srivani, A. Williams, and C. L. Williams. Delay Spectrum with Phase-tracking Arrays: Extracting the HI Power Spectrum from the Epoch of Reionization. ApJ, 833:213, December 2016. doi: 10.3847/1538-4357/833/2/213. xxii, 52, 56, 58, 63, 65, 69, 70, 73, 77, 84

A. A. Penzias and R. W. Wilson. A Measurement of Excess Antenna Temperature at 4080 Mc/s. ApJ, 142:419–421, July 1965. doi: 10.1086/148307. 2

S. Perlmutter, G. Aldering, G. Goldhaber, R. A. Knop, P. Nugent, P. G. Castro, S. Deustua, S. Fabbro, A. Goobar, D. E. Groom, I. M. Hook, A. G. Kim, M. Y. Kim, J. C. Lee, N. J. Nunes, R. Pain, C. R. Pennypacker, R. Quimby, C. Lidman, R. S. Ellis, M. Irwin, R. G. McMahon, P. Ruiz-Lapuente, N. Walton, B. Schaefer, B. J. Boyle, A. V. Filippenko, T. Matheson, A. S. Fruchter, N. Panagia, H. J. M. Newberg, W. J. Couch, and The Supernova Cosmology Project. Measurements of Ω and Λ from 42 High-Redshift Supernovae. ApJ, 517(2):565–586, June 1999. doi: 10.1086/307221. 2

L. Philip, Z. Abdurashidova, H. C. Chiang, N. Ghazi, A. Gumba, H. M. Heilgendorff, J. M. Jáuregui-García, K. Malepe, C. D. Nunhokee, J. Peterson, J. L. Sievers, V. Simes, and R. Spann. Probing Radio Intensity at High-Z from Marion: 2017 Instrument. Journal of Astronomical Instrumentation, 8(2):1950004, January 2019. doi: 10.1142/S2251171719500041. 20

Planck Collaboration, P. A. R. Ade, N. Aghanim, M. Arnaud, M. Ashdown, J. Aumont, C. Baccigalupi, A. J. Banday, R. B. Barreiro, J. G. Bartlett, and et al. Planck 2015 results. XIII. Cosmological parameters. A&A, 594:A13, September 2016. doi: 10.1051/0004-6361/201525830. 48

Planck Collaboration, N. Aghanim, Y. Akrami, M. Ashdown, J. Aumont, C. Baccigalupi, M. Ballardini, A. J. Banday, R. B. Barreiro, N. Bartolo, S. Basak, R. Battye, K. Benabed, J. P. Bernard, M. Bersanelli, P. Bielewicz, J. J. Bock, J. R. Bond,

J. Borrill, F. R. Bouchet, F. Boulanger, M. Bucher, C. Burigana, R. C. Butler, E. Calabrese, J. F. Cardoso, J. Carron, A. Challinor, H. C. Chiang, J. Chluba, L. P. L. Colombo, C. Combet, D. Contreras, B. P. Crill, F. Cuttaia, P. de Bernardis, G. de Zotti, J. Delabrouille, J. M. Delouis, E. Di Valentino, J. M. Diego, O. Doré, M. Douspis, A. Ducout, X. Dupac, S. Dusini, G. Efstathiou, F. Elsner, T. A. Enßlin, H. K. Eriksen, Y. Fantaye, M. Farhang, J. Fergusson, R. Fernandez-Cobos, F. Finelli, F. Forastieri, M. Frailis, A. A. Fraisse, E. Franceschi, A. Frolov, S. Galeotta, S. Galli, K. Ganga, R. T. Génova-Santos, M. Gerbino, T. Ghosh, J. González-Nuevo, K. M. Górski, S. Gratton, A. Gruppuso, J. E. Gudmundsson, J. Hamann, W. Handley, F. K. Hansen, D. Herranz, S. R. Hildebrandt, E. Hivon, Z. Huang, A. H. Jaffe, W. C. Jones, A. Karakci, E. Keihänen, R. Keskitalo, K. Kiiveri, J. Kim, T. S. Kisner, L. Knox, N. Krachmalnicoff, M. Kunz, H. Kurki-Suonio, G. Lagache, J. M. Lamarre, A. Lasenby, M. Lattanzi, C. R. Lawrence, M. Le Jeune, P. Lemos, J. Lesgourgues, F. Levrier, A. Lewis, M. Liguori, P. B. Lilje, M. Lilley, V. Lindholm, M. López-Caniego, P. M. Lubin, Y. Z. Ma, J. F. Macías-Pérez, G. Maggio, D. Maino, N. Mandolesi, A. Mangilli, A. Marcos-Caballero, M. Maris, P. G. Martin, M. Martinelli, E. Martínez-González, S. Matarrese, N. Mauri, J. D. McEwen, P. R. Meinhold, A. Melchiorri, A. Mennella, M. Migliaccio, M. Millea, S. Mitra, M. A. Miville-Deschênes, D. Molinari, L. Montier, G. Morgante, A. Moss, P. Natoli, H. U. Nørgaard-Nielsen, L. Pagano, D. Paoletti, B. Partridge, G. Patanchon, H. V. Peiris, F. Perrotta, V. Pettorino, F. Piacentini, L. Polastri, G. Polenta, J. L. Puget, J. P. Rachen, M. Reinecke, M. Remazeilles, A. Renzi, G. Rocha, C. Rosset, G. Roudier, J. A. Rubiño-Martín, B. Ruiz-Granados, L. Salvati, M. Sandri, M. Savelainen, D. Scott, E. P. S. Shellard, C. Sirignano, G. Sirri, L. D. Spencer, R. Sunyaev, A. S. Suur-Uski, J. A. Tauber, D. Tavagnacco, M. Tenti, L. Toffolatti, M. Tomasi, T. Trombetti, L. Valenziano, J. Valiviita, B. Van Tent, L. Vibert, P. Vielva, F. Villa, N. Vittorio, B. D. Wandelt, I. K. Wehus, M. White, S. D. M. White, A. Zacchei, and A. Zonca. Planck 2018 results. VI. Cosmological parameters. A&A, 641:A6, September 2020. doi: 10.1051/0004-6361/201833910. 2, 8, 9, 18, 78, 99

William H. Press, Saul A. Teukolsky, William T. Vetterling, and Brian P. Flannery. Numerical recipes in FORTRAN. The art of scientific computing. 1992. 35

D. C. Price, L. J. Greenhill, A. Fialkov, G. Bernardi, H. Garsden, B. R. Barsdell, J. Kocz, M. M. Anderson, S. A. Bourke, J. Craig, M. R. Dexter, J. Dowell, M. W. Eastwood, T. Eftekhari, S. W. Ellingson, G. Hallinan, J. M. Hartman, R. Kimberk, T. Joseph W. Lazio, S. Leiker, D. MacMahon, R. Monroe, F. Schinzel, G. B. Taylor, E. Tong, D. Werthimer, and D. P. Woody. Design and characterization of the Large-aperture Experiment to Detect the Dark Age (LEDA) radiometer systems. MNRAS, 478(3):4193–4213, August 2018. doi: 10.1093/mnras/sty1244. 20

J. R. Pritchard and A. Loeb. 21 cm cosmology in the 21st century. Reports on Progress in Physics, 75(8):086901, August 2012. doi: 10.1088/0034-4885/75/8/086901. xix, 5, 15, 18, 19

Jonathan R. Pritchard and Abraham Loeb. Constraining the unexplored period between the dark ages and reionization with observations of the global 21 cm signal. Phys. Rev. D, 82(2):023006, July 2010. doi: 10.1103/PhysRevD.82.023006. 17

Janakee Raste and Shiv Sethi. An Analytic Formulation of the 21 cm Signal from the Early Phase of the Epoch of Reionization. ApJ, 860(1):55, June 2018. doi: 10.3847/1538-4357/aac2d8. 22

M. J. Rees. Polarization and Spectrum of the Primeval Radiation in an Anisotropic Universe. ApJ, 153:L1, July 1968. doi: 10.1086/180208. 8

Christian L. Reichardt. Observing the Epoch of Reionization with the Cosmic Microwave Background, volume 423 of Astrophysics and Space Science Library, page 227. 2016. doi: 10.1007/978-3-319-21957-8_8. xix, 9

Adam G. Riess, Alexei V. Filippenko, Peter Challis, Alejandro Clocchiatti, Alan Diercks, Peter M. Garnavich, Ron L. Gilliland, Craig J. Hogan, Saurabh Jha, Robert P. Kirshner, B. Leibundgut, M. M. Phillips, David Reiss, Brian P. Schmidt, Robert A. Schommer, R. Chris Smith, J. Spyromilio, Christopher Stubbs, Nicholas B. Suntzeff, and John Tonry. Observational Evidence from Supernovae for an Accelerating Universe and a Cosmological Constant. AJ, 116(3):1009–1038, September 1998. doi: 10.1086/300499. 2

Brant E. Robertson, Richard S. Ellis, James S. Dunlop, Ross J. McLure, and Daniel P. Stark. Early star-forming galaxies and the reionization of the Universe. Nature, 468 (7320):49–55, November 2010. doi: 10.1038/nature09527. xix, 3

A. E. E. Rogers and J. D. Bowman. Spectral Index of the Diffuse Radio Background Measured from 100 to 200 MHz. AJ, 136:641–648, August 2008. doi: 10.1088/0004-6256/136/2/641. xxii, 38, 68, 80

G. B. Rybicki and A. P. Lightman. Radiative processes in astrophysics. 1979. 16

Mário G. Santos, Alexandre Amblard, Jonathan Pritchard, Hy Trac, Renyue Cen, and Asantha Cooray. Cosmic Reionization and the 21 cm Signal: Comparison between an Analytical Model and a Simulation. ApJ, 689(1):1–16, December 2008. doi: 10.1086/592487. xx, 22, 23

S. K. Sethi. HI signal from re-ionization epoch. MNRAS, 363:818–830, November 2005. doi: 10.1111/j.1365-2966.2005.09485.x. 4, 23

Harlow Shapley and Heber D. Curtis. The Scale of the Universe. Bulletin of the National Research Council, 2(11):171–217, May 1921. 1

P. Sharma. Astrophysical radio background cannot explain the EDGES 21-cm signal: constraints from cooling of non-thermal electrons. MNRAS, 481:L6–L10, November 2018. doi: 10.1093/mnrasl/sly147. 21

J. R. Shaw, K. Sigurdson, U.-L. Pen, A. Stebbins, and M. Sitwell. All-sky Interferometry with Spherical Harmonic Transit Telescopes. ApJ, 781:57, February 2014. doi: 10.1088/0004-637X/781/2/57. 47, 73, 74, 92

J. R. Shaw, K. Sigurdson, M. Sitwell, A. Stebbins, and U.-L. Pen. Coaxing cosmic 21 cm fluctuations from the polarized sky using m -mode analysis. Phys. Rev. D, 91 (8):083514, April 2015. doi: 10.1103/PhysRevD.91.083514. 47, 73

S. Singh, R. Subrahmanyan, N. Udaya Shankar, M. Sathyanarayana Rao, A. Fialkov, A. Cohen, R. Barkana, B. S. Girish, A. Raghunathan, R. Somashekar, and K. S. Srivani. First Results on the Epoch of Reionization from First Light with SARAS 2. ApJ, 845:L12, August 2017. doi: 10.3847/2041-8213/aa831b. 20

S. Singh, R. Subrahmanyan, N. U. Shankar, M. S. Rao, B. S. Girish, A. Raghunathan, R. Somashekar, and K. S. Srivani. SARAS 2: a spectral radiometer for probing cosmic dawn and the epoch of reionization through detection of the global 21-cm signal. Experimental Astronomy, 45:269–314, April 2018a. doi: 10.1007/s10686-018-9584-3. 20

S. Singh, R. Subrahmanyan, N. Udaya Shankar, M. Sathyanarayana Rao, A. Fialkov, A. Cohen, R. Barkana, B. S. Girish, A. Raghunathan, R. Somashekar, and K. S. Srivani. SARAS 2 Constraints on Global 21 cm Signals from the Epoch of Reionization. ApJ, 858:54, May 2018b. doi: 10.3847/1538-4357/aabae1. 20

Saurabh Singh and Ravi Subrahmanyan. The Redshifted 21 cm Signal in the EDGES Low-band Spectrum. ApJ, 880(1):26, July 2019. doi: 10.3847/1538-4357/ab2879. 21

Marcin Sokolowski, Randall B. Wayth, Steven E. Tremblay, Steven J. Tingay, Mark Waterson, Jonathan Tickner, David Emrich, Franz Schlagenhaufer, David Kenney, and Shantanu Padhi. The Impact of the Ionosphere on Ground-based Detection of the Global Epoch of Reionization Signal. ApJ, 813(1):18, November 2015. doi: 10.1088/0004-637X/813/1/18. 39

Suzanne Staggs, Jo Dunkley, and Lyman Page. Recent discoveries from the cosmic microwave background: a review of recent progress. Reports on Progress in Physics, 81(4):044901, April 2018. doi: 10.1088/1361-6633/aa94d5. 2

I. A. Strukov, A. A. Brukhanov, D. P. Skulachev, and M. V. Sazhin. Anisotropy of the microwave background radiation. Soviet Astronomy Letters, 18(5):153, May 1992. 2

R. A. Sunyaev and Ia. B. Zeldovich. The velocity of clusters of galaxies relative to the microwave background - The possibility of its measurement. MNRAS, 190: 413–420, February 1980. doi: 10.1093/mnras/190.3.413. 10

R. A. Sunyaev and Y. B. Zeldovich. The Observations of Relic Radiation as a Test of the Nature of X-Ray Radiation from the Clusters of Galaxies. Comments on Astrophysics and Space Physics, 4:173, November 1972. 10

G. B. Taylor, C. L. Carilli, and R. A. Perley, editors. Synthesis Imaging in Radio Astronomy II, volume 180 of Astronomical Society of the Pacific Conference Series, 1999. xx, 28, 29, 36, 49

N. Thyagarajan, N. Udaya Shankar, R. Subrahmanyan, W. Arcus, G. Bernardi, J. D. Bowman, F. Briggs, J. D. Bunton, R. J. Cappallo, B. E. Corey, L. deSouza, D. Emrich, and others. A Study of Fundamental Limitations to Statistical Detection of Redshifted H I from the Epoch of Reionization. ApJ, 776:6, October 2013. doi: 10.1088/0004-637X/776/1/6. xx, 36, 40

S. J. Tingay, R. Goeke, J. D. Bowman, D. Emrich, and others. The Murchison Widefield Array: The Square Kilometre Array Precursor at Low Radio Frequencies. PASA, 30:e007, January 2013. doi: 10.1017/pasa.2012.007. 23, 37, 42, 52, 79, 83

P. Tozzi, P. Madau, A. Meiksin, and M. J. Rees. The first light seen in the redshifted 21-cm radiation. Nuclear Physics B Proceedings Supplements, 80:05, January 2000. 100

C. M. Trott. Comparison of Observing Modes for Statistical Estimation of the 21 cm Signal from the Epoch of Reionisation. PASA, 31:e026, July 2014. doi: 10.1017/pasa.2014.23. xii, 47, 78

C. M. Trott, B. Pindor, P. Procopio, R. B. Wayth, D. A. Mitchell, B. McKinley, S. J. Tingay, N. Barry, A. P. Beardsley, G. Bernardi, J. D. Bowman, F. Briggs, R. J. Cappallo, P. Carroll, A. de Oliveira-Costa, J. S. Dillon, A. Ewall-Wice, L. Feng, L. J. Greenhill, B. J. Hazelton, J. N. Hewitt, N. Hurley-Walker, M. Johnston-Hollitt, D. C. Jacobs, D. L. Kaplan, H. S. Kim, E. Lenc, J. Line, A. Loeb, C. J. Lonsdale, M. F. Morales, E. Morgan, A. R. Neben, N. Thyagarajan, D. Oberoi, A. R. Offringa, S. M. Ord, S. Paul, J. C. Pober, T. Prabu, J. Riding, N. Udaya Shankar, S. K. Sethi, K. S. Srivani, R. Subrahmanyan, I. S. Sullivan, M. Tegmark, R. L. Webster, A. Williams,

C. L. Williams, C. Wu, and J. S. B. Wyithe. CHIPS: The Cosmological H i Power Spectrum Estimator. ApJ, 818:139, February 2016. doi: 10.3847/0004-637X/818/2/139. 78

Cathryn M. Trott, C. H. Jordan, S. Midgley, N. Barry, B. Greig, B. Pindor, J. H. Cook, G. Sleap, S. J. Tingay, D. Ung, P. Hancock, A. Williams, J. Bowman, R. Byrne, A. Chokshi, B. J. Hazelton, K. Hasegawa, D. Jacobs, R. C. Joseph, W. Li, J. L. B. Line, C. Lynch, B. McKinley, D. A. Mitchell, M. F. Morales, M. Ouchi, J. C. Pober, M. Rahimi, K. Takahashi, R. B. Wayth, R. L. Webster, M. Wilensky, J. S. B. Wyithe, S. Yoshiura, Z. Zhang, and Q. Zheng. Deep multiredshift limits on Epoch of Reionization 21 cm power spectra from four seasons of Murchison Widefield Array observations. MNRAS, 493(4):4711–4727, April 2020. doi: 10.1093/mnras/staa414. 78, 102

H. C. Van de Hulst. Herkomst der radiogolven uit het wereldruim. Nederlandsch Tijdschrift voor Natuurkunde, 11:210, 1945. 12

H. C. Van De Hulst. Origin of the Radio Waves from Space, pages 302–316. Springer Netherlands, Dordrecht, 1982. ISBN 978-94-009-7752-5. doi: 10.1007/978-94-009-7752-5_34. URL https://doi.org/10.1007/978-94-009-7752-5_34. 12

M. P. van Haarlem, M. W. Wise, A. W. Gunst, G. Heald, J. P. McKean, J. W. T. Hessels, A. G. de Bruyn, R. Nijboer, J. Swinbank, R. Fallows, M. Brentjens, A. Nelles, R. Beck, H. Falcke, R. Fender, J. Hörandel, L. V. E. Koopmans, G. Mann, G. Miley, H. Röttgering, B. W. Stappers, and others. LOFAR: The LOw-Frequency ARray. A&A, 556:A2, August 2013. doi: 10.1051/0004-6361/201220873. 23

H. Vedantham, N. Udaya Shankar, and R. Subrahmanyan. Imaging the Epoch of Reionization: Limitations from Foreground Confusion and Imaging Algorithms. ApJ, 745:176, February 2012. 36

Randall B. Wayth, Steven J. Tingay, Cathryn M. Trott, David Emrich, Melanie Johnston-Hollitt, Ben McKinley, B. M. Gaensler, A. P. Beardsley, T. Booler, B. Crosse, T. M. O. Franzen, L. Horsley, D. L. Kaplan, D. Kenney, M. F. Morales, D. Pallot, G. Sleap, K. Steele, M. Walker, A. Williams, C. Wu, Iver. H. Cairns, M. D. Filipovic, S. Johnston, T. Murphy, P. Quinn, L. Staveley-Smith, R. Webster, and J. S. B. Wyithe. The Phase II Murchison Widefield Array: Design overview. PASA, 35:33, Nov 2018. doi: 10.1017/pasa.2018.37. 42, 79

Michael J. Wilensky, Miguel F. Morales, Bryna J. Hazelton, Nichole Barry, Ruby Byrne, and Sumit Roy. Absolving the SSINS of Precision Interferometric Radio

Data: A New Technique for Mitigating Faint Radio Frequency Interference. PASP, 131(1005):114507, November 2019. doi: 10.1088/1538-3873/ab3cad. 40

Peter N. Wilkinson. An introduction to closure phase and self-calibration. In Marcello Felli and Ralph E. Spencer, editors, NATO Advanced Science Institutes (ASI) Series C, volume 283 of NATO Advanced Science Institutes (ASI) Series C, pages 69–93, January 1989. doi: 10.1007/978-94-009-2428-4_1. 41

S. A. Wouthuysen. On the excitation mechanism of the 21-cm (radio-frequency) interstellar hydrogen emission line. AJ, 57:31–32, 1952. doi: 10.1086/106661. 14

J. M. Wrobel and R. C. Walker. Sensitivity. In G. B. Taylor, C. L. Carilli, and R. A. Perley, editors, Synthesis Imaging in Radio Astronomy II, volume 180 of Astronomical Society of the Pacific Conference Series, page 171, January 1999. 36, 37

J. S. B. Wyithe and M. F. Morales. Biased reionization and non-Gaussianity in redshifted 21-cm intensity maps of the reionization epoch. MNRAS, 379:1647–1657, August 2007. doi: 10.1111/j.1365-2966.2007.12048.x. 33

Saleem Zaroubi. The Epoch of Reionization, volume 396 of Astrophysics and Space Science Library, page 45. 2013. doi: 10.1007/978-3-642-32362-1_2. 5, 17